THESIS FOR THE DEGREE OF DOCTOR OF PHILOSOPHY

High Precision Micro-Grinding of Advanced Materials

MOHAMMADALI KADIVAR

Department of Industrial and Materials Science

CHALMERS UNIVERSITY OF TECHNOLOGY

Gothenburg, Sweden 2021

High Precision Micro-Grinding of Advanced Materials

MOHAMMADALI KADIVAR
ISBN 978-91-7905-457-1

Doktorsavhandlingar vid Chalmers tekniska högskola
Ny serie nr 4924
ISSN 0346-718X

Department of Industrial and Materials Science
Chalmers University of Technology
SE-412 96 Gothenburg
Sweden
Telephone + 46 (0)31-772 1000

Printed by Chalmers Reproservice

Gothenburg, Sweden 2021

To my beloved mother

Toran Daneshvar

High precision micro-grinding of advanced materials

MOHAMMADALI KADIVAR
Department of Industrial and Materials Science
Chalmers University of Technology

Abstract

The aim of this thesis is to advance a fundamental understanding of process mechanics and surface integrity in micro-grinding of advanced materials, such as additively and conventionally manufactured titanium and engineering ceramic. Grinding forces and specific grinding energy were chosen as the two most important indicators to investigate the process. The surface integrity was evaluated using X-ray diffraction measurements to quantify residual stresses, surface roughness measurements, SEM microscopy, and confocal images. At the first stage, the influence of different micro-grinding and dressing parameters and different tool specifications was examined. Then, via process modelling, the outcome of the micro-grinding process at different chip thicknesses and aggressiveness numbers was studied. Additionally, a hybrid laser-assisted micro-grinding process was developed to improve the process efficiency.

The results show that the flow stress of the material did not change with the changing of cutting speed and cutting strain rate. Moreover, it was observed that the depth of cut and grinding feed rate had the same (neutral) effect on the resultant grinding forces. Therefore, the efficiency of titanium micro-grinding could be highly influenced by changing the topography of the micro-grinding tool through different dressing parameters. However, using higher chip thicknesses resulted in a more efficient process in terms of cutting/chip-formation. The lowest specific energy, obtained in the single grain tests, was 11.5 J/mm^3 for both-types of titanium materials. In contrast, a much higher minimum specific energy in real micro-grinding process with several (bonded) grains was observed – showing a higher amount of ploughing and rubbing/friction in the micro-grinding process. The build-up direction of additively-manufactured titanium, at low chip thickness, affected the process efficiency. In larger chip thicknesses, almost the same specific energy was measured independent of the material manufacturing method. The results of the XRD analysis showed that contrary to the specific grinding energy, the residual stresses of the ground surface changed by varying the cutting speed and feed-rate-to-depth-of-cut ratio, v_w/a_e. Higher cutting speeds resulted in lower compressive residual stress, and higher feed-rate-to-depth-of-cut ratios resulted in higher compressive stresses. This can be attributed to higher temperatures in the chip-formation process compared to the plastic deformation in micro-grinding at higher cutting speeds and lower v_w/a_e ratios, which was proved via SEM micrographs. A more efficient micro-grinding process was achieved via the Laser-Assisted Micro-Grinding (LAMG) process of a Si_3N_4 workpiece, where the values of the specific grinding energy, as well as the tool deflection by the LAMG process, were much lower than the Conventional Micro-Grinding (CMG) process.

Keywords: Micro-grinding; Additive manufacturing; Surface integrity; Process efficiency; Titanium; Ceramic; Modeling; Laser-assisted micro-grinding

Preface

This thesis is based on work performed at the Institute of Precision Machining (KSF) at Hochschule Furtwangen University (Germany) and the Department of Industrial and Materials Science, Chalmers University of Technology. The work has been carried out under the main supervision of Professor Peter Krajnik and co-supervision by Professor Bahman Azarhoushang and Professor Uta Klement.

This thesis consists of an introductory part followed by the appended papers:

Paper I: **The effect of dressing parameters on micro-grinding of titanium alloy.**
Kadivar, Mohammadali, Bahman Azarhoushang, Sergey Shamray, and Peter Krajnik.
Precision Engineering 51 (2018): 176-185.

Paper II: **Modeling of the micro-grinding process considering the grinding tool topography.**
Kadivar, Mohammadali, Ali Zahedi, Bahman Azarhoushang, and Peter Krajnik.
International Journal of Abrasive Technology 8, no. 2 (2017): 157-170.

Paper III: **Laser-assisted micro-grinding of Si_3N_4.**
Mohammadali Kadivar, Sergey Shamray, Babak Soltani, Amir Daneshi, Bahman Azarhoushang.
Precision Engineering 60 (2019) 394–404.

Paper IV: **Surface integrity in micro-grinding of Ti6Al4V considering the specific micro-grinding energy.**
Mohammadali Kadivar, Bahman Azarhoushang, Amir Daneshi, Peter Krajnik.
Procedia CIRP 87 (2020): 181-185.

Paper V: **Performance of micro-grinding pins with different bonding while micro-grinding Si_3N_4.**
Sergei Shamray, Mohammadali Kadivar, Amir Daneshi, and Bahman Azarhoushang.
International Journal of Abrasive Technology 10.1 (2020): 16-31.

Paper VI: **Modeling of micro-grinding forces considering dressing parameters and tool deflection.**
Mohammadali Kadivar, Bahman Azarhoushang, Peter Krajnik.
Precision Engineering 67(2021): 269-281.

Paper VII: **The role of specific energy in micro-grinding of titanium alloy.**
Mohammadali Kadivar, Bahman Azarhoushang, Uta Klement, and Peter Krajnik.
Accepted for publication in Precision Engineering.

Paper not appended to the thesis:

Paper A: **Intelligent grinding process via artificial neural networks.**
Mohammadali Kadivar and Bahman Azarhoushang.
The Upper-Rhine Artificial Intelligence Symposium UR-AI 2019, March 13th, 2019, Offenburg, Germany. ISBN: 978-3-9820756-0-0. 6 pages.

Paper B: **The effect of dressing parameters on the chip loading and ground surface quality by using grinding pins and grinding wheels with very fine grits.**
Kadivar, Mohammadali, Heike Kitzig-Frank, and Bahman Azarhoushang.
Fourth European Seminar on Precision Optics Manufacturing, vol. 10326, p. 103260E. International Society for Optics and Photonics, 2017.

Paper C: **Study of specific energy in grinding of tungsten carbide.**
Kadivar M, Daneshi A, Azarhoushang B.
14th international conference on high-speed machining, 17 -18 April, San Sebastian, Spain.

Paper D: **Laser-assisted micro-milling of austenitic stainless steel X5CrNi18-10.**
Kadivar M, Azarhoushang B, Zahedi A, Müller C.
Journal of Manufacturing Processes. 2019 Dec 1;48:174-84.

Paper E: **Spezifische Energie beim Schleifen von Wolframcarbid-Kobalt.**
Kadivar M, Daneshi A, Bösinger R, Azarhoushang B.
Schleifen + Polieren, 23.2019,6-9.

Paper F: **Moderne Zerspanungstechnologien-High Speed Cutting.**
Azarhoushang B, Kitzig-Frank H, Kadivar M.
Jahrbuch zum 3. Innovation Forum Zerspanungstechnologie, 2019.

Paper G: **Moderne Zerspanungstechnologien-Hybridbearbeitungsprozesse.**
Azarhoushang B, Kitzig-Frank H, Kadivar M, Ghadiri E.
Jahrbuch zum 3. Innovation Forum Zerspanungstechnologie, 2019.

Paper H: **Laser optimiert Zerspanung.**
Azarhoushang B, Zahedi A, Soltani B, Kadivar M, Kitzig-Frank H.
WB Werkstatt + Betrieb, 152.2019-16-19.

Paper K: **High-speed high-efficient grinding of CMCs with structured grinding wheels.**
Azarhoushang B, Kadivar M, Bösinger R, Shamray S, Zahedi A, Daneshi A.
International Journal of Abrasive Technology. 2019;9(1):1-5.

Paper L: **First Steps through Intelligent Grinding Using Machine Learning via Integrated Acoustic Emission Sensors.**
Mirifar S, Kadivar M, Azarhoushang B.
Journal of Manufacturing and Materials Processing. 2020 Jun;4(2):35.

Paper M: **A Numerical Model for Heat Transfer in Dry and Wet Grinding Based on the Finite Difference Method and Jet Cooling.**
Kadivar M, Kadivar M, Daneshi A.
Journal of Thermal Science and Engineering Applications. 2020 Aug 1;12(4).

Contribution to the appended papers

My contribution to the appended papers is as follows:

Paper I: I participated in the conceptualization and methodology of the paper with the help of co-authors. I performed all data curation, the experimental work, and investigation, as well as writing the original draft of the paper. The paper was then reviewed & edited by co-authors. The resources were provided by KSF institute.

Paper II: I planned the conceptualization with the co-authors. I performed the data curation, investigation, methodology, software programing, the experimental work, and simulation study with the help of Dr. Ali Zahedi, as well as validated the results. I also wrote the first original draft of the paper with the help of Dr. Zahedi. The text was later reviewed & edited by co-authors. The resources were provided by KSF institute.

Paper III: The conceptualization of the work was done with the help of co-authors and me. The data curation, investigation, the experimental work, and methodology were performed by me and Mr. Shamray. Mr. Soltani and I did the software programming and simulation. The simulation was validated by me. The original draft of the paper was written by me and was reviewed & edited by co-authors. KSF institute provided the resources.

Paper IV: Dr. Daneshi and I planned the conceptualization of the work. The data curation, investigation, validation, the experimental work, and methodology were completed by me. The original draft of the paper was written by me and reviewed & edited by co-authors. KSF institute and Hochschule Furtwangen provided the resources.

Paper V: Mr. Shamray did the data curation and investigation. The conceptualization, validation, the experimental work, and methodology of the work were done by me and Mr. Shamray. I wrote the original draft of the paper. The paper was later reviewed & edited by co-authors. KSF institute provided the resources.

Paper VI: The software programming, formal analysis, data curation, investigation, the experimental work, and validation were done by me. I participated in the conceptualization part with the help of co-authors and we built the methodology of the work. I wrote the original draft of the paper and the co-authors reviewed & edited the paper. KSF institute provided the resources.

Paper VII: I designed the test matrix and did the characterization work as a part of data curation, methodology, the experimental work, and investigation. I participated in the conceptualization with the help of co-authors. I wrote the original draft of the paper and the co-authors reviewed & edited the paper. KSF institute and Hochschule Furtwangen provided the resources.

Table of Contents

1. Introduction

The demands on miniaturized/micro-products/systems and components in many areas such as the automotive, biomedical, robotic, and micro-systems industries are increasing, however manufacturing micro-products remains challenging [1]. These micro-parts are generally complex and have strict requirements, such as high dimensional accuracy and surface integrity. Currently, the mass production of miniaturized components in micro and meso-scale is mainly dominated by semiconductor technology via lithographic and etching processes [2]. The use of such processes does not meet the required flexibility with respect to a small or medium series production of free-form 3D structures [3]. Additionally, the workpiece material is a limitation factor for micro-manufacturing. For example, only conductive materials can be machined using Electro Discharge Machining (EDM). Finding a manufacturing process that could provide a high level of accuracy and guarantee the part quality with complex features is challenging. A robust manufacturing process to fulfill such stringent requirements is mechanical micro-machining. Mechanical micro-machining enables the production of highly accurate and complex 3D micro-parts, made from a variety of engineering materials including titanium and its alloy, tungsten carbides, nickel alloys, aluminum, glass, as well as ceramics. Additionally, an acceptable degree of flexibility can be obtained. Therefore, mechanical micro-machining is becoming increasingly important for future manufacturing technologies, offering a potential capacity to economically machine miniaturized parts in small batch sizes.

In the fabrication of micro-scale parts (Fig. 1 right) and features, micro-grinding offers several advantages such as higher flexibility, higher quality, and workpiece material independence over other mechanical micro-machining processes, such as micro-milling (for example, better surface quality and higher dimensional accuracy in micro-grinding compared to micro-milling). Contrary to the conventional (macro) grinding process, which is typically employed for grinding of simple components, micro-grinding offers a high degree of geometric flexibility to produce micro-parts with sophisticated features. Some examples are micro-sensors, micro-actuators, micro-fluidic devices, and micro-machine parts. Although there are some kinematic similarities between the micro and conventional grinding process, the micro-grinding process is distinctive because of the size effect, dimensions, and accuracy of micro-parts or features, tool geometry, tool deflection, as well as the application area associated with very small chip thicknesses. [4–6]. The ratio of the size of part or the micro-feature to the cutting tool dimension is smaller in the micro-grinding process and cutting conditions are much finer than the macro-grinding. Therefore, the outputs of the micro-grinding process, like the surface quality and micro-grinding forces, are related to the mechanical and thermal interactions between a single grit and the work material. Simply stated, the size effects can change the whole aspect of the machining process.

Micro-grinding, which uses abrasive tools with geometrically undefined cutting-edges, is a promising procedure (in some cases the only possibility) to machine hard and brittle materials [7]. However, the machining of miniaturized hard-to-cut materials using abrasive tools is difficult due to their complex and non-deterministic nature [8–10]. Accordingly, despite the advantages of hard-to-cut materials, the use of these materials is limited by the high processing and finishing costs. For instance, the machining of ceramic materials is subjected to high grinding forces and very high tool wear – limiting the achievable tolerances. The micro-tool is also subjected to high deflections and rapid tool wear because of high grinding forces acting upon small tool diameters (0.2 to 2 mm), which directly affects part accuracy [4].

The number of research publications in the field of micro-grinding has increased during previous decades (as shown in Fig. 1 left) – showing academic interest in the subject area. It is projecting also the potential of more specific analysis in the near future for different kind of

materials – where new process conditions according to different chipping mechanism for different materials are needed to be established. Currently, the research on the micro-grinding process is still in its early stages and mostly related to the effect of main process parameters. Micro-grinding is an effective process in which high dimensional accuracy (Fig. 1 right) and superior surface finish are achievable. Moreover, unlike other micro-machining processes, micro-grinding is applicable to a wide range of materials (from soft to brittle and hard-to-cut materials). Therefore, the micro-grinding process has potential to be broadly adopted by industries for a wide range of applications. However, further fundamental studies in this field seem essential in order to understand the process.

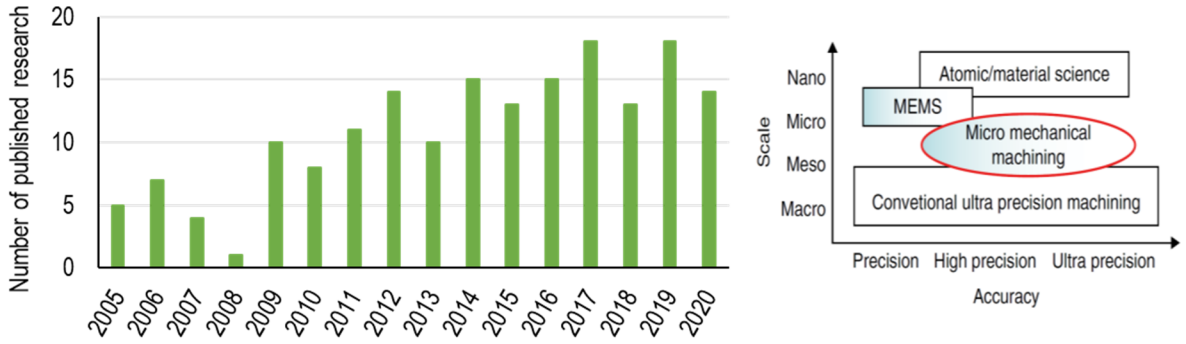

Fig. 1. Left: Yearly research publication trend in micro-grinding (Google scholar); right: dimensional size for the micro-mechanical machining (Reprinted with permission from [11]).

1.1. Objective and research questions

The main objective of this thesis is to advance an understanding of the fundamental mechanisms in micro-grinding of advanced materials to achieve an efficient process with desirable accuracy and minimum surface and subsurface damages.

Using the Research Questions (RQ) below the specific objectives of the thesis translate to:

- RQ1: What is the main material removal mechanism in the micro-grinding process related to the workpiece material and how can the surface accuracy and quality be affected?
- RQ2: What are the dominant grinding and dressing parameters affecting the efficiency of the micro-grinding process?
- RQ3: What methods should be used for modelling the micro-grinding forces and resulting surface roughness? And what are the most influential parameters?
- RQ4: What are the differences in grindability of Additive Manufactured (AM) and conventionally-fabricated parts, considering the process efficiency?

1.2. Research approach

One of the criteria for evaluating the efficiency of the process, and at the same time a key indicator of grindability is the specific grinding energy. The specific grinding energy, defined as the energy expended to remove a unit volume of material, is a critical parameter that indicates the efficiency of the grinding process [12]. In micro-grinding, high specific energy is generally required for the material removal because of high elastic and plastic deformations in the chip formation process as well as the friction between the grains and the ground material [6]. Therefore, using this fundamental parameter/indicator, the dependency of the process

efficiency on the material properties, manufacturing method, process parameters, and tool specifications can be characterized.

To cover the RQs, two kinds of materials are addressed; titanium alloy (Ti6Al4V) as a ductile material (additively and conventionally manufactured) and Si_3N_4 as a brittle material. Such distinct material selection enables us to address the (characteristic) influence of the workpiece material on process efficiency. To improve the efficiency of the micro-grinding process, detailed knowledge regarding (controllable/input) process parameters, such as the topography of the grinding tool and the bond material, is needed. Moreover, to achieve a highly-efficient grinding process, it is particularly important to know the effects of these inputs on the process outputs, such as grinding forces and surface quality. Thus, the effect of bonding materials, microtopography of the grinding tool, and the process parameters are also investigated by choosing four types of bond materials (vitrified (V), metal (M), hybrid (H), and electroplated (E)).

A novel (hybrid) method was also proposed to achieve an optimal micro-grinding process with high material removal rates and desired part accuracy, combining micro-grinding and ultra-short pulsed laser ablation. The laser beam was used to remove material and create micro-structures on the surface of either the workpiece or grinding tool prior to the micro-grinding. The structured areas reduce the workpiece-tool contact area. The resulting reduction of specific grinding energy by laser assistance leads to a more efficient and accurate micro-grinding process. Furthermore, an attempt is made to develop a model to predict grinding forces, considering the effects of dressing parameters and tool deflection. In this approach, the chip thickness was modeled by a probabilistic function, based on the kinematics of the process, a topography of the tool, and properties of titanium.

The flowchart in Fig. 2 provides an overview of the research approach and how the formulated RQs in section 1.1 are systematically addressed.

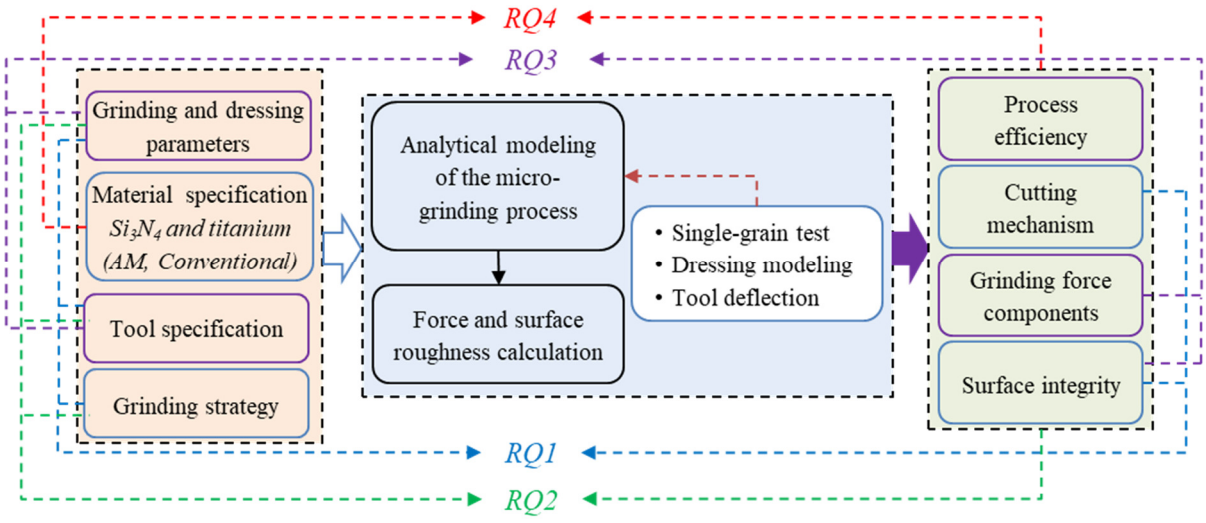

Fig. 2. Flowchart of the research approach and procedure corresponds to the research questions (RQs).

The publications used in this dissertation can be divided into 3 categories to address the research questions:

- Inputs: on understanding the process inputs (Paper I, and V) – to investigate the effects of influential parameters on micro-grinding outcomes, i.e. surface roughness and micro-grinding forces, addressing the RQ1.
- Process: on understanding fundamental process mechanics via modeling (Paper II and VI) – to explain the material removal mechanism in micro-grinding process and quantify the factors/parameters affecting the material-removal mechanism (RQ1 and RQ3).
- Outputs: on characterizing process efficiency via the specific grinding energy and surface integrity (Paper III, IV, and VII) – to investigate produced/generated surfaces (without or with minimum surface damage) – addressing RQ2 and RQ4.

Generally, the underlying approach in this work was to investigate the grindability of the advanced materials, i.e. additively and conventionally-manufactured Ti6Al4V and Si_3N_4 with the help of material-characterization techniques and assessment of specific grinding energy in order to achieve a highly accurate surface finish with minimum surface and subsurface damages (focus on process efficiency). In that way, it was possible to connect the surface integrity of the part, specific micro-grinding energy, and controllable process parameters.

The aim of Paper I and V was to obtain a fundamental understanding of the effect of micro-grinding and dressing parameters and tool specification on grinding forces and surface roughness. This provided experimental evidence of the efficiency of the material removal mechanisms. Moreover, empirical data was also used to verify the process models presented in papers II and VI to explain the material removal mechanism in the micro-grinding process. Using papers III, IV and VII, an ultimate understanding of the micro-grinding process was developed to achieve an optimized, highly efficient, micro-grinding process with a desired surface finished. Moreover, the grindability of additively manufactured vs. conventional titanium was examined.

1.3. Challenges and limitations

During the course of this thesis the following limitation/challenges were experienced:

- Because of the size effect resulting from the size of the micro-grinding tool and fine grinding and dressing parameters, the tool run-out affected the process outputs, which was attempted to be addressed via modeling. Because of the complexity of the tool run-out measurement and modeling, this parameter was not considered in this thesis.
- For process modeling, an ideal shape of the abrasive grain (a spherical form) was assumed, which somewhat simplified the predicting surface roughness and grinding forces.
- The tool deflection was considered as a static deflection. But in practice, the tool is subjected to dynamic forces. Hence, a dynamic tool deflection model is needed to model the grinding forces.
- The microscopic examination of worn tools was not considered in this thesis since the tool was freshly dressed prior to almost each experiment. However, in the micro-grinding process, the tool is subject to wear flat and grain pull-out, but addressing this is complex and deemed out-of-scope, in view of the postulated research questions.
- One of the biggest challenges was measuring the tool deflection during the grinding experiments, therefore the actual depth of cut (removed material depth after grinding) was measured and its difference with the programed depth of cut was taken as the tool deflection.

2. Micro-grinding

Micro-grinding is a material-removal process capable of reaching high dimensional accuracy and creating (geometrically) complex micro-parts. Micro-grinding is positioned last in the manufacturing value chain, which normally generates a finished surface quality and high level of accuracy [10,13]. Achieving a high level of accuracy in the micro-grinding process is challenging, since it can be realized only when highly accurate machine tools with a very high stiffness are available. Moreover, special micro-grinding tools with low or predictable wear rate are needed. The micro-grinding process is able to machine brittle and hard-to-cut materials such as tungsten carbide, ceramics, and aerospace alloys which are normally very hard to machine with other processes like milling[10,14]. However, micro-grinding is distinguished when compared with lapping and polishing processes, as it uses fixed abrasives and has an interrupted contact with the workpiece. Apart from some kinematic similarities between micro and conventional grinding processes, they can be distinguished according to the following:

- In contrast with conventional (macro) grinding processes, micro-grinding offers a high degree of geometric flexibility to produce micro-parts with sophisticated features [15].
- Miyashita [16] introduced the specific material removal rate and the grain size, d_g, to differentiate the conventional and micro-grinding process. He mentioned the material removal rate range of 10^{-4}-10^{-1} $mm^3/mm \cdot s$ and grain size range of 10^{-1}-10^{2} μm for micro-grinding process.
- In the case of brittle materials, the micro-grinding process is performed at the borderline of brittle-to-ductile transition – including both ductile and brittle material removal mechanism. Hence, both ductile paths and cracks and outbreaks over and beneath the finished surface can be expected.
- Micro-grinding cannot only be characterized via the surface and quality criteria, but also by tool and abrasive specifications. Micro-grinding generally employs small grinding tools with very fine abrasives, with high wear resistance and low tool run-out.
- The depth of cut in the micro-grinding process is limited to the micrometer range (for brittle material often in ductile mode). This process is normally performed with a very low material removal rate and limited cutting speed due to the tool size.

The conventional grinding processes are quite well understood. However, a simple characterization of the micro-grinding process is not well-studied. The quality of the finished part, the efficiency of the process, and the mechanical properties of the workpiece material help as preliminary indicators to aid process characterization, selection of optimal/desired process parameters, and cutting tools. However, the challenges (such as the demands on machine tool and environmental conditions) need to be addressed.

2.1. Size effect

There is a general understanding of why the fundamental knowledge, applicable to macro-scaled (conventional) grinding, cannot be utilized in the case of micro-grinding. Understanding the material removal mechanism in micro-grinding is difficult due to the size effect. Because of the relatively larger chip thicknesses in conventional grinding, the share of ploughing and rubbing compared to the material removal is not significant in the material-removal mechanism. However, in micro-grinding the chip thicknesses are much smaller (lower than 2 μm [17] and in some cases in nano range [18,19]) compared to conventional grinding, hence the portion of ploughing and rubbing becomes larger and more significant in the process. For the sake of comparison, in the micro-grinding process, the chip thickness is on the scale of the tip radius of

an abrasive grain. Fig. 3 compares the grain-workpiece interactions in micro and conventional grinding processes [20].

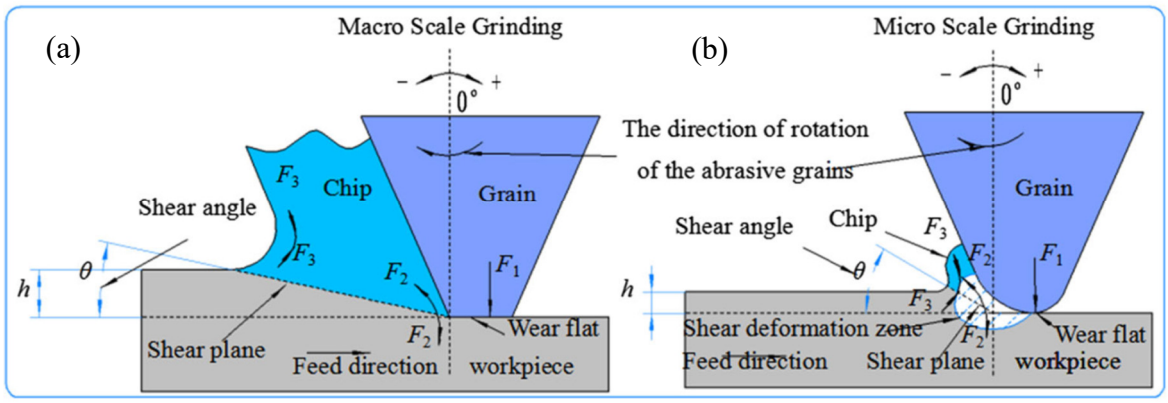

Fig. 3. Model of single abrasive grain material removal. a: Macro-scale grinding model; b: Micro-scale grinding model (h—undeformed chip thickness) (Reprinted by permission from [20]).

Park [21] showed the dependency of the ploughing and cutting forces on the chip thickness. He observed that the share of ploughing becomes significant at small chip thicknesses, which dominates the share of cutting in the micro-grinding process. For instance, the normal ploughing force is around 40% of the overall forces at the smallest chip thickness (where the grinding parameters are very conservative). Increasing the chip thickness by increasing the depth of cut decreases the percentage of the ploughing force and the cutting becomes dominant. A FEM study based on Johnson's indentation theory and specific energy variation was proposed to predict the minimum chip thickness in micro-grinding process. The authors showed that decreasing the tool diameter results in a higher contribution of ploughing and rubbing. Moreover, using higher cutting speeds and lower feed rates (lower chip thicknesses) led to an inefficient micro-grinding process [22].

In the grinding process, there is a certain chip thickness value below which no cutting occurs, i.e. "critical chip thickness". The process implementation requires that the parameters are selected in a way that the resulting chip thickness value is above the critical value (h_{cr}). Three grinding regimes in micro-grinding are hence attainable:

- The uncut chip thickness (h) is smaller than the critical chip thickness ($h < h_{cr}$). In this case, just the elastic deformation in the workpiece occurs but no chipping.
- The uncut chip thickness is equal to the critical chip thickness ($h = h_{cr}$). In this case, the workpiece is slightly deformed, and a small chip is formed. However, because of the material spring back, the actual depth of cut is smaller than the set depth of cut.
- The uncut chip thickness is greater than the critical chip thickness ($h > h_{cr}$). The share of elastic deformation becomes much lower and the actual depth of cut approaches the set depth of cut.

2.2. Micro-tools

In contrast to conventional grinding wheels, which normally have a simple shape with or without complex profiles, the micro-grinding tools may come in a wide variety of shapes and sizes, including irregular shapes (Fig. 4a-g). The micro-grinding tools may be produced via different manufacturing processes, such as Electro Discharge Machining (EDM) [23], laser

[24], electroplating [25], cold spraying [26], as well as the combination of the sintering, brazing, and shaping [2]. According to their shapes, they may also perform differently. In one study carried out by Perveen et al. [23] it was shown that, using a D-shaped tool resulted in lower tangential and normal grinding forces compared to the other shapes; or a better surface roughness was achieved by utilizing the circular tool. In the case of tool wear, the square and triangular tools experienced higher tool wear compared to the circular and D-shaped tools [23]. Moreover, the D-shaped tool showed a better performance in the case of straightness, waviness, and roughness of the drilled holes in tungsten carbide [27]. Producing the predefined cutting edges using laser ablation could also outperform conventional electroplated diamond micro-grinding tools in the case of accuracy. A better surface roughness and durability was accomplished using the new laser-ablated micro-tool [24]. Apart from their shapes, micro-tools may have also different bonding materials shown in Fig. 5.

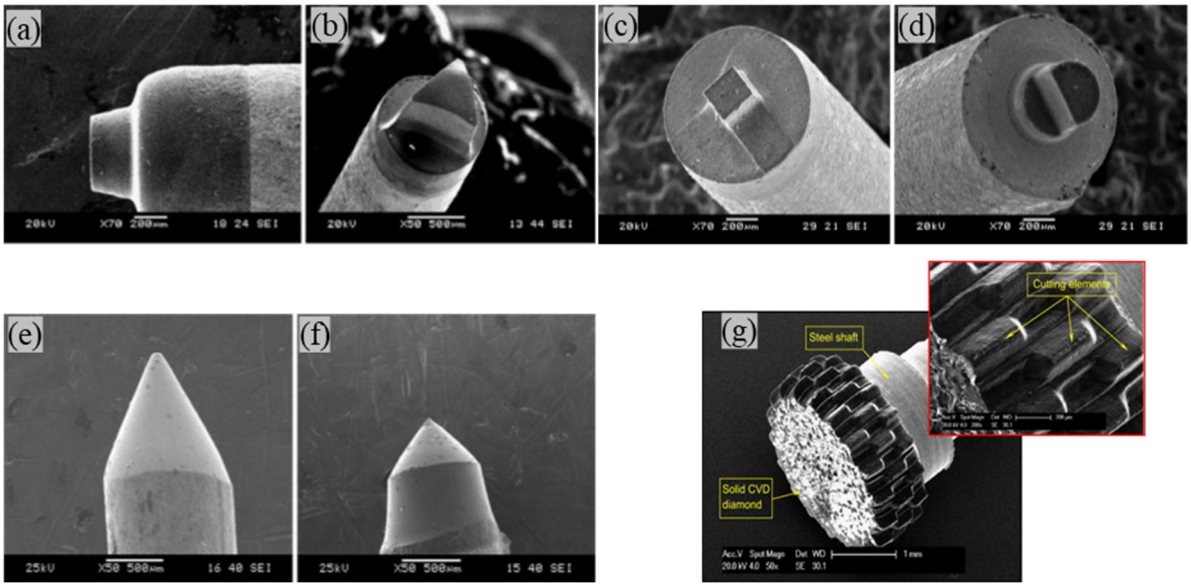

Fig. 4. Micro-grinding tools: a: circular tool; b: triangular tool, c: square tool; d: D-shaped tool; e: conical tool of 60°; f: conical tool of 90° (Reprinted by permission from [23]; and g; unused laser ablated solid diamond micro-grinding tool (Reprinted with permission from [24]).

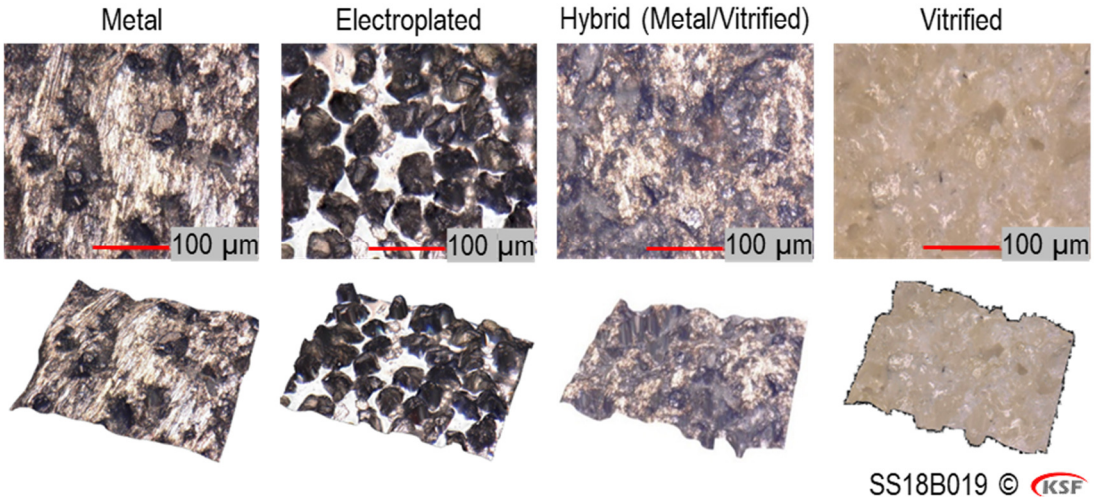

Fig. 5. Tool topography with different boding materials [28].

In terms of size, the micro-grinding tools may range from some micrometers to maximum 2 millimeters [14]. The smallest reported micro-grinding tool was fabricated by Aurich et al. [29] with a diameter of 4 µm (Fig. 6) featuring a diamond grain size of 0.1–0.2 µm. The tool was fabricated on a specially-developed machine tool (i.e. the nano-grinding center) using an electroplating technique. This technology allowed for fabrication and utilization of the manufactured micro-tool without re-clamping.

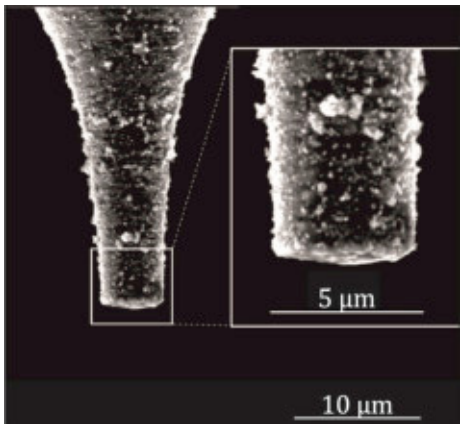

Fig. 6. A 4 µm micro-grinding tool (Reprinted with permission from [29])

2.3. Micro-grinding forces

Micro-grinding forces play an important role in the micro-grinding process. Due to the small size of the micro-tools, micro-grinding forces determine the achievable accuracy of the finished parts due to tool deflection and wear. Moreover, the efficiency of the material-removal process can be assessed using the process forces. Therefore, using the optimal combination of the micro-grinding parameters and micro-tool specification is one of the most important objectives for this research. Micro-grinding forces can be affected by several factors such as tool shape, dressing parameters, tool specification (e.g. abrasive material), work material, as well as process parameters [30]. Cheng et al. [18,19] showed that the micro-grinding forces abruptly change when the chip thickness size comes within the range of the material's crystal boundary. They also found out that the grinding forces increase at the undeformed chip thicknesses lower than 0.5 nm, compared to higher chip thicknesses, as a result of the size effect. Moreover, the {0001} ceramic crystal orientation generated lower grinding forces compared to other directions. They also reported a force ratio between 0.6 and 0.8. The grinding forces can also be affected using the tool shape [31], or tribological conditions. For example, the forces can be reduced using Minimum Quantity Lubrication (MQL) [32]. Utilizing compressed (chilled) air is also a good approach to reduce the forces in case of small depths of cut and low feed rates [33]. Moreover, micro-grinding performance also depends on the type of tool materials. It was reported that the effect of feed rate on the resultant forces is much larger compared to the effect of the depth of cut in the case of micro-grinding of SiCp/Al composites [34].

2.4. Specific grinding energy

One of the most fundamental criteria for evaluating grindability (i.e. the ease to grind) of micro-parts is the specific grinding energy. The specific energy is defined as the energy expended to remove a unit volume of the work material, which is a key indicator of the efficiency of the

grinding process [12]. A larger portion of chipping energy leads to a higher process efficiency; associated with lower specific energy. In the case of micro-grinding, a relatively high specific energy is generally required for the material removal because of high elastic and plastic deformations in the chip formation as well as the friction (rubbing) between the grains and the ground material. This phenomenon is common for all abrasive processes running at a low chip thickness [35]. Therefore, the specific energy is considered as the main grindability parameter. The data on specific energy for micro-grinding is nearly nonexistent. This is in stark contrast to conventional grinding operations, where numerous publications investigate specific grinding energy in a variety of applications. According to the literature review carried out, the specific energy in micro-grinding was only measured by Morgan et al. [36]. This investigation was specific for tungsten carbide and the authors observed that the specific energy at the beginning of the tool-workpiece contact was relatively high and then it dropped rapidly to an almost constant value after the tool engagement (500 J/mm^3). Such specific energy of 500 J/mm^3 is 10 times higher than values associated with the macro-grinding process. For example, Kadivar et al. [17] and Badger [37] reported the specific energies of 32 and 50 J/mm^3 for macro-grinding of tungsten carbide, respectively. In the case of titanium alloys, Guo et al. [38] and Kacalak et al. [39] reported the specific energy in between 12-15 J/mm^3 for conventional grinding.

2.5. Surface integrity

Surface integrity comprises several indicators for grinding quality, describing the properties of surface finish, subsurface microstructure, residual stresses, etc. During micro-grinding, the elastic and plastic deformations, chip formation, and friction between the grains and the workpiece material affects the quality of the finished surface. Additionally, the mechanical work during the material removal process results in compressive residual stresses, while an excessive grinding temperature can cause the onset of tensile residual stresses, which may cause surface and subsurface damages, which negatively affect the performance (e.g. fatigue) of the parts. Therefore, an investigation of the quality of the finished surface is essential.

It was reported that during micro-grinding of nickel-based (single-crystal) superalloy, the workpiece was subjected to high amounts of plastic deformation in the sub-surface and that a hardened layer was observed. Moreover, many dislocation-winding regions, high-density dislocation walls, sub-grain structure, and small-angle grain boundaries were identified in this layer [40]. The study showed that, although the micro-grinding forces are very low, the workpiece experiences a high plastic deformation. Gong et al. [41] and Zhou et al. [42] analyzed the removal mechanism of nickel-based single crystal superalloy. They studied the effect of grinding parameters on microstructure of ground surface and sub-surface. They showed that the most shear-slipping planes are associated with the {111} planes. The thickness of subsurface plastic deformation and surface roughness increased with the feed rate and grinding depth and decreased with increasing the cutting speed. Based on the experimental work of Fook et al. [43], low cutting speed and low depth of cut are the most crucial parameters to achieve optimal surface integrity in micro-grinding of bio-ceramics. Zhang et al. [44,45] studied the surface integrity of amorphized Si during micro-grinding of RB-SiC/Si composites. They showed that recrystallization developed at higher feed rates. At lower feed rates, the surface generation mechanism changed from micro-cracking to smoother surface. Using more aggressive parameters (higher feed rate and depth of cut) resulted in an uneven surface topography of the Al/Si composite materials and more accumulation and adhesion [34]. It was also reported that surface integrity can be improved using MQL in combination with nanofluid-based lubricant via a proper selection of the nano-diamond particle size and concentration [46]. Another way to improve the integrity of the finished part is by controlling the heating rate and strain rate,

which can reduce the transformation phase of material, thus controlling the induced residual stress and the material deformation. Higher strain rates and lower heating rates can reduce the amount of material deformation and phase transformation [47]. Compressive residual stresses were observed while micro-grinding ZrO_2 and ZTA workpieces [48].

2.6. Tool wear

Like macro-grinding processes, tool wear is also an expected phenomenon in the micro-grinding process. Different wear mechanisms may apply for micro-grinding tools [49,50]:

- Wear flat, in this case, the sharp edge of the abrasive grain is worn (grain flattering). This is caused by an attritious process (causing abrasion/flattening).
- Fracture of the abrasive grains. Here the durability of the abrasive grain reaches its ultimate limits and because of the thermal and mechanical stresses, the grains get fractured (e.g. micro-chipping).
- Grains pull-out, in this case, the abrasive grains as a result of the external loads, higher than the bond strength, are pulled-out from the bond layer.
- Wear of the bond. The bonding material is continuously in interaction with the work material and chips. This results in friction and heat generation – damaging the bond material. Thermal shocks further contribute to this type of wear.

Zhou et al. [42] showed that micro-grinding with low cutting speeds, high feed rates and high depth of cuts, led to a higher level of tool wear and that lubrication could improve the tool life. They also observed that the wear flat was the main wear mechanism of the micro-grinding tool in the early stage. Feng et al. [51] monitored tool wear during micro-grinding of ceramics and showed that tool wear monitoring using acoustic emission and force signals is possible. Aurich et al. [29] showed that the smaller the grain sizes and the smaller the grain concentrations, the higher the tool wear. Perveen et al. [23] investigated the tool geometry performance of the tool wear. The tool wear was higher in the case of square and triangular tools compared to circular and D-shaped tools. The performance of different micro-grinding tools, i.e. PCD, CVD electroplated, and vitrified diamond tools were investigated in micro-grinding of monocrystalline silicon workpiece. The results showed that apart from the good performance of the electroplated tool in terms of surface roughness, it was subjected to severe tool wear. The electroplated tool with a small grain size was subjected to grain pull-out as the main wear mechanism [52]. They also found that the effect of cutting speed on tool wear was minimal. Instead, the feed rate was identified as the most influential factor. The main wear mechanism in the micro-grinding process of ductile materials was observed to be the wear flat along with pull-out of diamond grains [52].

2.7. Material removal mechanisms

Generally, the material-removal mechanism of ductile materials such as titanium alloys, nickel alloys, and alloy steels follows a ductile mode cutting, so that a chip is formed due to high plastic deformation and shear in the contact zone. A ductile mode cutting is also appropriate when grinding hard and brittle materials, which could improve the quality of the finished surface [53]. Material-removal mechanism of brittle materials like ceramics is associated with a combination of plastic flow, chipping, and lateral (responsible for material removal) and radial (responsible for material weakening) crack propagation [54]. Therefore, the transition from brittle-to-ductile material removal is an important aspect for a high precision grinding process

with a desired surface quality. This transition is highly connected with the stress conditions around the cutting zone in the work material [10]. As it is already known for conventional grinding operations with a trochoidal path (such as surface and cylindrical grinding) the chip thickness starts from a zero value to a maximum value, as maximum chip thickness, h_m. During the material removal process of brittle materials, up to a certain value of chip thickness, the material removal mechanism is in ductile mode and after that a transition from ductile-to-brittle mode will happen. This value is called a critical undeformed chip thickness ($h_{cu\text{-}crit}$) [3]. The value of critical undeformed chip thickness depends on the type and properties of workpiece material, as given in the following equation [55]:

$$h_{cu-crit} = \beta \left(\frac{E}{H}\right)\left(\frac{K_{Ic}}{H}\right)^2 \quad \text{Eq. 2-1}$$

where E defines Young's modulus, H is the hardness of the material, K_{IC} is the material fracture toughness of the first mode, and β presents a constant (generally equal to 0.15 for brittle materials [56]).

Since the grinding process is a complex material removal process, the critical undeformed chip thickness value can be experimentally established by a single-grain scratch test for different kind of materials. Cheng et al. [57] found that the limit for ductile-brittle transition in single grain scratch test and micro-grinding of single crystal silicon is largely different, since the rake angle has a huge influence on both the brittle fracture and $h_{cu\text{-}crit}$. They also defined critical undeformed chip thickness values for soda lime glass (2 and 5 nm) [58] and silicon (20 and 100 nm) [18]. In the micro-grinding process, using grinding tools with large grain tip radius and higher cutting speeds should increase the chance of ductile-mode cutting [59].

2.8. Modeling of micro-grinding process

As mentioned earlier, the micro-grinding process is distinctive because of the size effect. Therefore, the outputs of micro-grinding like surface quality and grinding forces are more strongly related to the mechanical and thermal interactions between a single grit and the work material. Hence, an analytical description of the single grit-workpiece interaction is critical for better process understanding. This interaction can be quantified by maximum undeformed chip thickness, the effect of ploughing, and friction coefficient. Thus, the grinding process can be better understood via modeling of the chip thickness, which is governed by a multitude of parameters and factors. Since a grinding process involves material removal with a large number of abrasive grains (with geometrically undefined cutting edges) which are randomly distributed over the surface of the grinding tool, it is challenging to model the chip thickness and consequently study material-removal mechanisms. Nevertheless, a probabilistic distribution of cutting edges results in a random distribution of chip thicknesses. Using the statistical approach to chip thickness prediction, modeling the grinding forces and surface roughness is achievable. This prediction can further aid process control and optimization [60].

In view of the above described complexity, there are several ways to model the undeformed chip thickness and to describe grain-workpiece interactions in the grinding process. The undeformed chip thickness can be directly modelled via analyzing the grinding path or by quantifying the balance between the volume of the generated chips and the total material removal rate [12]. Yang et al. [61,62] modeled the chip thickness under different friction coefficients based on the strain gradient, geometrical and kinematical analyses. They showed that the chip thickness in both grinding and single-grain tests of ceramic materials decreased with the increasing of the friction coefficient, μ, and frictional angle, β, ($\mu = arctan\,\beta$). Moreover,

the authors addressed the size effect in their study and concluded that the critical chip thickness is in the border area of ploughing and cutting; but still mainly in the ploughing region. Agarwal and Rao [63] developed a new undeformed chip-thickness model for the grinding of ceramics. This model considered the stochastic nature of the grinding process, i.e. the random geometry and the random distribution of cutting edges. Zhang et al. [64] modeled a wheel topography with the integration ability and the workpiece model, kinematic model, and undeformed chip thickness model. The proposed tool topography model, aided by a single-grain model, could calculate the distribution of undeformed chip thicknesses. In most of the studies, the deformation of the grinding contact zone was not considered. Moreover, none of these analyses took the dressing parameters explicitly into account. Varying the dressing parameters can nonetheless significantly change the number of active cutting edges in the tool-workpiece contact zone, which affects the undeformed chip thickness.

Since the research in the field of micro-grinding is still in its early stage, there are not many modeling-focused studies available. Cheng et al. [65] built a micro-fracture model and established a restraining technique for micro-grinding of glass and also proposed a prediction model for the size of the fractures considering both micro-interaction and elastic strain energy. With the help of the model, they could increase the productivity of the process up to 50 times. Cheng and Gong [18] modeled the process forces considering crystallographic effects in micro-grinding of single-crystal silicon. They used the undeformed chip thickness to connect the process parameters and grinding forces. They found a critical chip thickness that determines a threshold for material-removal effectiveness. Li et al. [66] modeled the grinding forces in detail, including rubbing, ploughing, and cutting forces. In their method, the instantaneous grain-workpiece interaction for each grain was determined. The instantaneous interaction took both random grinding-tool topography and process kinematics into consideration. Cheng et al. [19] presented a predictive model for the grinding force in micro-slot-grinding of single-crystal sapphire. They concluded that the {0001} crystal orientation generated lower grinding forces compared to other directions. They also reported a force ratio between 0.6 and 0.8. They demonstrated that their prediction model could capture the main trend of the grinding forces. A thermophysical model for micro-grinding was presented by Gorodkova et al. [67]. The model was able to predict the cutting zone temperature and the temperature distribution in the workpiece, considering the process parameters as well as the properties of the material.

3. Titanium

One of the materials that gained a lot of attention in micro-manufacturing is titanium. Titanium and its alloys have remarkable properties such as high corrosion resistance, high strength, and ductility compared to the other kind of materials [15] – making it a suitable choice for a wide field of applications like biomedical and healthcare goods [68,69], microfluidic [70], microneedles [71,72], and aerospace [73]. Their machining, however, is associated with various problems. For example, high tool wear due to reactivity of titanium with tool materials, and its low thermal conductivity [74]. High specific energy, work hardening, and burr formation can also be counted as some of the limitations [75]. Fabricating high precision micro-parts from titanium alloys is also very challenging. Their micro-machining is always accompanied by high plastic deformation due to the size effect, high tool deflection as a result of process forces, and rapid tool wear [76–78] which negatively affect the accuracy of micro-parts. The cost-efficient manufacturing of complex 3D-geometries and micro-features in titanium is possible by means of the micro-grinding process. Obtaining tight tolerances in a broad range of materials through this method is also advantageous [79]. Therefore, the fundamental investigations regarding the

application of micro-grinding are considered essential in order to meet the industrial requirements. Fig. 7 illustrates some of the titanium applications in micro-parts.

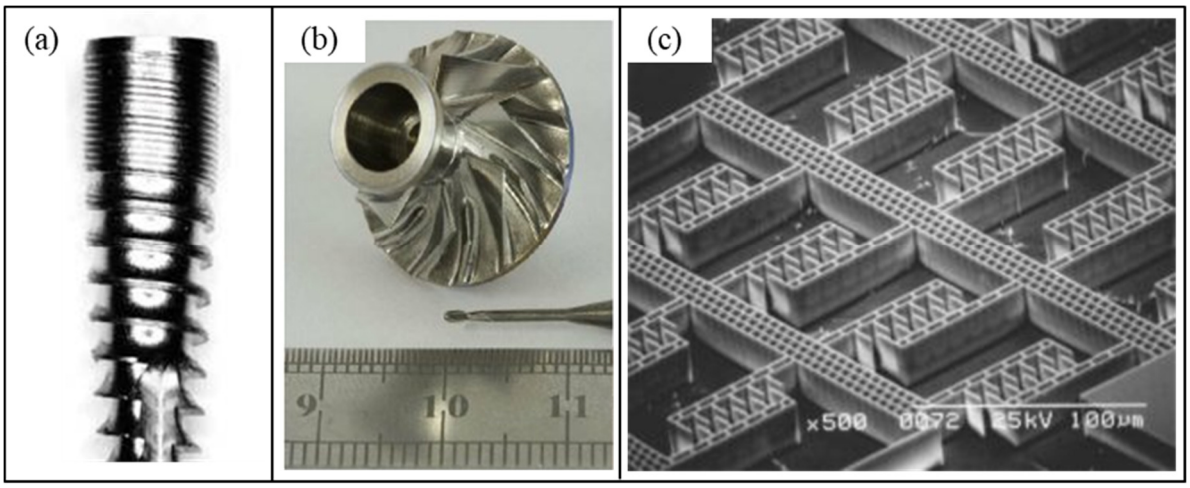

Fig. 7. a: a dental implant (Reprinted with permission from [74]); b: micro-turbine impellers from titanium © 2015 IEEE [80]; and c: scanning electron micrograph of a titanium-based MEMS comb drive structure (Republished with permission from [75]).

4. Ceramics

Among difficult-to-cut materials, silicon nitride (Si_3N_4) is also increasingly becoming popular due to its enhanced mechanical properties. Like titanium, ceramic materials have a broad range of applications, especially in the medical sector, microsystems technology [81], and molding [82] (Fig. 8). However, the brittle nature of advanced ceramics makes these materials particularly susceptible to breaking and the formation of micro-cracks, due to the mechanical stress involved in hard cutting [9,83]. Once introduced, cracks in ceramics lead to a significant loss of tolerable stresses and strength reduction. Furthermore, internal stresses can be introduced into the surface areas by the grinding process. While compressive stresses have a positive effect on the component strength, local superficial tensile stresses are critical [84,85]. The surface quality, marginal zone properties and surface texture also play an important role in the performance of such materials [86].

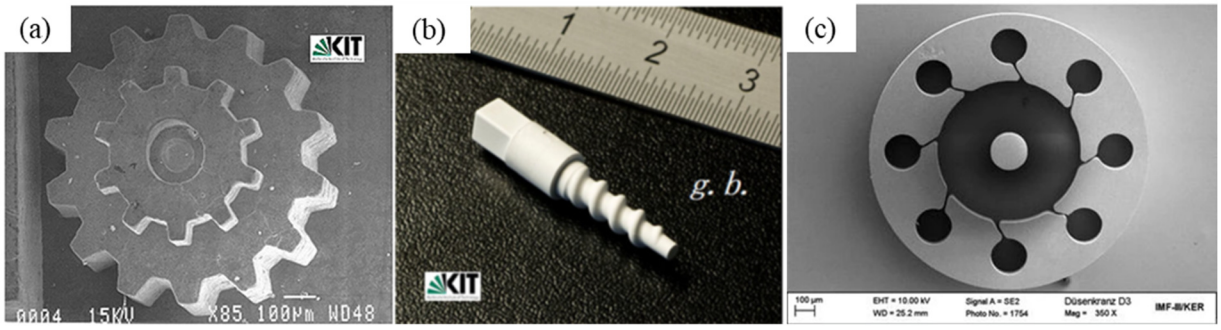

Fig. 8. a: a ceramic micro gear wheel injection-moulded using LIGA mould inserts (Reprinted with permission from [81]); b: a dispenser screw made of ZrO_2 (Reprinted with permission from [81]); and c: SEM image of a nozzle plate made of sintered ZrO_2 (Reprinted with permission from [82]).

5. Experimental details and analysis techniques

In this chapter, the experimental setup, workpiece materials, and experimental parameters as well as work methodology are presented. In this thesis, two materials are chosen: titanium alloy (Ti-6AL-4V) representing a ductile material class and Si_3N_4 ceramic as a representative of brittle material, to investigate the micro-grinding process in both ductile and brittle regimes.

5.1. Workpiece materials

Ti6Al4V

Ti6Al4V grades produced by electron-beam melting (EBM) and wrought were chosen as the ductile workpiece material. The conventional (wrought) material samples had a dimension of 30x20x10 mm, whereas the AM samples were manufactured with a dimension of 30x20x4 mm in two different build-up directions (one parallel to the workpiece length of 30 mm (AM BD 30) and one parallel to the workpiece width of 20 mm (AM BD 20)). The chemical composition of the material is listed in Table 1.

Table 1. Chemical composition (wt%).

Al	V	C	Fe	O	N	H	Ti
6	4	0.03	0.1	0.15	0.01	0.003	Bal.

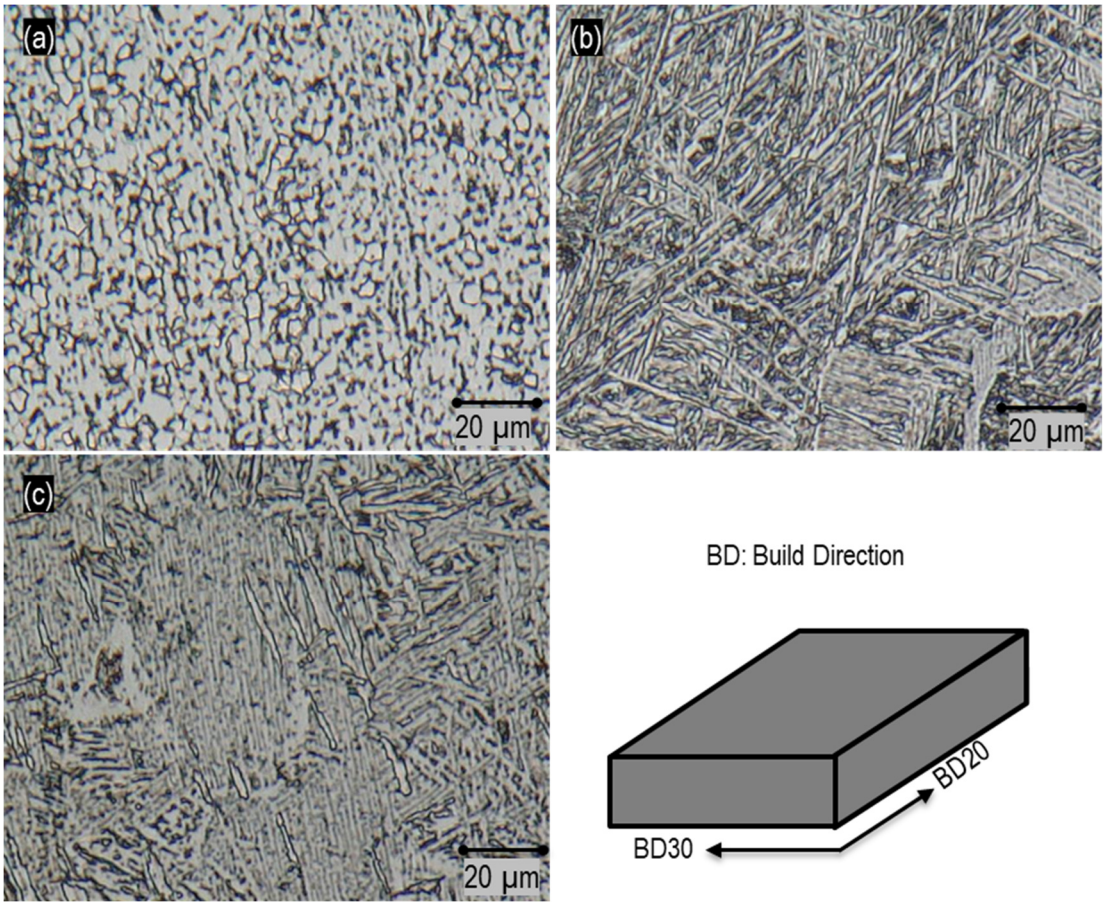

Fig. 9. The microstructure of a: conventional; b: AM BD30; and c: AM BD20 Ti6Al4V.

The samples were polished and etched for approximately 30 seconds using Kroll's reagent etchant (1–3 ml HF, 2–6 ml HNO_3, 100 ml DI water). The microstructure of the samples was investigated using an optical microscope. The microstructure of the AM material (shown in Fig. 9) reveals a thin, acicular fine α-phase located perpendicular to each other (martensitic structure); however, the conventional part consisted of elongated alpha with intergranular beta, β. This highlights that the microstructure is highly dependent on the manufacturing method as a result of different cooling rates. After polishing and etching, the Vickers HV0.1 microhardness was measured. The results were: for AM BD20, HV0.1 = 352±12; for AM BD 30 HV0.1 = 345±10. The conventional part has a microhardness of 340 HV±5. Based on these measurements, we can conclude that all material samples have almost the same Vickers hardness.

Ceramic

As a brittle material, a Si_3N_4 material containing < 5 wt.% Al_2O_3 and 5 wt.% Y_2O_3 in the form of block (30x20x10 mm) was chosen. The material had a Young's modulus of 310 GPa, Vickers hardness HVA of 1650, and Flexural strength of 850 MPa.

5.2. Grinding tools

Four diamond micro-grinding pins (D46 C150) with different bond materials (vitrified, hybrid, metal, and electroplated) were used. These four bonding types are the most commonly used in the industry, therefore, the author used these types for his study. Fig. 5 shows the grinding pins topography for 4 different pins. The diameter of the tool was 2 mm. Table 2 lists the tools′ specifications.

Table 2. Tools specification.

Producer	Bond type	Grain size [µm]	Concentration	Tool size D×T×L
Meister Abrasives	Vitrified	D45	150	2×4×40
	Hybrid			
Haefeli	Metal			
Effgen	Electroplated		-	

5.3. Tool preparation

The micro-grinding pins were dressed using a Dr. Kaiser C72FCA dressing spindle and a diamond form roller with a diameter of 100 mm. Only the metal and hybrid bonded micro-pins were sharped, using an aluminum oxide stick after the dressing process. The sharpening parameters for each tool were set so that the same grain protrusion for both materials was achieved. This was controlled using the confocal microscope, which was integrated into the grinding machine. The sharpening parameters were set at a feed rate of 300 mm/min, a cutting speed of 10 m/s, and depth of cuts 70 and 400 µm for hybrid and metal bonded tools, respectively.

5.4. Micro grinding test

Two different micro-grinding approaches were considered in this thesis. The first approach is Conventional Micro-Grinding (CMG) for both titanium and ceramic materials and the second

one is hybrid machining, namely Laser-Assisted Micro-Grinding (LAMG) for ceramic micro-grinding.

5.4.1. Conventional Micro-Grinding (CMG)

The CMG tests were carried out on a high precision 5 axis micro-machine center KERN Pyramid Nano (Fig. 10) at different cutting speeds (v_c), feed rates (v_w), depth of cuts (a_e) (feed-rate-to-depth-of-cut ratios (v_w/a_e)), dressing feed rates (v_{ftd}), and dressing speed ratios (q_d). A peripheral up-grinding procedure was used to carry out the experiments in such a way that a width of 20 mm was ground (Fig. 10c). The micro-grinding tests were completed under grinding oil as a lubricant.

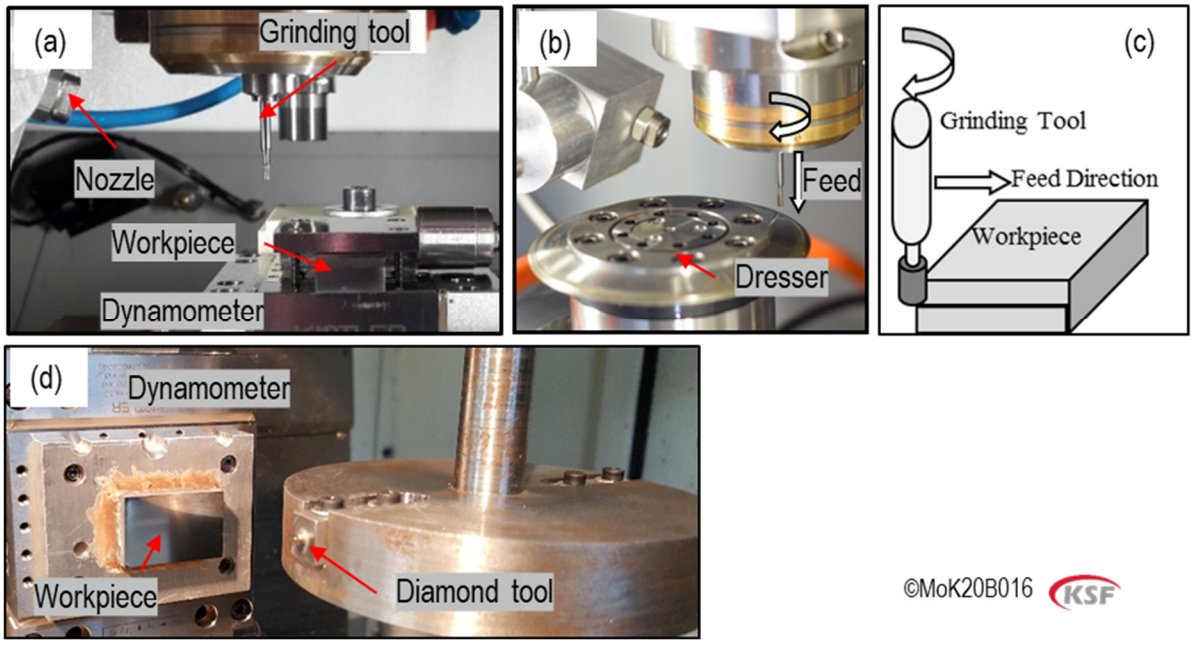

Fig. 10. a: experimental setup for the micro-grinding process; b: dressing unites and kinematic; c: schematic of peripheral surface micro-grinding; and d: experimental setup for single grain tests.

5.4.2. Laser Assisted Micro-Grinding (LAMG)

The approach of hybrid machining (LAMG) was divided into two categories, tool structuring and workpiece structuring by means of an ultra-short pulsed laser. For tool structuring, a femtosecond laser (TRUMPF TruMicro 5050 in the Femto Edition) was integrated into a high micro-grinding machine (KERN Pyramid Nano) (Fig. 11). This laser is an Ultra-Short Pulse Laser (USPL) with a mean laser power of 40 W. The maximum pulse energy is 200 µJ, the pulse duration of 900 fs. However, the workpiece structuring took place outside of the CNC machine. A specially developed setup [83] with an integrated Yb:YAG picosecond (TruMicro 157 5050 manufactured by Trumpf) laser was utilized for this purpose. The tool was structured by proven/optimized laser parameters [4], through which minimum damages on the abrasive grains and bonding material were obtained. To this end, the findings from previous studies were used [87–89]. The tool surface was structured by about 10%. The workpiece was lasered with a structure proportion of 30%. It means 30 percent of the workpiece surface area was removed by the laser ablation. The structure depth was around 90 µm. The laser beam was directed into the machining area via aligned deflecting mirrors. Fig. 11 shows the structure of the laser beam guide. The setup consists of several components for attaching the mirrors and the lens for fast

clamping and precise positioning. The grinding tool used in LAMG approaches was an electroplated diamond grinding tool. The grinding experiments were performed under three different cutting speeds (v_c) of 6, 10, and 14 m/s, a constant depth of cut (a_e) 3 µm, and feed rate (v_w) of 10 mm/min. Each grinding test was completed in 3 passes.

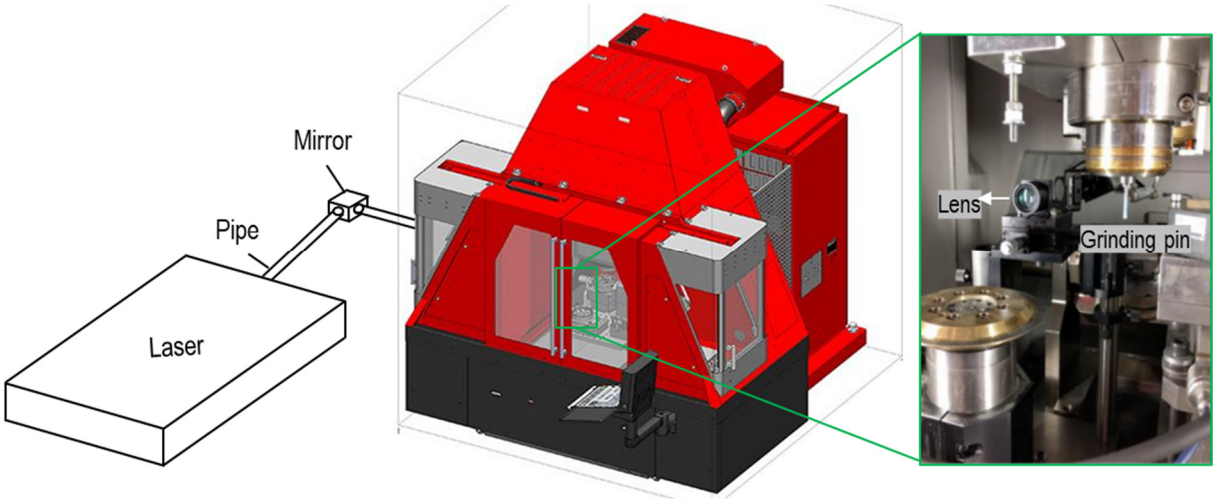

Fig. 11. Experimental setup for tool structuring in the machine center.

5.5. Single grain test

In order to have a better understanding of the fundamental material removal mechanism of titanium, single-grain tests were carried out. The single-grain tests were performed on a Müga CNC milling machine (Fig. 10d). The experiments were carried out under dry and flood conditions (grinding oil). A fixed feed rate of 5000 mm/min was used to avoid overlapping of the scratches. A diamond grain with a pre-defined conical form, a tip diameter of 100 µm, and a conical angle of 120° was used. Prior to the tests, each material was polished to achieve a mirror surface. The process parameters for both the micro-grinding and single grain tests are listed in Table 3.

Table 3: Process parameters.

Parameters	Values
Micro-grinding tool	D45-46-V-M-H-E-150 and - 200
Workpiece	Titanium grade 5 (Ti6Al4V) and Si_3N_4
Cutting speed (v_c) for micro-grinding	6, 10, 12 and 14 m/s
Cutting speed (v_c) for single grain test	4, 6, and 10 m/s
Feed rate to depth of cut ratio (v_w/a_e)	5, 8, and 11 (x10^4 mm/mm.min)
Depth of cut (a_e)	1, 3, 4, 5, 10 µm
Feed Rate (v_w)	200 and 1000 (mm/min)
Axial depth of cut (a_p)	3.5 mm
Coolant for micro-grinding	Grinding oil
Coolant for single grain test	Dry, grinding oil
Dressing feed rate (v_{fid})	50, 150 and 300 mm/min
Dressing speed ratio (q_d)	-0.8, -0.4 and 0.8
Dressing depth of cut (a_{ed})	3x2 µm

5.6. Analysis technique

5.6.1. Micro-grinding forces

The grinding forces were measured and analyzed using a Kistler type 9256C2 three-component dynamometer which is suitable to measure the micro-cutting forces [90]. The dynamometer was connected to a type 5015 amplifier and the signals were recorded via a LabView software. A low-pass (LP) filter was used to filter noise and extract the real micro-grinding forces.

5.6.2. Surface integrity

The surface integrity of the ground workpieces was analyzed using SEM, with the radiation penetration depth of 5 µm and XRD techniques of the StressTech GmbH company. In order to investigate the surface integrity of the parts, prior to each trial, each workpiece was ground with conservative grinding parameters (a_e = 1µm, v_w = 50 mm/min and v_c = 6 m/s) with a total depth of cut 50 µm, inducing low grinding forces and temperature.

5.6.3. Surface topography and roughness profile

The surface topography (both the grinding tool and workpiece) were measured using a mobile confocal microscope (NanoSurf) which was integrated within the CNC machine. The surface roughness measurements were taken perpendicular to the grinding direction at three positions: at the beginning, at the middle, and at the end of the grinding path, with a sampling length of 4.8 mm, cut-off length λ_c of 0.8 mm, and sample length to evaluation length λ_c/L of 0.8/4 mm. The average of these three measurements was chosen as the value of surface roughness.

6. Modeling

In this thesis, three models were developed to predict the grinding forces and surface roughness for titanium, and the laser ablation depth for Si_3N_4 material.

6.1. Thermal analysis of laser structuring of Si_3N_4

For the workpiece structuring, it is very important to use proper laser parameters corresponding to the desired structure dimensions. The depth of the laser cut is related to the laser input energy density and almost independent from the laser type (with the same wavelength). The areal density of laser input energy can be expressed as [91]:

$$E_{L-input} = \frac{E_{L-total}}{A_{L-total}} \qquad \text{Eq. 6-1}$$

where $E_{L-total}$ is the total laser energy and $A_{L-total}$ is the total structured area. It contains the effects of laser structuring parameters, i.e. laser power (P_L), laser scan speed (v_L), laser line-width (w_L) and laser line-span (d_L). Thus, Eq. 6-1 can be re-written as:

$$E_{L-input} = \frac{P_L}{(d_L + w_L) \cdot v_L} \qquad \text{Eq. 6-2}$$

In this work, workpiece structuring by laser ablation was simulated using the "Comsol" software. For the simulation input, the workpiece material Si_3N_4 with 200 µm radius and 275 µm thickness was defined with the properties listed in Table 4 [4].

The heat flow was applied after 10 ps in the center of the sample. Since the frequency of the laser is 400 kHz, there are 2.5 µs rest time periods between two laser pulses. Hence, a sequence of 2.5 µs must be considered for heat input between two consequent laser pulses. The simulation showed that the material temperature rises when the laser beam is radiated on the workpiece surface for the pulse duration of 10 ps. The material is then cooled during the rest time of 2.5 µs at the ambient temperature [4].

Table 4: The simulation input parameters.

Parameter	Value
Heat capacity, C_p [J/kg·K]	700
Density, ρ [kg/m^3]	2329
Thermal conductivity, k [W/m·K]	130
Thermal expansion, λ [1/K]	2.6×10^{-6}
Young's modulus, E [Gpa]	170
Poisson ratio, υ	0.28
Laser radiation frequency [kHz]	400
Radius of the laser beam [µm]	50
Pulse energy [µJ]	125
Pulse duration, p [ps]	10
Laser type	Picosecond laser

The thermal distribution area over the surface of the workpiece is very small and limited to the laser focus area. The temperature rises directly in the center of the workpiece (almost 10000 K), which is much higher than the material boiling temperature (3000 K [92]). After 2.5 µs rest time, the material is cooled down in the ambient temperature and the maximum temperature in the center drops to about 1750 K. Throught the sequential pulse beams, the material temperature rises. Around the time of 2×10^{-12} s, the workpiece temperature exceeds 10000 K. As mentioned, in steady-state conditions, the material sublimates at a temperature higher than 3000 K. In the sublimation, the material transforms from the solid state to gas state. Over 10000 K, the material converts to the plasma phase [92]. Therefore, it is expected that the material sublimation on the surface of the workpiece begins in less than the 2×10^{-12} s. The ablation process starts on the surface of the workpiece. The instantaneous depth of ablation depends on three parameters: depth of laser absorption into the material (about 20 nm [93]), speed of heat propagation inside the material, and kinetic phase transformation in melting, evaporation, and sublimation of material [94]. On the other hand, according to the other studies [83,91,95] and in the case of USPL radiations, the Multiple Photon Ionization (MPI) mechanism can be the dominant ablation mechanism, depending on the laser intensity. Supposing that 100% of laser energy is to be absorbed by the workpiece material as thermal energy, the elevation of workpiece temperature is the maximum possible value over the surface. A temperature of 3000 K was set in the simulation as a threshold for the material ablation. Depending on the number of laser pulses emitted to a certain point on the material, the temperature may rise above the boiling temperature – causing material ablation. The simulation was performed to achieve optimal laser parameters to structure the workpiece with a certain depth of cut, which is slightly smaller than the micro-grinding depth of cut. As shown in Fig. 12, the depth of ablation matches well with the experimental result of ablation on the workpiece [4].

Fig. 12 shows the depth of laser ablation for the simulation and experiment after 10th, 20th, and 40th laser pulses. The ablation depths obtained from the simulation are 16, 19, and 24 µm after 10th, 20th, and 40th laser pulse, respectively. The workpiece was structured via laser with the equivalent parameters used in the simulation. The laser-cut depths were measured by a light

microscope from Keyence. The actual laser-cut depths in the experiments are 17±3, 19±3, and 22±3 µm which are in very good accordance with the simulation results. The experiments were carried out three times for each laser parameter and the mean values were reported. With the simulation model, it is possible to determine the number of laser pulses required for a certain material ablation and laser-cut depth. Having the number of laser pulses, the scan speed of the laser to generate a laser line cut can easily be found.

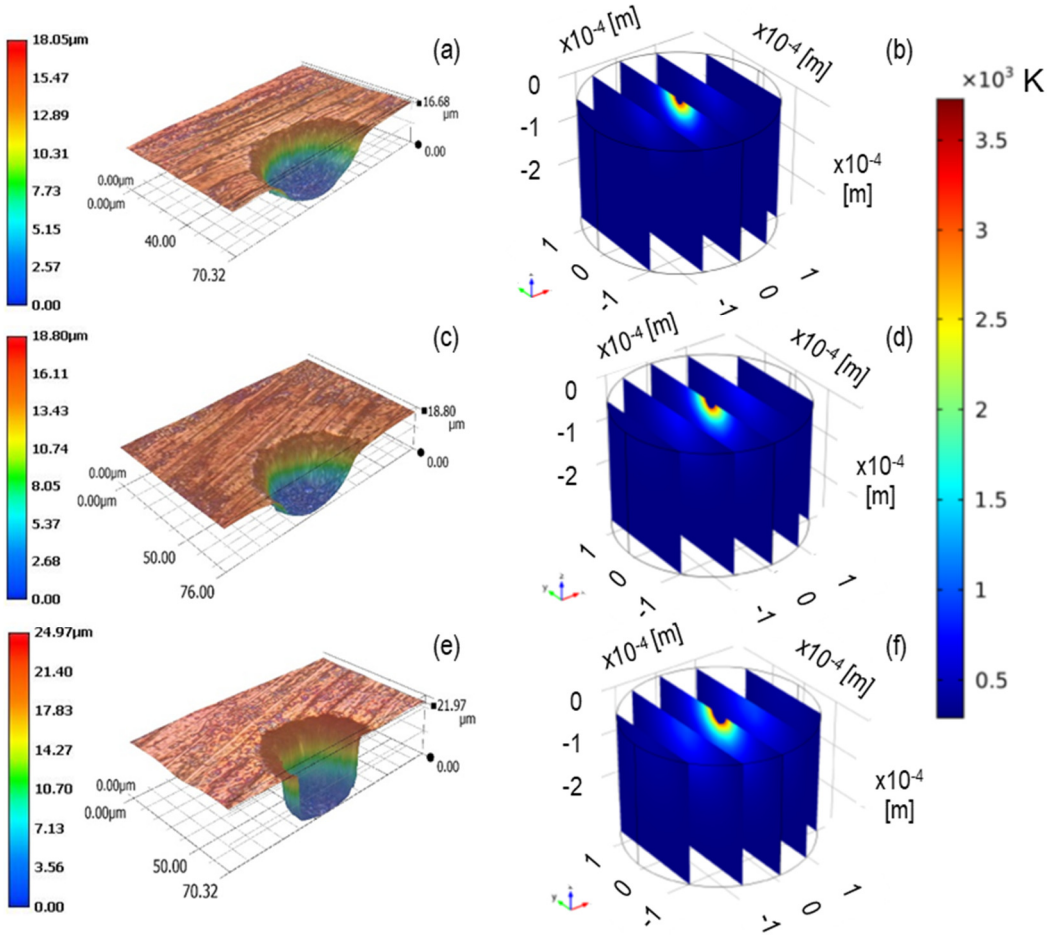

Fig. 12. Comparison between the simulation of ultra-short pulsed laser ablation of Si_3N_4 and experimental results a: experimental after the 10th pulse; b: simulation after the 10th pulse; c: experimental after the 20th pulse; d: simulation after the 20th pulse; e: experimental after the 40th pulse; and f: simulation after the 40th pulse.

6.2. Modeling of the surface roughness

To model the surface roughness, the grinding tool was modeled according to the real position of the abrasive grains on the actual grinding tool. For this purpose, several confocal pictures of the grinding tool surface were taken. After taking the pictures, several sections were analyzed in detail and the position and protrusion height distribution of each single grain was extracted and used to model the grinding tool. The height of the grains was determined according to an approach presented in [96], based on a Gamma distribution function. The scale and shape parameters of the distribution function were defined accordingly, to fit the obtained confocal images of the extracted sections. The whole grinding tool surface was constructed by extending the modelled section of the tool surface to its whole width and periphery. According to Shaw [97], it was assumed that the tips of the grains have a spherical shape. The distribution of the grains and the grain-workpiece interaction can be defined by the position of each grain on the

virtual grinding tool. By expressing the coordinates of the cutting grains (X_i, Y_i, Z_i) and the individual points on the workpiece surface (X_j, Y_j, Z_j) in a global coordinate system on the workpiece, the grain-workpiece engagement can be characterized and interpreted according to a regression model. The engagement criteria of the i^{th} grain can be hence expressed as:

$$(X_i - X_j)^2 + (Y_i - Y_j)^2 + (Z_i - Z_j)^2 < \left({}^{d_{gi}}/_{2}\right)^2 \quad \text{Eq. 6-3}$$

where d_{gi} is the diameter of the i^{th} simulated grain. The equation expresses the instantaneous distance between the points on the workpiece surface and individual cutting grains. In case of engagement (when Eq. 6-3 holds), the grinding force components and the workpiece surface topography are calculated – taking into account engagement depth, grain size, and cutting speed. The proposed procedure is applied to all grains in the tool-workpiece contact zone instantaneously. This model time-dependently modified the topography of the workpiece surface based on an individual grain-workpiece interaction. Therefore, after the calculation of the grain engagements (Eq. 6-3) and corresponding forces, the workpiece surface is also modified. This procedure results in the generation of the workpiece surface profile influenced by all cutting grains throughout the grinding process. A Matlab code was specifically generated for the modeling of the tool surface and the time-dependent simulation of the grinding process (force and workpiece surface).

6.3. Modeling of grinding forces

6.3.1. Modeling of single-grain forces

In a grinding process, the resultant forces for every single grain (the grain which comes in contact with the workpiece) can be aggregated to the whole grinding zone in order to model the grinding forces. Therefore, the tangential and normal grinding forces ($F''_{t,n}$) can be expressed as a function of single-grain forces, considering the dynamic cutting-edge density (C_d) and the real grinding tool-workpiece contact length (l_c). Here, the indentation test was used to define the single grain forces, according to Shaw [97]. To this end, the indentation force in the Brinell hardness test was combined with the single-grain test (Eq. 6-4).

$$BHN = \frac{2F''}{\pi \cdot D \cdot (D - \sqrt{D^2 - b^2})} \quad \text{Eq. 6-4}$$

The load in Brinell test (F'') is assumed to be the acting force on each abrasive grain in the grinding process, where D is the indenter diameter (the diameter of the diamond tool in the single-grain scratch test had a predefined form with a spherical tip), and b defines the impression diameter. In the grinding process, first the spherical grains indent the workpiece – generating plastic deformation, similar to in the Brinell hardness test. The abrasive grains then move in the horizontal direction. This horizontal movement pushes the plastically deformed zone in the front of abrasive grains (plowing) and shears the material and produces chips – acting as an extrusion process [97]. This horizontal movement also generates a friction force between the abrasive grain and material as well as the generated chip. Therefore, the tangential and normal grinding forces can be calculated as a combination of the single grain force from the Brinell hardness test and friction coefficient, μ.

The strain rate used in the Brinell hardness test is very low and the abrasive grains in the real process are not perfectly sphered. Additionally, high temperatures in the cutting zone may cause material softening and consequently lower cutting force needed for the grain indentation.

Hence, to calculate F'' the empirical factor of d_f is added to Eq. 6-4. Therefore, the F'' can be calculated using the following equation:

$$F'' = d_f \frac{\pi \cdot D \cdot BHN}{2}(D - \sqrt{D^2 - (D \cdot \sin(\alpha))^2}) \qquad \text{Eq. 6-5}$$

The friction coefficient, μ, and the empirical factor of d_f can be determined from the single-grain test on titanium alloy. The following flowchart (Fig. 13) shows the algorithm to calculate the single grain forces.

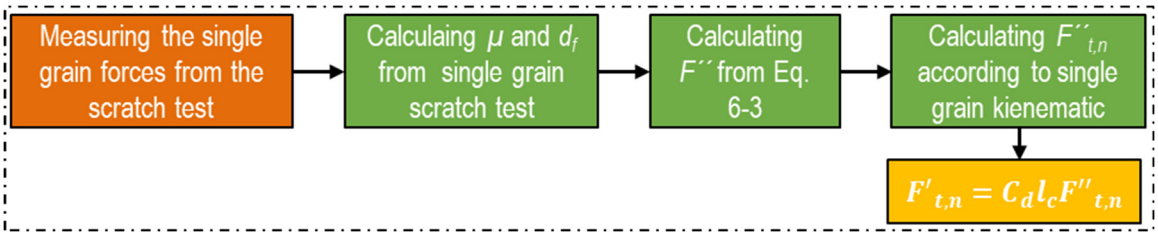

Fig. 13. The algorithm to the establishment of the single grain forces.

6.3.2. Modeling of dressing process

The static number of the cutting edges quantifies the micro-topography of the grinding tool and changes with varying dressing parameters. The consideration of dressing parameters in grinding force modeling is typically not explicitly considered. To model the grinding forces, the number of static cutting edges versus the radial position into the abrasive tool for different dressing parameters, i.e., dressing overlap ratio, U_d, and speed ratio, q_d, is considered. The dressing overlap ratio defines the number of sequences for which every peripheral line over the surface of the grinding tool comes into contact with the dressing tool in the axial direction. The higher this value, the higher the number of sequences and the lower the dressing feed rate. In rotary dressing, the dressing speed ratio is the ratio of periphery speed of the dresser and the grinding tool. The dressing speed ratio can be categorized in up-dressing for the values lower than zero ($q_d < 0$) and down-dressing for the values higher than zero ($q_d > 0$).

To this end, several grinding tools were dressed with various dressing parameters and for each grinding tool, the whole surface of the grinding tool was captured via a confocal microscope. From each obtained image, grain tip diameters and the number of static grains were counted and measured in different radial depths into the tool (z) from the highest point (zero point). The increment of 1 µm was chosen for the measurements. From the measurements, an average grain tip (cutting edge) diameter was selected for modelling, which is used to calculate the conical angle of the abrasive grain. A Gaussian Process Regression (GPR) was used to model the static number of the cutting edges. GPR is a non-parametric regression technique. In addition to predicting the response value for given predictor values, GPR models optionally return the standard deviation and prediction intervals. The method is effective even with a small number of experimental data and can provide estimates of uncertainties.

6.3.3. Modeling of chip thickness

To determine the chip thickness in the micro-grinding process, first the density of dynamic cutting edges, C_d, must be determined. C_d is a function of static cutting edges density, C_s, and process parameters i.e., cutting speed, depth of cut, and feed rate. Simultaneously, the C_d is also influenced by the cutting force acting on every single grain because of the tool deflection. In

micro grinding, the static cutting-edge density, measured in the micro-grinding tool, changes according to Eq. 6-6 with the radial position into the tool (z) from the measurements:

$$C_{s(z)} = A \cdot e^{kz} \quad \text{Eq. 6-6}$$

where A and k are constants, and z is the radial distance into the tool. To obtain the A and k constants, firstly the static cutting-edge density at different z and dressing parameters was modeled using the GPR model.

The dynamic cutting-edge density, $C_{d(z)}$, is a function of static cutting-edge density at height z and process kinematics. The dynamic cutting-edge density is lower than the $C_{s(z)}$. In the grinding process, after each abrasive grain-workpiece engagement, a slot is cut and a 3D space including valleys (voids) and pile-ups are left along its moving path. Then, the next grain comes into contact with the workpiece. The new grain either removes some material along its moving path or traverses between the valleys (voids) generated by the previous grains. It highly depends on the protrusion height and position of each grain on the grinding tool surface. In fact, not all static cutting grains contribute to material removal. Hence, the number of dynamic cutting-edges is always lower than the static numbers. Therefore the $C_{d(z)}$ can be defined geometrically according to removed material as:

$$C_{d(z)} = C_{s(z)} \cdot (1 - \frac{V_{valley}}{V_{tot}}) \quad \text{Eq. 6-7}$$

here V_{valley} is the volume of the valleys (voids) left behind the active cutting edges, and V_{tot} defines the total volume of the grain-workpiece engagement.

The grinding tool consists of several abrasive grains which are stochastically distributed over the surface of the grinding tool. Hence, the chip thickness as a function of the tool topography can be determined via probability approaches. Younis and Alawi [98] used the Rayleigh probability density function for random distribution of the cutting edges as:

$$\begin{cases} f(x,\delta) = \frac{x}{\delta^2} \cdot e^{(\frac{-x^2}{(2\delta^2)})} & x \geq 0 \\ 0 & x < 0 \end{cases} \quad \text{Eq. 6-8}$$

In the Rayleigh function above, δ indicates a scale parameter of the distribution in x, which can be expressed as:

$$E(x) = \sqrt{\frac{\pi}{2}} \cdot \delta \quad \text{Eq. 6-9}$$

To apply this function to the modeling of grinding tool and chip thickness, the value of x can be replaced by the undeformed chip thickness h in grinding. On the other hand, the chip thickness is related to the kinematics of the process including the main process variables. To define the distribution of the chip thickness, just those depths of engagements (chip thicknesses) must be considered which contribute to the material removal ($h>h_{cr}$). Thus, from the kinematics of the process, and assuming the chip with a triangular cross-section, Hecker et al. [99] defined the Rayleigh parameter of δ for the chip thickness as [99]:

$$\delta = \sqrt{\left(\frac{a \cdot v_w}{2v_c}\right) \cdot \left(\frac{1}{l_c \cdot C_d}\right) \cdot \left(\frac{1}{\tan\theta} - \frac{h_{cr}^2}{2}\right)} \quad \text{Eq. 6-10}$$

where h_{cr} is the critical chip thickness obtained from the single grain test, which is 0.4 µm for Ti6Al4V and θ expresses the conical angle of the grain, which changes with varying the

diameter of grains tip (here the average of grain's tip diameter). Using the parameter δ the expected chip thickness, h, and its standard deviation can be respectively calculated. The parameters of l_c, h and C_d are simultaneously updated and recalculated. The real tool-workpiece contact length, l_c, can be calculated using the following equation [100]:

$$l_c = (a_e \cdot d_e + 8R_r^2 \cdot F_n' \cdot d_e(K_s + K_w))^{0.5} \qquad \text{Eq. 6-11}$$

R_r is a surface roughness constant in the contact zone which is taken to be equal to 5 in this study [97], d_e indicates the tool diameter, a_e shows the depth of cut, and K_s and K_w are tool and workpieces stiffness.

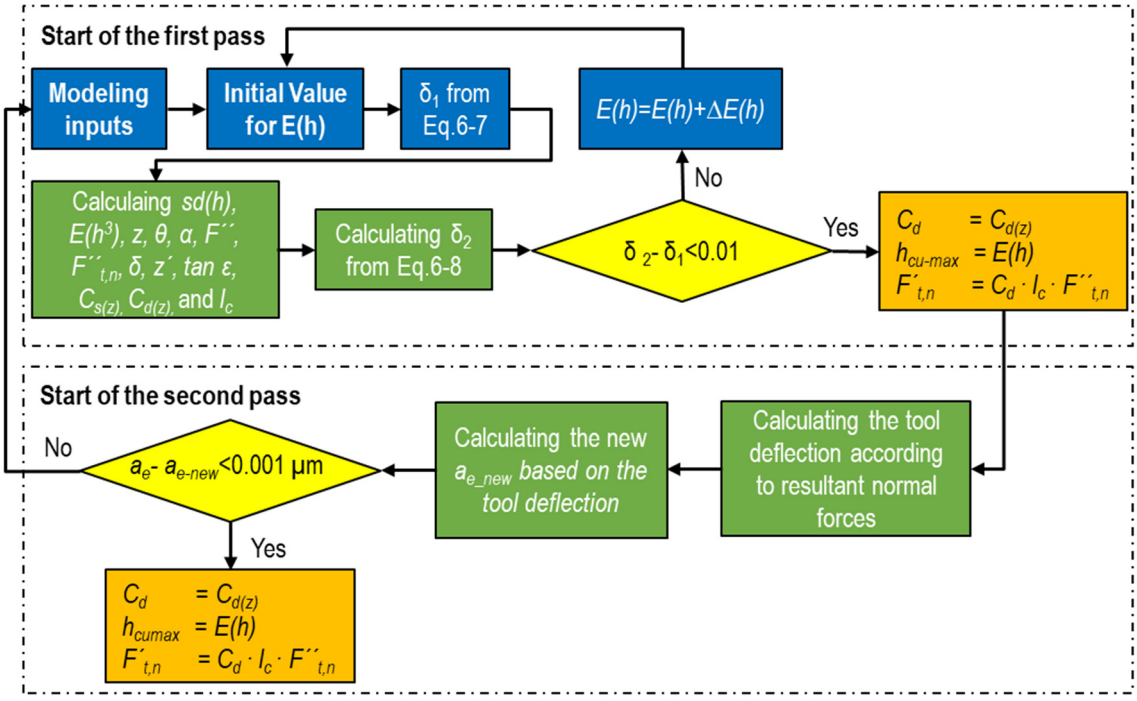

Fig. 14. Computational algorithm to predict grinding forces and tool deflection.

The dynamic cutting-edge density – dependent on the chip thickness and tool-workpiece contact zone – can be calculated using the above equations. To solve the equations, first an initial chip thickness value (0.1 µm) was assumed for the p.d.f to predict the chip thickness using the C_d function. Using Matlab and by means of a loop function, the chip thickness was changed incrementally to modify the value of chip thickness and C_d. After the loop was successfully finished calculating the C_d, l_c, and forces for each single grain, the specific tangential (F'_t) and normal (F'_n) micro-grinding forces for the whole grinding tool were calculated. After calculating the forces based on the actual depth of cut, the tool deflection was predicted and, correspondingly, the depth of cut was corrected. The modified depth of cut was returned to the loop and the new chip thickness and corresponding specific grinding forces, based on the deflection of the grinding tool, were calculated. The flowchart in Fig. 14 shows the modelling algorithm.

6.3.4. Modeling of tool deflection

The micro-grinding tool acts as a cantilever beam where the end of the tool is firmly clamped in the tool holder. The tool is subjected to a nonuniform load at its end, during the grinding process. Since the grinding forces are applied in two different directions (tangential and

normal), the tool deflects in both directions. However, only the deflections in normal direction were considered in this study, since the tool is fed in the normal direction. The tool shaft was made of solid carbide with the E-Modulus of $6x10^6$ N/mm^2. To calculate the tool deflection accurately, the tool was divided into different geometrical segments, including the cylindrical section of the shaft, the taper, the free length, and the abrasive layer. The specific normal force applies to the abrasive layer.

The total tool deflection, including the partial deflections of all sections, can be calculated using Euler–Bernoulli's beam theory. It is assumed that a concentrated force is applied to the middle of the grinding width a_p, which is the normal force (F_n) calculated from the first grinding pass with the actual depth of cut. According to the Euler–Bernoulli's beam theory, the relationship between the tool´s deflection and the applied load was expressed in this thesis as:

$$d_z = \frac{F_n \cdot L_s^3}{3E \cdot I_s} + \left(\frac{F_n \cdot L_c^3}{3E \cdot I_c} + \frac{F_n \cdot L_s^2}{2E \cdot I_s} \cdot L_c\right) + \left(\frac{F_n \cdot L_f^3}{3E \cdot I_f} + \left(\frac{F_n \cdot L_s^2}{2E \cdot I_s} + \frac{F_n \cdot L_c^2}{2E \cdot I_c}\right) \cdot L_f\right) + \left(\frac{F_n \cdot L_b^3}{3E \cdot I_b} + \left(\frac{F_n \cdot L_s^2}{2E \cdot I_s} + \frac{F_n \cdot L_c^2}{2E \cdot I_c} + \frac{F_n \cdot L_f^2}{2E \cdot I_f}\right) \cdot L_b\right) \quad \text{Eq. 6-12}$$

where $I_{s,c,c,b}$ are the area moments of inertia of the tool's cross-sections. These sections, along with the actual micro-grinding tool, and the resultant deflection are shown in Fig. 15.

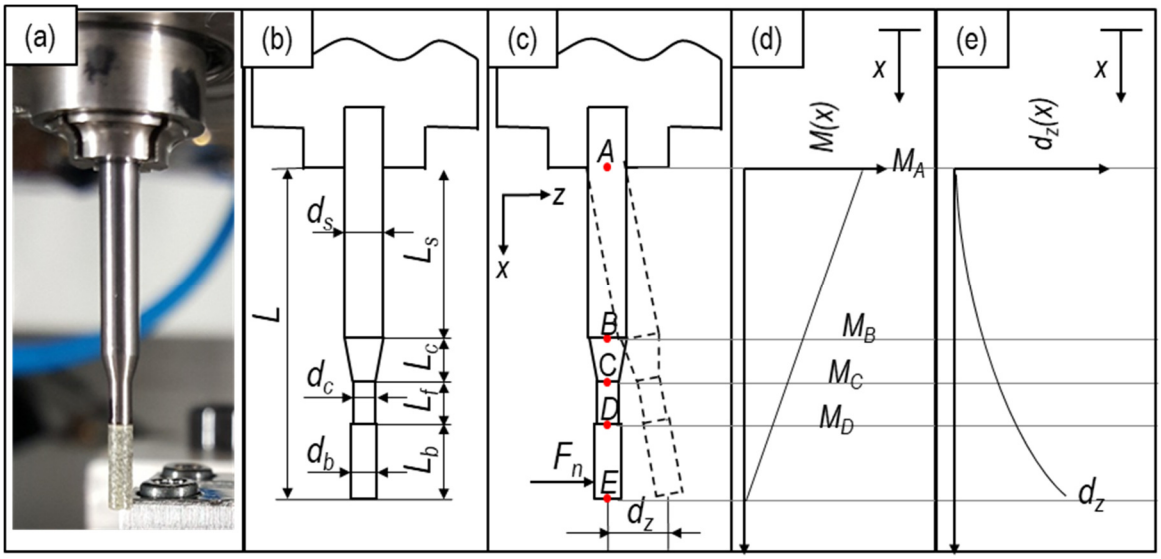

Fig. 15. Tool deflection model of micro-grinding tool a: micro-grinding tool; b: schematic of micro-grinding tool specification; c: schematic of micro-grinding tool deflection; d: bending moment diagram; and e: deflection diagram.

7. Summary of experimental results and discussion

This chapter presents a summary of the experimental work on two different materials. Firstly, the effects of process parameters on micro-grinding of Si_3N_4 outputs is discussed. Then, a method is proposed to achieve a highly efficient micro-grinding process. Afterward, the results of the simulations are presented and the material removal mechanism in micro-grinding of titanium is studied. Finally, the grindability of titanium is addressed. It should be noted that this summary focuses on selected results from the published papers and the manuscript under review.

7.1. Micro-grinding of ceramics

In this section, the results of micro-grinding of Si_3N_4 ceramic are presented and discussed.

7.1.1. The effect of tool specification

Fig. 16 shows the effect of the tool bond type on grinding forces and the roughness of the ground surface. The finest surface roughness was obtained by using electroplated micro-grinding tools. The electroplated tool has more abrasive grains per unit area compared to the other utilized grinding tools [28]. More grains generally lead to a higher dynamic cutting edges number, which in return reduces the uncut chip thickness. The higher the number of the active grains, the better the surface roughness. Additionally, the very high grit protrusion of the electroplated tool (which is the characteristic of this bond) leads to less rubbing and ploughing regimes – and consequently less plastic deformation in the workpiece, which may also influence the surface quality. Comparison between the metal and hybrid bonded tools reveals higher surface roughness for hybrid bonded grinding tool (Fig. 16). This is likely associated with the distribution of the grains on the tool surface. The hybrid bond material is a combination of vitrified and metal bond – using the advantages of both materials (good profile keeping and dress-ability). However, the grain distribution of the metal-bonded tool is much more uniform than the hybrid bond after dressing and sticking processes, causing lower surface roughness.

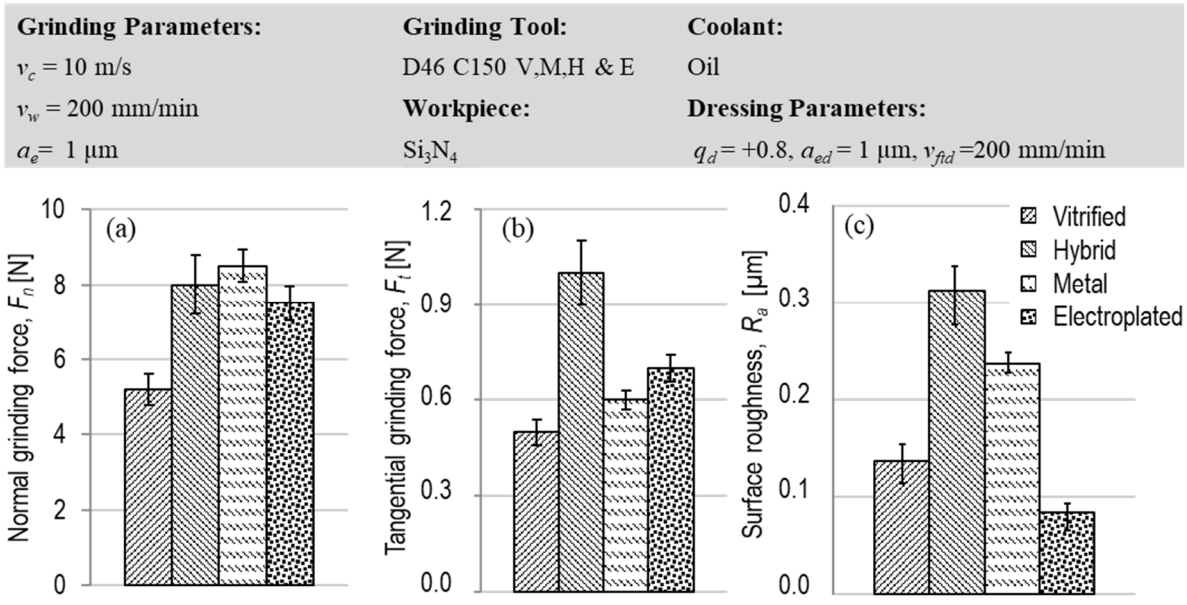

Fig. 16. Grinding forces, a: F_n; b: F_t; and c: surface roughness Ra, versus bond type of the grinding tool.

The vitrified grinding tool gave lowest normal and tangential forces as the result of high grain protrusion, high porosity, and better self-sharpening compared to the other bond types. Moreover, because of the hard and brittle nature of the vitrified bond, the dressing process induces sharper cutting edges of the vitrified bonded tools, easing the material removal. The comparison between the metal and hybrid bonded micro-grinding tools reveals that the metal bonded grinding tool generated lower tangential grinding force and slightly higher normal forces. The tangential grinding force is involved directly in material removal while the normal force is a result of the tool grains penetration into the workpiece. The micro-topography of the utilized metal bond tool is rougher than the micro-topography of the hybrid bond tool and the

diamond grains are sharper, which causes lower grinding forces and consequently lower tangential forces [28].

The bonding material of the tool is one of the most influential factors on the normal forces as well [101]. It could be assumed that the lower porosity and higher amount of the bond material, in the case of metal-bonded grinding tools, lead to higher normal forces, since the possibility that the bond comes into contact with the workpiece material is higher. Additionally, a large number of cutting edges over the grinding tool increases the normal forces more rapidly than tangential forces. Since the hybrid-bond grinding tool has more porosity than the metal-bond tool, the total penetration force of the grains into the workpiece material may be reduced, resulting in lower normal forces. The electroplated grinding tool is a single-layer grinding tool containing diamond grains electroplated over the surface of the grinding pin. Therefore, the grinding tool cannot be dressed. Since the retention force of the electroplated bond is very high, the grains can become dull during the process. Additionally, the dull grains could not be replaced by the sharper grains via self-sharpening (as there is only one layer of grains). However, the number of grains per unit area on the tool surface is much higher in the case of an electroplated tool compared to other bond types [28]. Hence, it can be assumed that the high number of cutting edges (including the dull ones) leads to relatively high normal grinding forces. On the other hand, the reduced uncut chip thickness (due to a higher number of cutting edges) and less friction (due to high grit protrusion) led to lower tangential grinding forces.

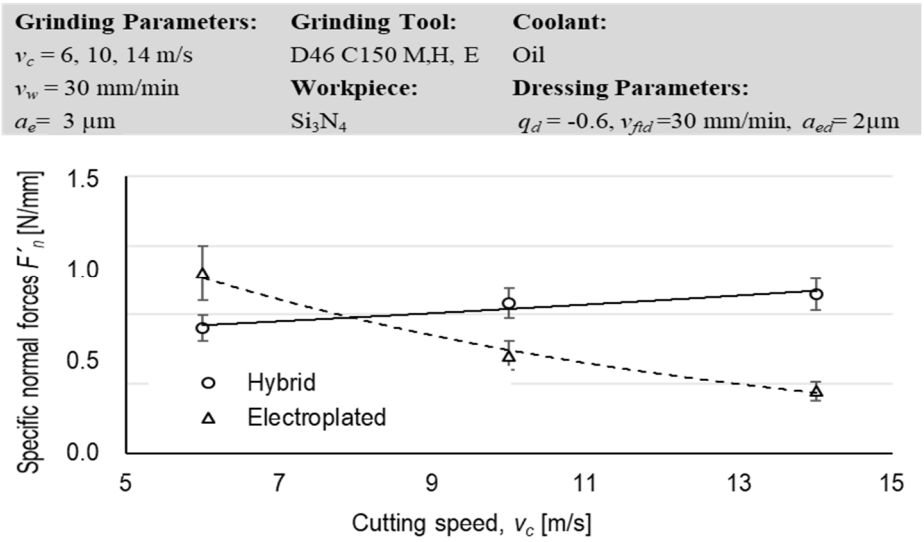

Fig. 17. The effect of cutting speed on the specific normal grinding forces.

To get a better understanding of the tool performance, the specific grinding forces of the hybrid bond and electroplated grinding tools were studied at different cutting speeds (v_c = 6, 10 and 14 m/s) – see Fig. 17. The specific grinding force in this study is considered the normal force divided by the removed depth of cut measured via a tactile measuring sensor in the machine tool. The actual depth of cut was measured at three points, at the beginning, in the middle and at the end of the grinding path. Each test was finished in three passes. Both tools demonstrated a different performance when increasing the cutting speed. The specific force remains almost constant in the case of the hybrid-bonded tool. However, the specific force was decreased by increasing the cutting speed for the electroplated grinding tool. Increasing the cutting speed reduces the chip thickness and generally causes lower grinding forces in micro-grinding [5].

To further investigate the grinding tool performance, a long-term test was done with fixed grinding parameters for all grinding pins. Here, a feed rate of 500 mm/min and a depth of cut of 5 µm was chosen to compare the results with Fig. 16. The results for tangential forces are given in Fig. 18. It can be observed that material removal rate also affects the performance of the grinding tools. The material removal rate was increased significantly (depth of cut and feed rate are 5 µm and 500 mm/min, meaning more than 12 times higher material removal rate) compared to Fig. 16 (where the depth of cut and feed rate is 1 µm and 200 mm/min, respectively). In this case, the vitrified tool generated the highest force at the beginning of the process. However, when increasing the volume of removed material (grinding passes), a significant force reduction was observed. This behavior may be attributed to the strength of the vitrified bond, which normally has a lower retention force than the other bond types, causing the self-sharpening of the grains during the grinding process [28].

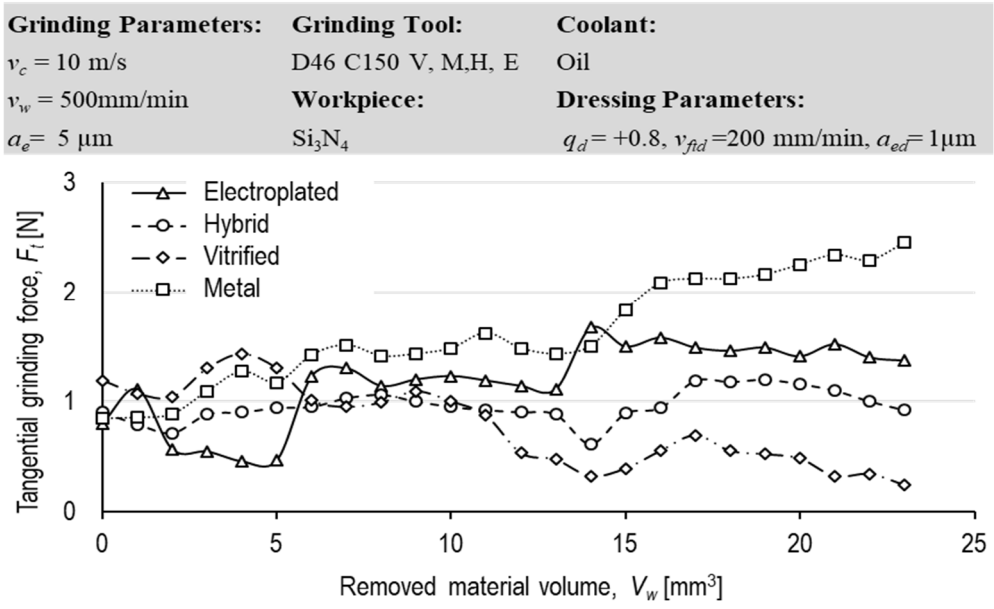

Fig. 18. Tangential grinding forces versus removed material volume.

Fig. 19 shows that the protrusion height of the metal-bonded tool was decreased significantly by removing more material from the workpiece. At the beginning of the long-term test, the grains were sharp and had a higher protrusion height. However, the topography of the tool became much smoother at a higher volume of the removed material as the result of tool wear.

During the long-term testing, the hybrid tool tended first to self-sharpen because of the portion of the vitrified bond which was mixed with the metal bond in this bond type. However, the grains became duller with time. The self-sharpening reduced the forces, but the tool wear increased them [28]. Increasing the volume of the removed material decreased the forces for the electroplated grinding tool. Further material removal first increased the forces sharply. However, the level of process forces stayed almost constant up to 13 mm^3 of removed material, where another jump in grinding forces occurred. Since the electroplated grinding tool is a single layer tool, the worn grains could not be replaced by the new sharp grains. The grains could either partly break, flatten, or be pulled out from the surface of the electroplated grinding pin. Grain breakage induces new sharp cutting edges and increases the number of cutting edges, resulting in lower grinding forces. Grain pull out results in lower active grains and higher chip thickness – increasing the grinding forces [28].

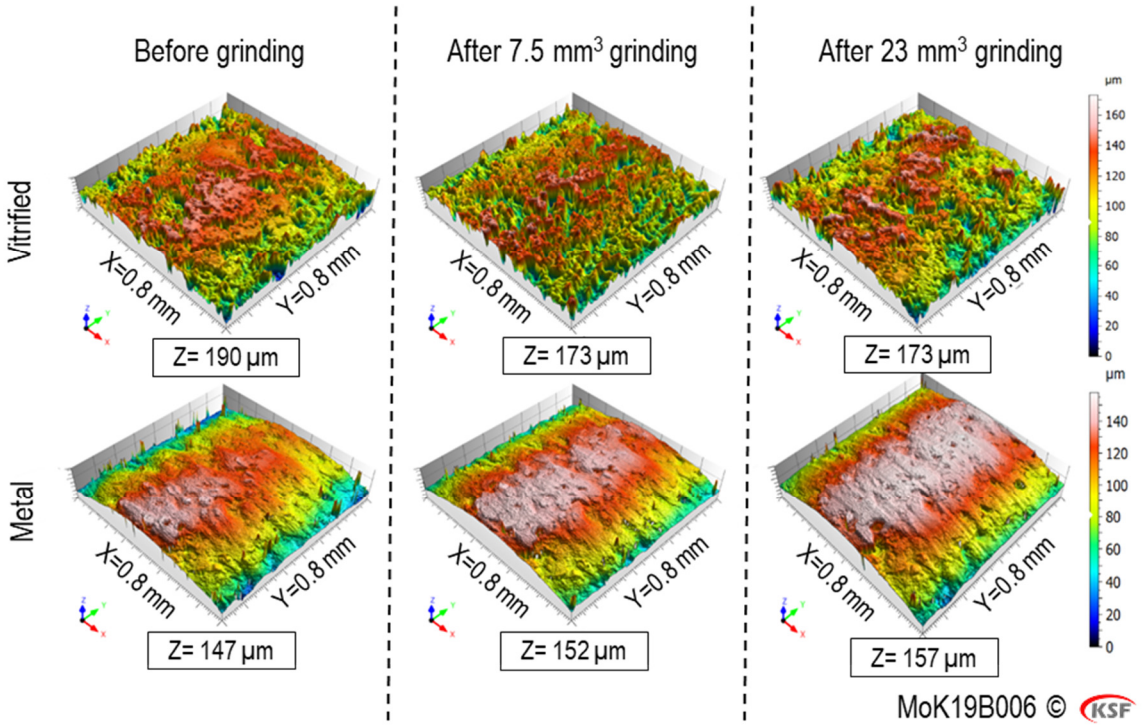

Fig. 19. The confocal pictures of the tools' topography after a certain removed material.

7.1.2. Laser-Assisted Micro-Grinding (LAMG)

As discussed in the previous section, the surface quality and grinding forces could be affected to some extent by changing the process parameters and topography of the tool. However, altering the process efficiency and surface quality via these parameters is not possible. Hence, to improve the process efficiency and accuracy of the finished part, the results of a hybrid process are described in this section. The effect of 10% tool structuring and 30% of workpiece structuring on the grinding forces and surface roughness is shown in Fig. 20.

It is demonstrated that as little as 10% of tool structuring led to a significant reduction of the specific energy. The specific energy was reduced up to 35% by reducing the process forces. During the grinding process, the abrasive grains penetrate the workpiece material with high velocity and remove the material at a high strain rate. In contrast to ductile materials such as titanium, crack propagation is the main material-removal mechanism during grinding of brittle ceramics. Grinding with the laser-structured tool may allow for more lateral crack propagation compared to non-structured tools and more micro-cracks in the workpiece-tool contact zone due to intermittent cutting, easing the chipping mechanism, and improving the material-removal process with lowering the grinding forces [91]. Furthermore, structuring the grinding tool reduces the number of static and dynamic cutting grits on the surface of the grinding tool. This means less ploughing and rubbing – and a higher share of cutting [102]. Additionally, the tool-workpiece contact length is smaller when employing structured tool compared to conventional micro-grinding. 10% tool structuring translates into lowering the tool-workpiece contact zone area up to 10%. The smaller the contact area, the lower the process forces and temperatures and more efficient the micro-grinding process. Another reason for specific energy reduction by LAMG is attributed to improved lubrication, due to the effect of the grooves on the tool. In this

case, the coolant can be easier transported through these grooves into the contact zone, whereby the cooling becomes more effective.

The workpiece structuring could also reduce the specific energy up to 15%. This is mainly due to reduced volume of the workpiece material (by laser structuring) which is to be removed by the subsequent micro-grinding process. Since the material is brittle, the laser structuring enhances the crack initiation and propagation around the laser-ablated structures [83,91]. This eases the micro-grinding process and reduces the specific energy. However, LAMG produced a rougher surface (about 40% higher) compared to the Conventional Micro-Grinding (CMG) [4,91].

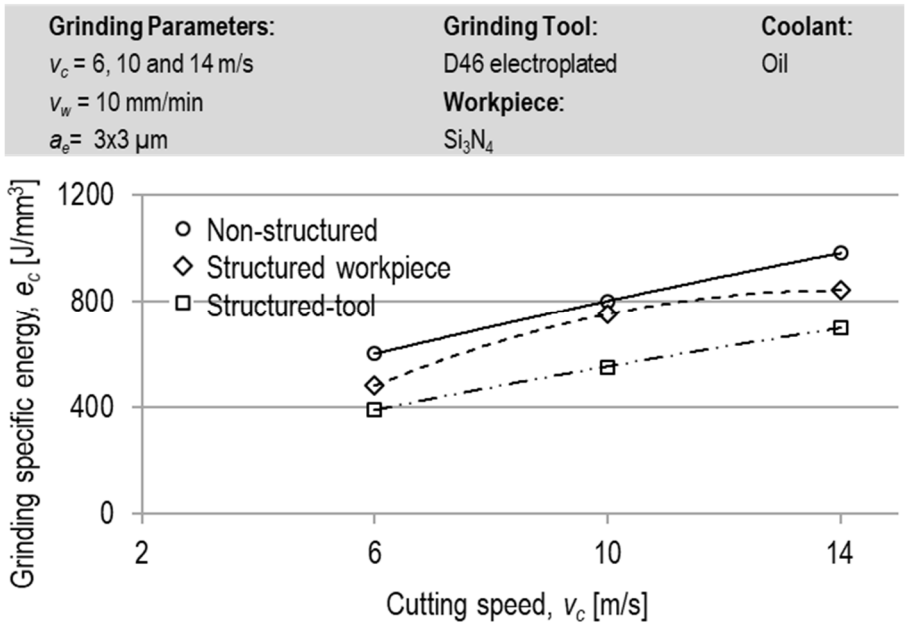

Fig. 20. The effect of structuring on a: the grinding forces and b: the surface roughness.

Overall, it can be stated that tool structuring was more effective than the workpiece structuring in the LAMG of Si_3N_4 – in terms of specific energy. Tool structuring results in a lower number of active grains compared to workpiece structuring. This leads to less rubbing and ploughing during the micro-grinding process compared to the workpiece structuring, as a result of higher chip thickness and more efficient process.

To investigate the effect of tool structuring on the performance of the grinding tool, long-term tests with the same grinding parameters for both structured and unstructured tools were carried out. The specific energy was periodically measured after a certain volume of material removal. Fig. 21 illustrates the results. Here, the specific energy for the non-structured grinding tool increased with more material being removed. The specific energy for the structured tool was much lower (around 85% in all cases) compared to non-structured tool at all volumes (V'_w). The specific energy for the non-structured tool increased with material removal to some specific rate of tool wear. Then, the forces dropped and increased (linearly) again. Big drops in the specific energy values are caused by diamond grains breakage during the machining process – resulting in new sharp cutting edges that reduce the specific energy.

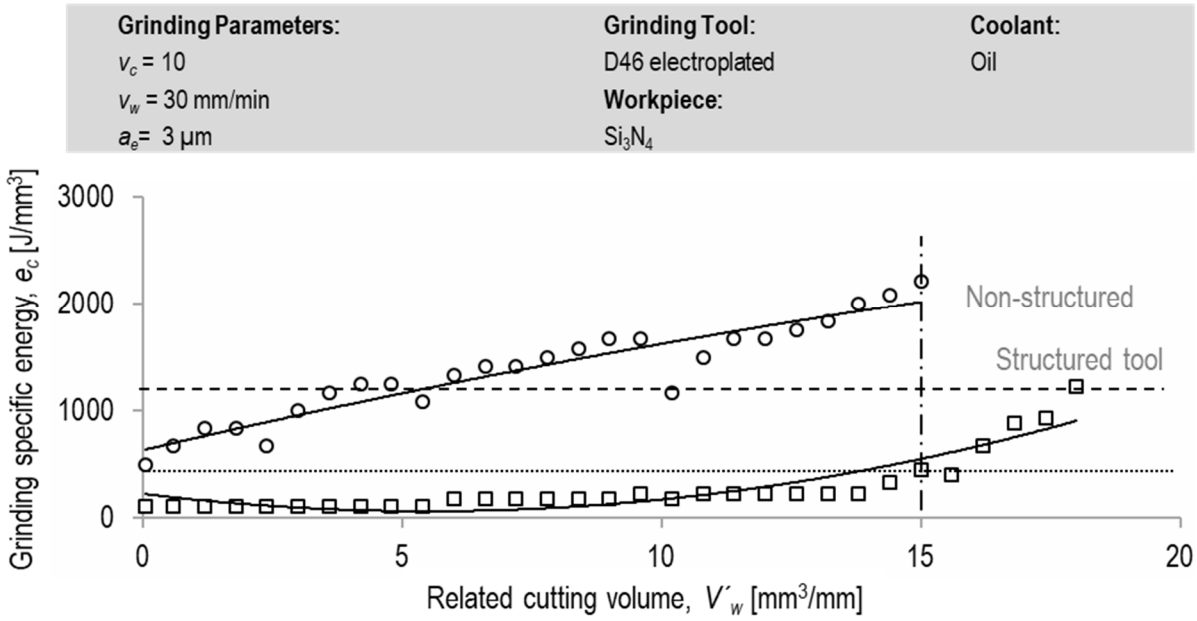

Fig. 21. The effect of structuring on the specific energy versus removed material.

In comparison to specific energy associated with the non-structured tool, the specific energy for the structured tool stayed almost constant up to 14 mm^3/mm material removal and then it increased continually – showing the better performance of the structured grinding tool [4]. The specific energy of the structured tool at 15 mm^3/mm V'_w (Fig. 21 with the dashed line) are much smaller than those of the non-structured tool at the beginning of the process. This shows very good performance of the structured tool. Just 10 percent tool structuring resulted in higher productivity.

One of the most important aspects of micro-grinding is the accuracy of the parts. In micro-grinding, the tools are much weaker than fixed abrasive tools (wheels) for conventional grinding. Thus, they can be easily deflected during the process. As a result, the actual material removal deviates from the nominal depth of cut, which directly influences the accuracy of the part. In addition, the tool deflection may lead to vibrations during the process, especially at high removal rates. Therefore, the effect of tool deflection on part accuracy was investigated. The tool deflection was measured via a digital nano-taster integrated into the machine tool center by measuring the actual depth of cut removed from the workpiece. Each grinding test was performed with a depth of cut of 3 µm. Fig. 22 shows the effect of the cutting speed and workpiece structuring on the tool deflection. Here, increasing the cutting speed did not affect the tool deflection. Using the LAMG process resulted in no tool deflection. The actual depth of cut in LAMG was hence the same as the set depth of cut. In contrast, the CMG process resulted in approximately 1 µm tool deflection at all cutting speeds – resulting in approximately 30% lower actual than the nominal depth of cut (i.e. 3 µm). The grinding forces in case of laser-assisted micro-grinding are much smaller than the micro-grinding process with a non-structured tool or workpiece (as a result of lower specific energy). The lower process forces result in lower pressure and dynamic loads on the micro-tool during the micro-grinding process, causing less tool deflection.

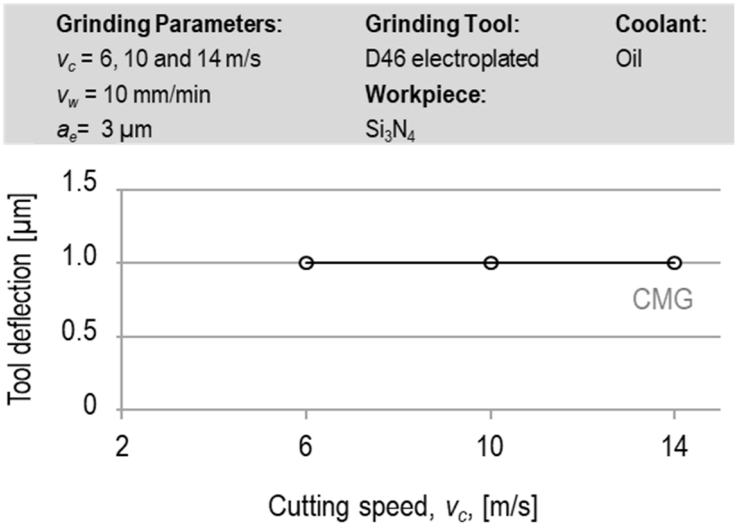

Fig. 22. The effect of structuring on the dimensional accuracy of the machined area.

7.2. Micro-grinding of titanium

In this section the results of micro-grinding of Ti6Al4V material are presented and discussed.

7.2.1. The effect of dressing parameters

The process outputs, like surface roughness and grinding forces, can be affected not only by tool specification but also by the grinding and dressing parameters. In micro-grinding, the diameter of the tool is very small (i.e. 2 mm); hence, relatively high rotational speeds of the grinding pin are generally needed. For instance, almost 100.000 RPM are needed for achieving a cutting speed of 10 m/s. Therefore, extremely high dressing feed rates are also required to achieve typical dressing overlap ratios, U_d, (2 to 8). As a result, much higher values of dressing overlap ratios, U_d, were used in this study and their effect on grinding performance was studied.

The dressing overlap ratio is calculated as:

$$U_d = \frac{\sqrt{(8 \cdot r_{pd} \cdot a_{ed})}}{f_{ad}} \qquad \text{Eq. 7-1}$$

where a_{ed} is the dressing depth of cut, r_{pd} is the tip radius of the dressing tool, and f_{ad} is the axial dressing feed ($f_{ad} = v_{fad}/n_s$; where n_s is the rotational speed of the grinding pin and v_{fad} is axial feed speed by dressing). Here, it is assumed that the width of cut equals the active width of the dressing tool [103]. According to Fig. 23, high dressing overlap ratios (achieved by reducing the dressing feed) increase the grinding forces. In Fig. 23 the corresponding dressing feed rates for overlap ratios are listed in Table 5 at the cutting speed of 10 m/s.

Table 5: Corresponding dressing feed rates

Overlap ratios	2000	1000	350	300	100	50
Corresponding dressing feed rates (mm/min)	45	90	270	305	910	1830

The micro-topography of the grinding tool is affected by changing the dressing overlap ratio (Eq. 7-2), which gives the relationship between the theoretical grinding tool surface roughness, R_{ts}, and the dressing overlap ratio [12].

$$R_{ts} = \frac{a_{ed}}{U_d^2}$$ Eq. 7-2

Here, the higher U_d values lead to a finer micro-topography of the grinding tool – resulting in an increased number of static and kinematic cutting edges and rising the amount of rubbing and ploughing in grinding, which explains the observed rise in the grinding forces. On the other hand, higher dressing overlap ratios reduce the proportion of the grit break-out by dressing [104]. This phenomenon can be explained with reduced dressing forces when increasing the dressing overlap ratio. High dressing forces (which occur at lower dressing overlap ratios), lead to an aggressive dressing of the grinding pin. Hence, the grain tips may be broadly fractured. In contrast, it has been shown that the grain tips are more flattened when the dressing feed rate is low (i.e. at high U_d values) [105]. Therefore, the surface of the grinding tool is rougher (and the grains become sharper) when using higher dressing feed rates; hence, the sharper the grains, the lower the grinding forces.

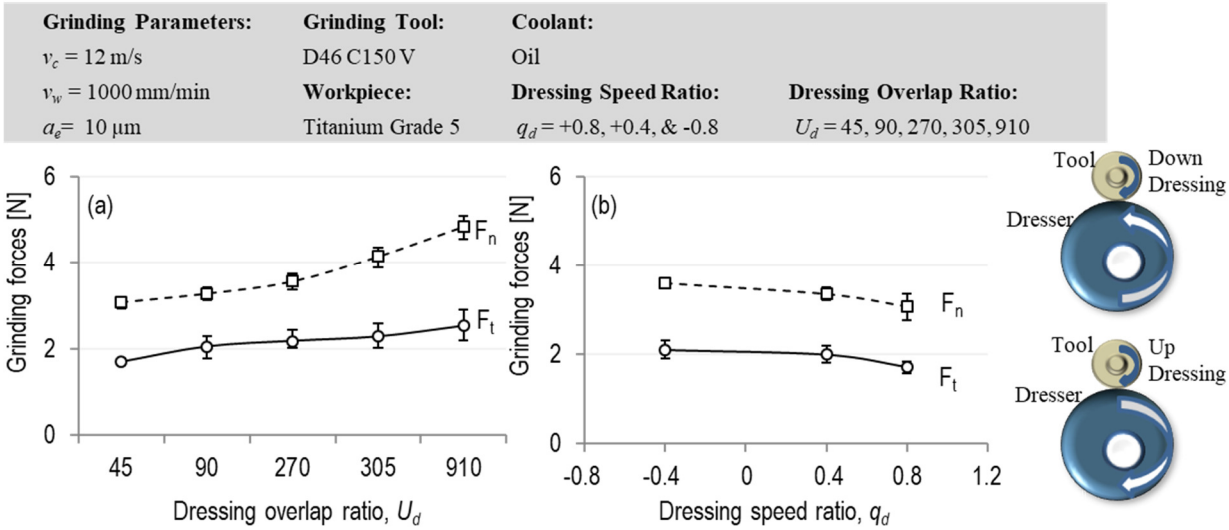

Fig. 23. The effect of a: dressing overlap ratio (q_d = +0.8); and b: dressing speed ratio (U_d = 45) on the grinding forces.

The effect of the dressing speed ratio is also shown in Fig. 23b. In rotary diamond dressing, the grinding tool and the dressing roller engage against each other in a rotational movement. The used speeds and the rotational direction determine the dressing-speed ratio, q_d, which has a significant effect on the dressing process. The dressing speed ratio is therefore another dressing parameter to consider when generating the micro-topography of the grinding tool. As such, q_d affects the dressing forces [106] and can be calculated as:

$$q_d = \pm \frac{v_{cd}}{v_c}$$ Eq. 7-3

where v_c is the grinding tool speed and v_{cd} is the dressing-roll speed. The rotary dressing can be categorized into two different processes, up-dressing ($q_d < 0$) and down-dressing ($q_d > 0$). In most operations, the common dressing speed ratios vary between -0.8 and +0.8.

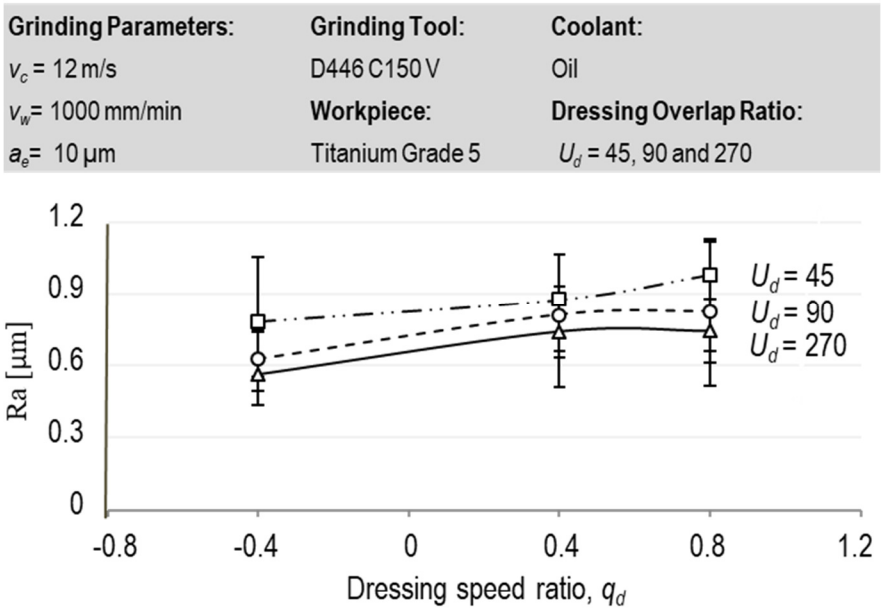

Fig. 24. Surface roughness, Ra, versus dressing speed ratio.

A rise in the speed ratio, q_d, (from -0.4 to +0.8) increases the dressing aggressiveness, leading to more grit breakage and/or break-out from the surface of the grinding tool. Moreover, the effective roughness of the grinding tool is higher when employing down-dressing, compared to the up-dressing [9,12,107], which decreases the grinding forces noticeably (Fig. 23b). In contrast, the contact length of the dresser-grinding tool is much larger in up-dressing compared to down-dressing. Moreover, the up-dressing, the generated paths on the grinding pin overlap with each other, causing more wear-flats and finer surface roughness of the grinding tool, which results in higher grinding forces, since the contact length is larger (i.e. the radius is bigger).

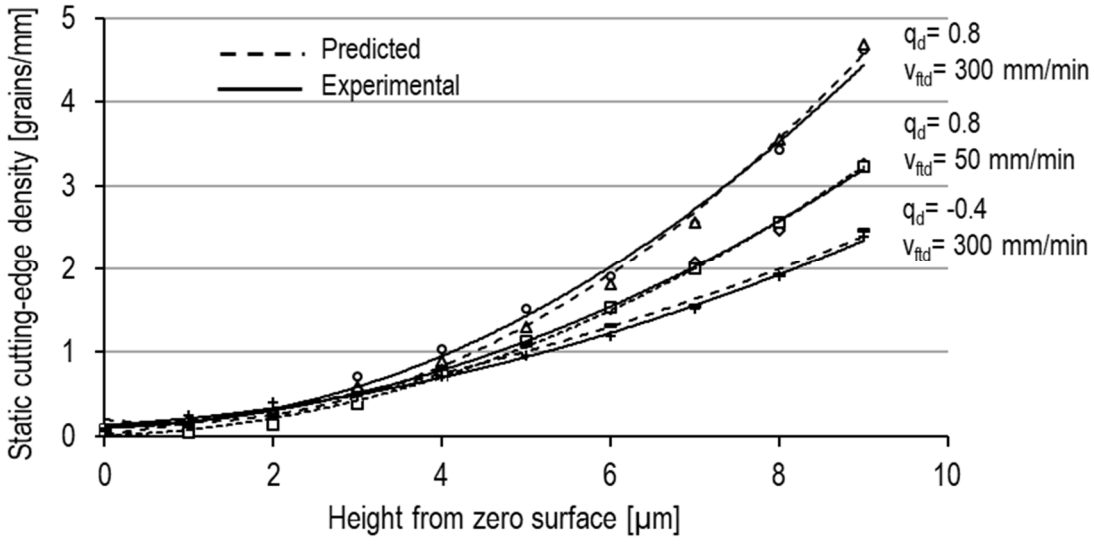

Fig. 25. Static cutting edge density versus the radial depth into the micro-grinding tool.

The relation between the surface roughness, the dressing speed ratio, and overlap ratio is shown in Fig. 24. Here it can be seen that the surface roughness increases when shifting from up-dressing to down-dressing because of higher theoretical roughness of the grinding tool.

Furthermore, the surface roughness improves by increasing the overlap ratio [5] due to a finer micro-topography of the grinding tool.

Up until now, it was clear that changing the dressing parameters could greatly influence the grinding outputs, i.e, grinding forces and surface roughness. But here the process parameters are kept constant and the tool topography is only changing with the dressing parameters. This implies that the chip thickness is varying at the same grinding parameters. Therefore, a modeling study for calculation of the chip thickness which considers the dressing parameters seems essential for better understanding of the process. To realize the effect of dressing parameters on the chip thickness, the dressing process was hence modeled. Fig. 25 shows both predicted and real static cutting-edge density at different radial depths into the micro-grinding tool (z). The predicted values are well in agreement with the experiments. The GPR model could also predict the static cutting-edges density with an average error of 10%.

As mentioned before, using different dressing parameters changes the micro-topography of the grinding tool and consequently the number of static grains (refer to Fig. 25). Parameters A and K (Eq. 6-6) for the estimation of the static grain density in a certain radial depth into the grinding tool are until now unknown. These two parameters change with different tool micro-topography as a result of varying dressing parameters. In the simulation model, the dressing parameters (like the grinding and material parameters) are given as inputs. By inputting the dressing parameters, the GPR model can predict the density of static grains in the radial depth into the tool. Here an exponential function (given in Eq. 6-6) was fit to the predicted grain densities and for each dressing parameter set; moreover, the parameters of A and K were experimentally determined and the grinding forces were predicted. The results in Fig. 26 show two different dressing parameter sets.

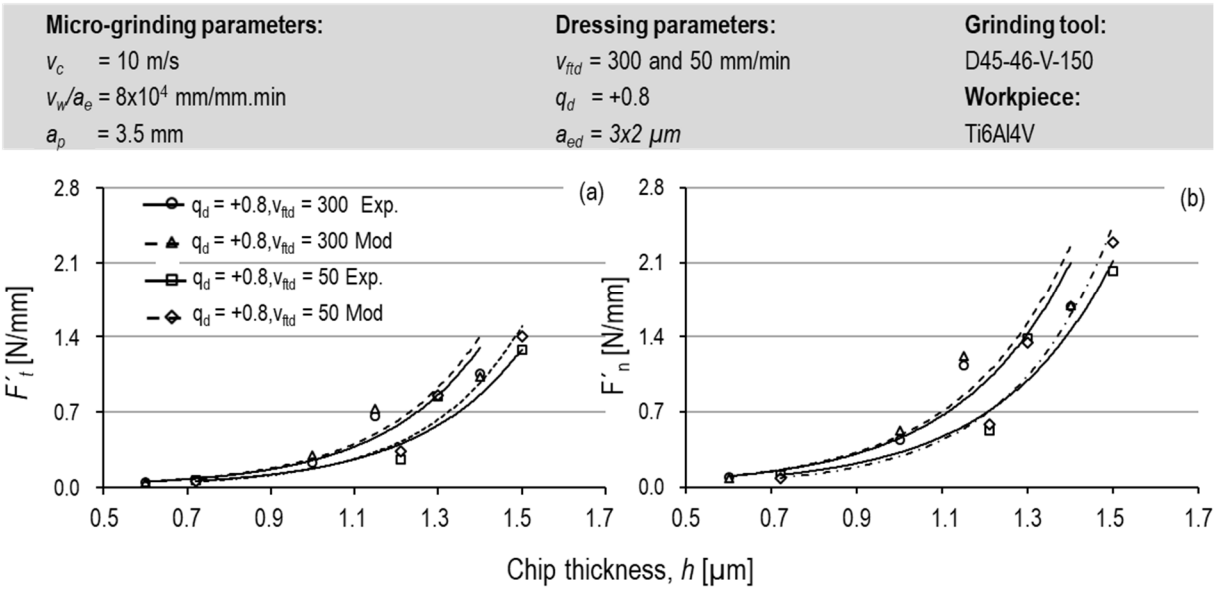

Fig. 26. The effect of dressing parameters on the specific grinding forces a: specific tangential micro-grinding forces; and b: specific normal micro-grinding forces.

For the dressing analysis, the dressing feed rate, v_{fad}, was used instead of the dressing overlap ratio, U_d. Based on the primary results from the dressing process (Fig. 23 and Fig. 24) lower dressing feed (higher dressing overlap ratio) resulted in higher grinding forces and better surface finish considering constant dressing parameters. The same effect was observed when

up-dressing instead of down-dressing (see Fig. 26). Using more timid dressing parameters generated a finer tool topography – resulting in higher specific grinding forces. Fig. 26 indicates that the prediction model can precisely map the effects of dressing parameters on the micro-topography of the micro-grinding tool to predict tangential (with 11 percent error) and normal (with 10 percent error) grinding forces. Both simulations and experiments proved that finer dressing results in approximately 19% higher grinding forces where the chip thickness is the same. Thus, changing the dressing parameters can also change the efficiency of the micro-grinding process where for a given chip thicknesses, lower specific forces were always achieved for a sharper tool.

7.2.2. The effect of cutting speed

Similarly to conventional grinding, the process forces can be reduced by increasing the cutting speed in the micro-grinding process as well. This is due to lower chip thickness at higher cutting speed (Eq. 7-4) [12].

$$h_m = 2L\left(\frac{v_w}{v_c}\right)\left(\frac{a_e}{d_e}\right)^{1/2} \qquad \text{Eq. 7-4}$$

where L is the distance between successive cutting points. The cutting speed variation can also change the share of friction and plastic deformation in the process. This is due to different strain rates at different cutting speeds and/or influence of the chip thickness and the associated size effect. In Fig. 27a, the results of the modeled and experimentally measured forces indicate that changing the cutting speed has minimal influence on the tangential grinding forces, whereas the normal grinding forces reduced slightly at the same chip thickness value.

Grinding Parameters:	**Dressing Parameters:**	**Grinding Tool:**	**Coolant:**
v_c = 6, 10, 14 m/s	q_d = +0.8	D45-46-V-C150	Oil
v_w/a_e = 8 x10^4 mm/mm.min	v_{ftd} = 300 mm/min	**Workpiece:**	
h = Vary µm	a_{ed} = 3x2 µm	Conventional Ti6Al4V	

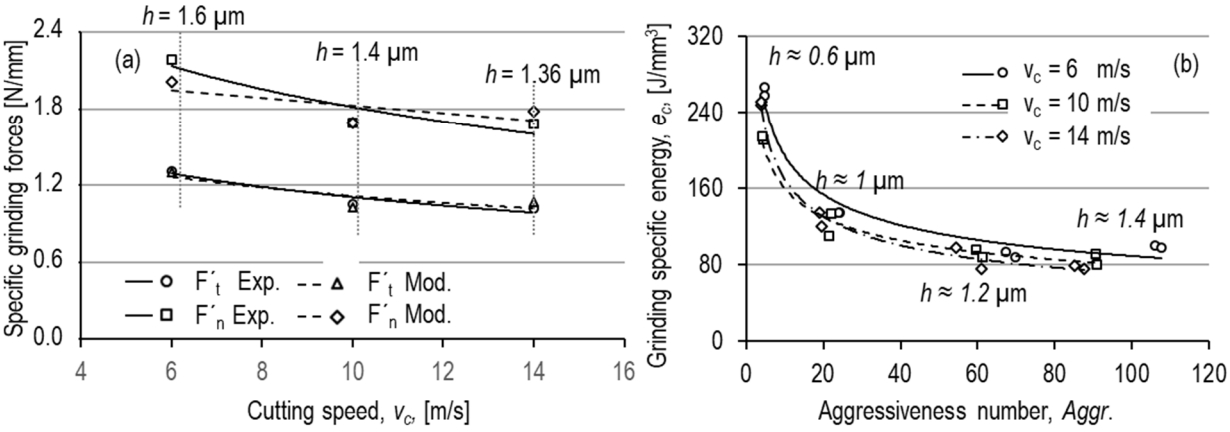

Fig. 27. The effect of cutting speed on a: specific grinding forces with average chip thickness of 1.5 µm (a_e ranging from 7.6-11.7 µm and v_w varying between 347-800 mm/min); and b: the grinding specific energy at different chip thicknesses (v_w/a_e = 8x10^4 mm/mm.min).

Since the diameter of the grinding tool in micro-grinding is small (i.e. 2 mm), and the rotational speed is limited, changing the cutting speed in a large increment is not possible. The results

imply that changing the cutting speed from 6 to 14 m/s has a minor effect on the flow stress of material in the micro-grinding process. However, the strain rate became almost doubled.

In Fig. 27, the chip thicknesses for cutting speeds 10 and 14 m/s are 1.4 and 1.36 µm respectively and 1.6 µm for the cutting speed of 6 m/s (Fig. 27a). At the cutting speed of 6 m/s, where the chip thickness is larger, higher tangential forces were observed (both modeled and experimentally obtained). Nevertheless, when changing the cutting speed from 10 to 14 m/s, where the chip thickness is similar, identical tangential grinding forces were generated. However, changing the cutting speed at the same chip thickness reduced the specific normal grinding force. This means that higher cutting speeds ease the penetration of the tool/grain into the material. Additionally, higher cutting speed in micro-grinding results in higher tool vibration [108]. This additional vibration in the process may also help the grain penetration into the workpiece, which is not considered in the models and which can explain the larger difference observed between the modeled and experimental normal forces at higher cutting speeds.

In this thesis, it is assumed that the cutting grains are idealized spheres, with an assigned average value for their size. However, in reality, each grain has its unique and random geometry and size. The real cutting grains are much sharper than the simulated ones. Therefore, they can penetrate the workpiece more efficiently – resulting in lower specific normal grinding forces. Moreover, the tool loading by chips is not considered in the models, which can have a significant influence on normal forces. It is worth mentioning that both parameters of friction coefficient μ and experimental factor d_f for calculating the single grain forces were obtained from the single grain tests – and their values change with varying chip thickness. The results of the single-grain test showed that the cutting speed in the tested range has no influence on μ and d_f. Based on the results, the model could accurately predict the tangential (with 9 percent error) and normal (8 percent error) micro-grinding forces with changing the cutting speed.

The topography of the grinding tool has random properties which make calculation of the chip thickness difficult. Therefore, the use of an alternative parameter to chip thickness can be useful to obtain a fundamental insight into the process, from the perspective of geometry and kinematics. Drazumeric et al. [109] introduced a novel, unifying modelling framework featuring the aggressiveness number, which can be directly related to the process outputs such the specific energy. In this study, the results of specific micro-grinding energy were compared under different conditions at the same grinding aggressiveness, calculated as:

$$Aggr. = 1{,}000{,}000 \frac{v_w}{v_c} \sqrt{\frac{a_e}{d_s}} \qquad \text{Eq. 7-5}$$

where d_s is the diameter of the micro-grinding tool.

Increasing the chip thickness resulted in lower specific energies (Fig. 27b). Higher chip thickness caused lower shares of friction and plastic deformation in the chip formation and consequently a more efficient grinding process. With an increase in the aggressiveness number, a minimum specific grinding energy of 79 J/mm^3 was achieved. Interestingly, varying the cutting speed did not affect the values of specific micro-grinding energy. Generally in the material removal processes, the cutting speed variation can change the share of friction and plastic deformation in the process [110,111]. This is due to different strain rates at different cutting speeds and/or influence of the chip thickness which can be perceived using the specific energy values. According to the same values of specific micro-grinding energy, the cutting speeds used in this study can be counted as low cutting speed and the flow stress follows the theory of the strain gradient plasticity [112].

In the grinding process, the induced residual stress arises as a result of the thermo-mechanical effects during the material removal process. They can be related either to thermal or mechanical loads [12,113]. Thermal loads, such as the thermo-plastic deformation at elevated temperatures, lead to tensile residual stresses – in this case, due to limited material expansion as a result of high temperatures occurring in a very short time period and the rapid cooling in the contact zone. Mechanical loads, like the mechanical and plastic deformation loads on the ground surface, cause compressive residual stresses [88,114–116].

Fig. 28 shows the results of residual stress measurement using the XRD technique. Compressive residual stresses were observed in all test specimens. In the micro-grinding process, the grinding temperature is low compared to conventional grinding. Therefore, residual stresses are likely the result of the mechanical load during the grinding process. Increasing the cutting speed from 6 m/s to 10 m/s resulted in lower compressive residual stresses. And increasing the cutting speed from 10 m/s to 14 m/s did not change the residual stresses significantly. The error bars show the repeatability of the test; here each test was replicated 2 times.

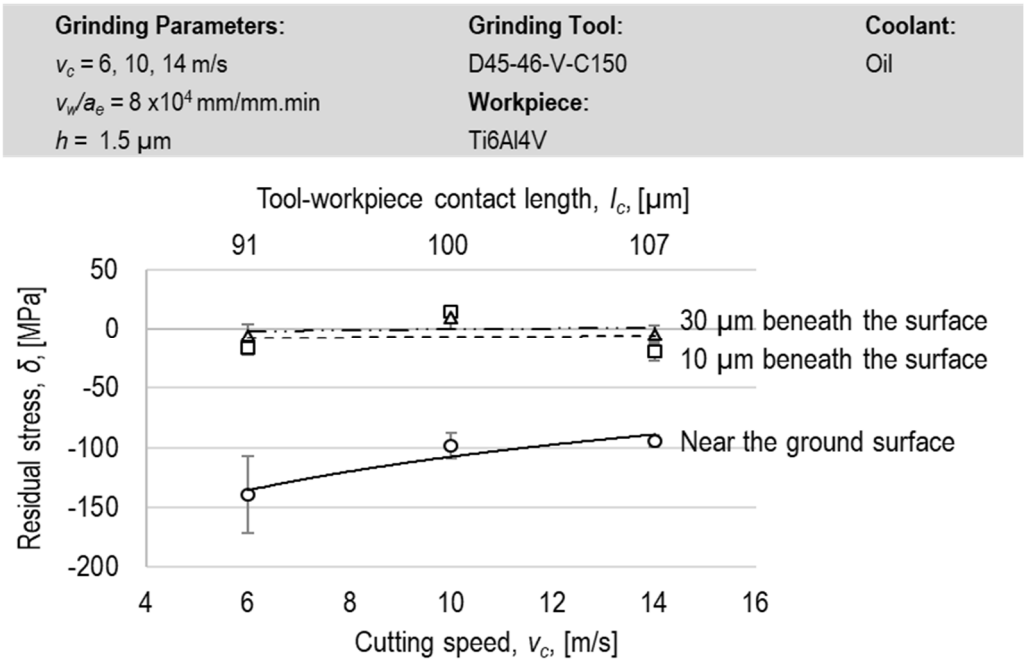

Fig. 28. The residual stress at constant chip thickness versus the cutting speed (v_w/a_e = 8x10^4 mm/mm·min).

To have a better understanding of the process, the topography of the ground surface was assessed with help of the SEM images shown in Fig. 29. They show the effect of cutting speed at almost the same aggressiveness number, 21 (chip thickness around 1.4 µm) and v_w/a_e ratio of 8x10^4 mm/mm.min. To achieve almost the same aggressiveness at different cutting speeds, the feed rate and the depth of cut were increased in order to keep the v_w/a_e ratio constant. For example, at the cutting speed of 10 m/s, a v_w of 300 mm/min and an a_e of 3.8 µm resulted in *Aggr*. of 21. To have almost the same *Aggr*. of 19.5 at the cutting speed of 14 m/s, a v_w of 355 mm/min and an a_e of 4.4 µm were used.

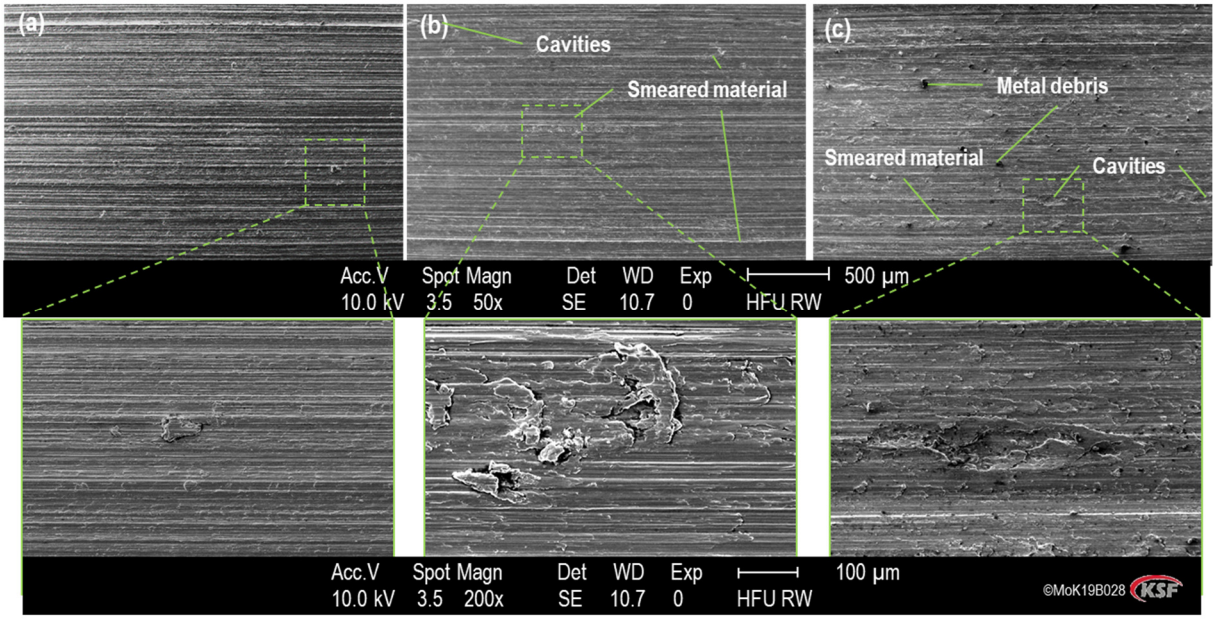

Fig. 29. Topography of the ground surface at a: v_c = 6 m/s; b: v_c = 10 m/s; and c: v_c = 14 m/s (v_w/a_e = 8x10^4 mm/mm.min and $h \approx$ 1.4 µm- *Aggr.* ≈ 21).

A better surface quality with fewer surface defects was achieved at a cutting speed of 6 m/s (Fig. 29a). Increasing the cutting speed deteriorated the quality of the workpiece surface, where the chip thickness is almost the same. Higher cutting speeds led to smeared material and cavities on the ground surface as a result of higher plastic deformation and possibly higher grinding temperature (Fig. 29b), despite almost the same chip thickness. More smeared material, larger cavities and some material debris can be seen when the cutting speed is 14 m/s Fig. 29c – meaning high plastic deformation and higher temperatures as compared to the cutting speeds of 6 m/s and 10 m/s (Fig. 29a and b). Therefore, at higher cutting speeds, high plastic deformation and higher temperatures are generated, resulting in material softening. However, it is important to note that the values of specific energy are identical for all cutting speeds. These results suggest that both material softening and strain hardening play a role in the material removal mechanism at the given cutting speeds.

7.2.3. The effect of feed-rate-to-depth-of-cut ratio

The previous section demonstrated that the cutting speed has a minor influence on grinding forces when the chip thickness was kept constant. Nevertheless, it is also necessary to examine the effect of another two important grinding parameters, i.e. the depth of cut and the feed rate. To investigate the impact of both parameters in the abrasive process, a feed-rate-to-depth-of-cut ratio, v_w/a_e, is employed. The ratio v_w/a_e is a valuable process-control parameter since the effect of both feed rate and depth of cut on the process outputs can be examined at the same time.

The effect of v_w/a_e ratio on the specific micro-grinding forces is shown in Fig. 30a. The figure shows that there is no considerable change in the grinding forces with changing the v_w/a_e ratio. This means that neither a higher depth of cut nor a larger feed rate has an influence on the grinding forces. It is important to mention here that in all figures, the actual depth of cut is considered. The model could accurately predict the tangential (with 12% error) and normal (13% error) grinding forces by changing the feed-rate-to-depth-of-cut ratio. Almost the same

specific energy was generated for all v_w/a_e ratios, as long as the chip thickness was kept constant (Fig. 30b). Increasing the v_w/a_e ratio slightly increased the value of the chip thickness (Fig. 30a).

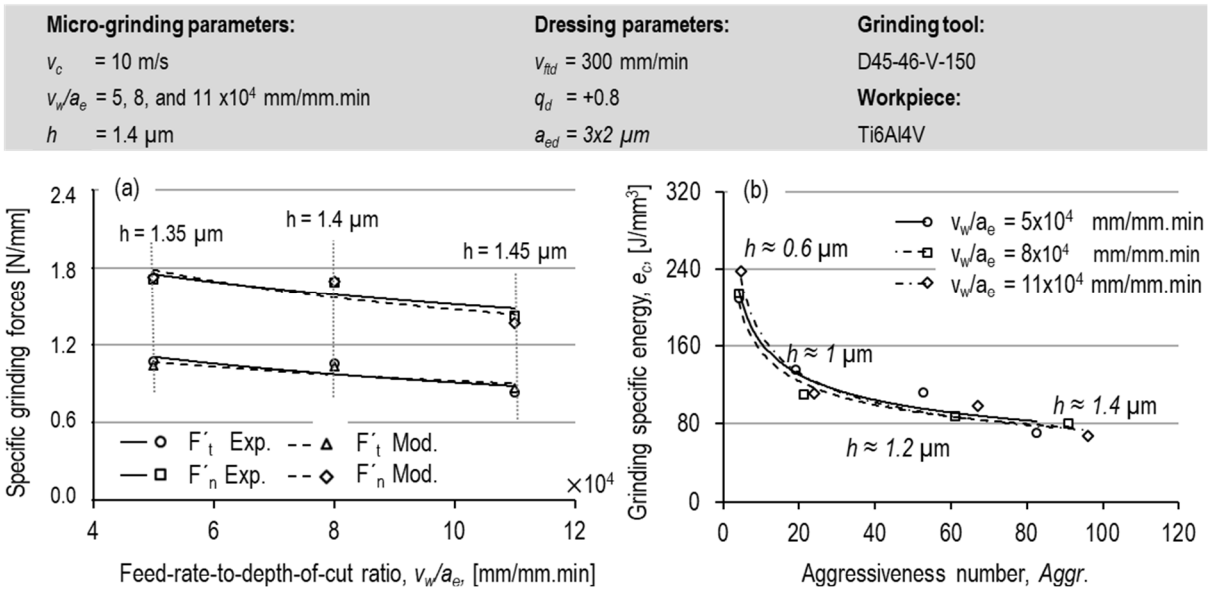

Fig. 30. The effect of v_w/a_e on a: specific grinding forces with average chip thickness of 1.4 µm ($a_{e\text{-}real}$ ranging from 8.1-13 µm and v_w varying between 633-940 mm/min); and b: the grinding specific energy at different chip thicknesses (v_c = 10 m/s).

The residual stresses for different v_w/a_e ratios were also measured and the results are shown in Fig. 31. Like in Fig. 28, compressive residual stresses were observed in all test specimens. Using a higher feed rate and lower depth of cut (higher v_w/a_e ratio) resulted in more compressive residual stress. The measured residual stresses in Fig. 28 and Fig. 31 indicate that they were generated only near the ground surface, but beneath the surface the effects of neither thermal nor mechanical stresses were seen and a maximum compressive stress of around 150 MPa was measured.

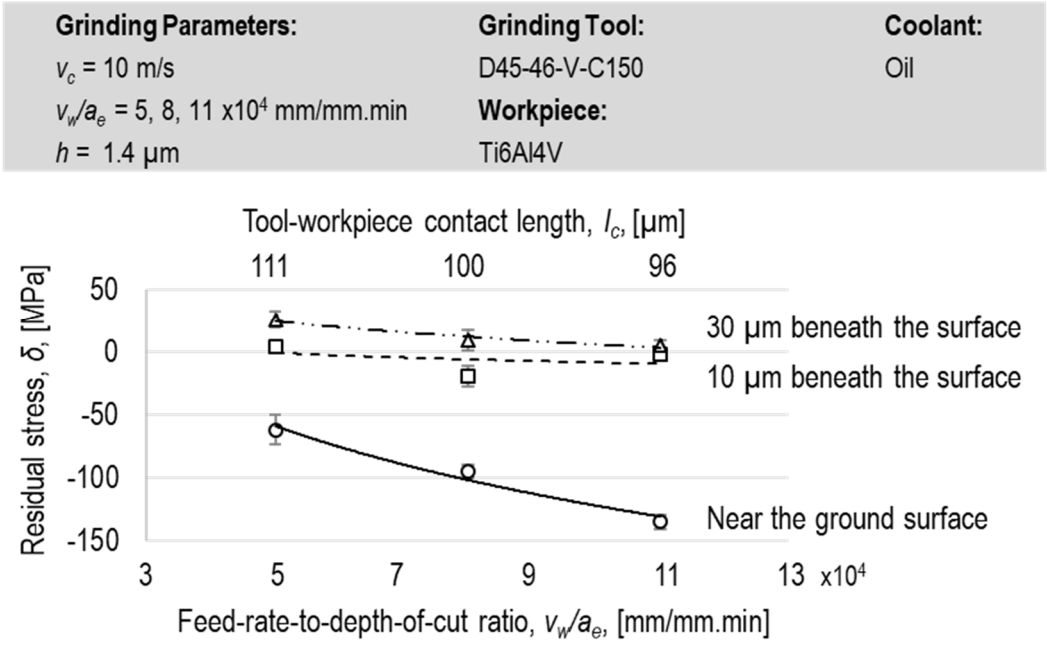

Fig. 31. The residual stress at constant chip thickness versus the feed rate to depth of cut ratio (v_c = 10 m/s).

For a better understanding of the effect of the v_w/a_e ratio, the topography of the finished surface was analyzed using SEM. The results are presented in Fig. 32. More smeared material was observed on the ground surface at lower v_w/a_e ratios, i.e. a lower surface quality is achieved during the micro-grinding process when using a lower feed rate and a higher depth of cut. Higher depth of cut and lower feed rates increased the tool-workpiece contact length (Fig. 31), resulting in higher temperature in process. Hence, for increasing the material removal rate, it is recommended to use higher feed rates instead of higher depths of cut.

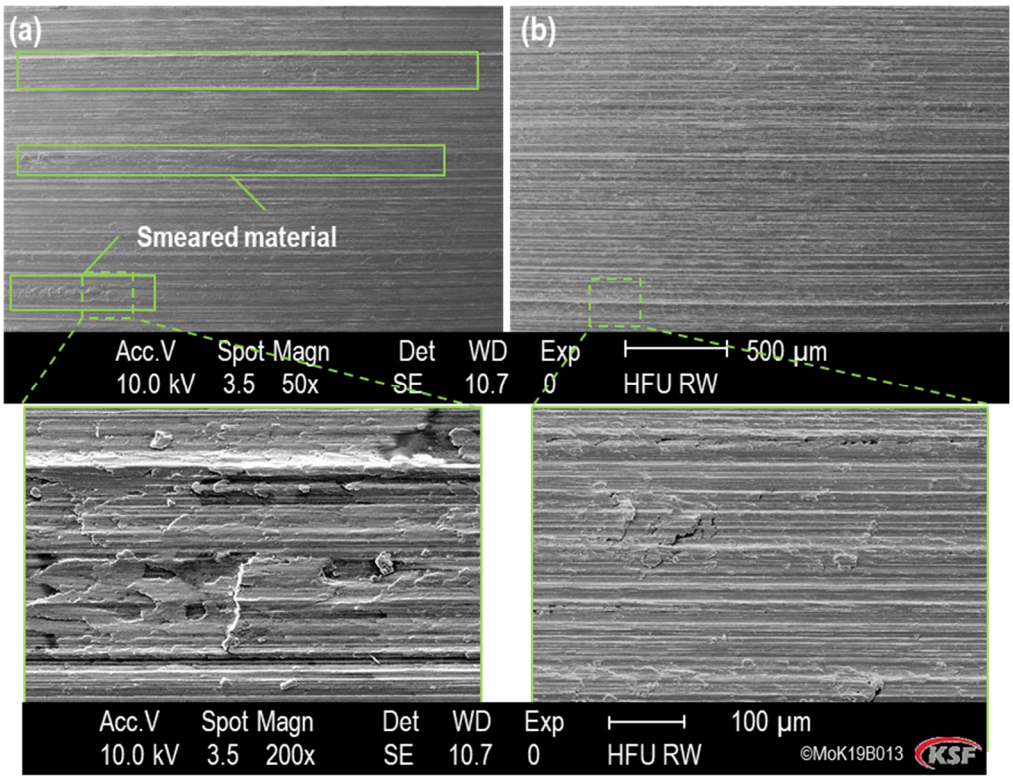

Fig. 32. SEM pictures from the ground surface a: $v_w/a_e = 5\text{x}10^4$ mm/mm.min; and b: $v_w/a_e = 11\text{x}10^4$ mm/min.min ($v_c = 10$ m/s and $h \approx 1.4$-*Aggr.* ≈ 21).

Fig. 27-32 suggest that the grinding specific energy can be connected to the surface integrity. Comparing Fig. 27b and Fig. 28 shows that where the specific grinding energy is higher ($v_c = 6$ m/s), more compressive residual stress was induced. This is due to the higher mechanical loads (grinding forces) on the surface at $v_c = 6$ m/s compared to the higher cutting speeds. The residual stress values shown in Fig. 28 correspond to the chip thickness of about 1.4 µm in Fig. 27b. In order to keep the chip thickness constant, depth of cut and feed rate varied at different cutting speeds, resulting in a change in the tool-workpiece contact length (l_c). Hence, according to Fig. 28, raising the cutting speed from 6 to 10 m/s leads to a 10% increase in the contact length (l_c). The specific energy and consequently mechanical load on the ground surface at $v_c = 6$ m/s (at $h = 1.4$ µm) is about 15% higher than that at $v_c = 10$ m/s. On the other hand, this increased force is distributed on the 10% smaller contact zone, as a result of which about 35% more compressive residual stress on the ground surface was generated. The same effect, but with a slighter trend, can be seen in Fig. 27b by increasing the cutting speed from 10 to 14 m/s (almost the same specific energy, 7% larger l_c).

At higher cutting speed and at an almost constant chip thickness, the number of tool rotations during the grinding path increases (cutting speed 14 m/s 2.3 times higher than cutting speed

6 m/s). Due to the higher rotation number and higher friction, the surface temperature can elevate. As a result, the surface quality became worse with increasing the cutting speed (Fig. 29; more debris and smeared material at higher cutting speeds). The elevated surface temperature with an increase in cutting speed can principally induce tensile residual stresses if the order is big enough. Recognizing the contribution of thermal and compressive stresses on the values measured in Fig. 28 needs further fundamental investigation.

Comparing Fig. 30b and Fig. 31 shows that the specific grinding energy is in the same order by varying the v_w/a_e ratio (at each constant chip thickness); the residual stresses changed with changing the v_w/a_e ratio. The almost constant grinding specific energies at various cutting speeds and the v_w/a_e ratios (at nearly same chip thicknesses) express that the tangential grinding forces are in the same order. Increasing the v_w/a_e ratio leads to a lower contact time between the tool and the workpiece (due to a smaller contact length) (Fig. 31) and due to higher feed speeds, leading to a smaller heat partition into the workpiece. Thus, higher compressive residual stress was induced in $v_w/a_e = 11\text{x}10^4$ compared with $8\text{x}10^4$ and $5\text{x}10^4$ mm/mm·min.

7.2.4. The effect of material microstructure

This section is dealing with the effect of material-manufacturing methods, i.e. additive manufacturing and conventional manufacture methods on grindability. The single grain test was first carried out to experimentally determine the minimum specific energy required for cutting of titanium alloy and to fundamentally explain the results of a micro-grinding process. Moreover, the specific grinding energies for all materials are calculated and the dependency of the process efficiency on the manufacturing process is discussed.

Single-grain scratching results

The evaluation of single-grain scratching and the explanation of the changes in specific cutting energy as an evaluation of the process efficiency requires the measurement of the ratio of the volume of material removed to the volume of material piled-up. For this, the chipping ratio f_{ab} is used:

$$f_{ab} = \frac{V_s - V_p}{V_s} \qquad \text{Eq. 7-6}$$

where V_s and V_p are the volumes of the removed material (groove) and pile-up, respectively. The maximum value for the chipping ratio f_{ab}=1 indicates no material pile-up in the absence of plastic deformation, i.e., ideal cutting. When f_{ab}=0, no cutting occurs, and plastic deformation is the only mechanism leading to the piling-up of material. The efficiency of the chip formation process can be measured by the specific energy dissipated for scratching. Using the volume of removed material and tangential forces, the specific cutting energy for the single grain test can be calculated using the following equation:

$$u_c = \frac{v_c \cdot \int F_t dt}{V_s} \qquad \text{Eq. 7-7}$$

where v_c indicates the cutting speed and F_t is the tangential force.

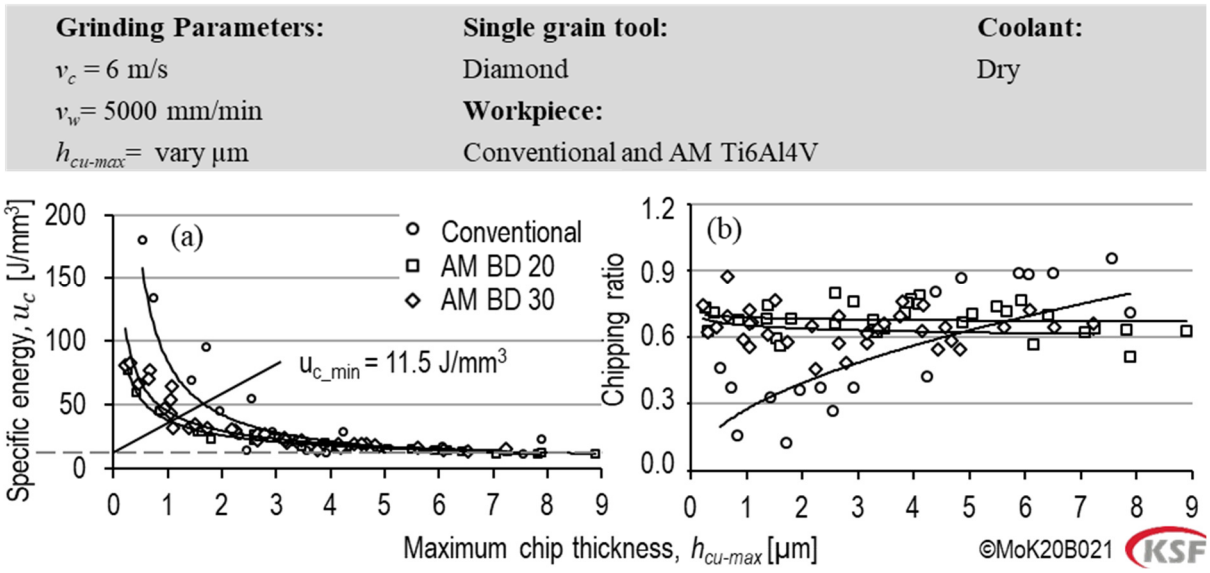

Fig. 33. The effect of the manufacturing process and chip thickness on a: the specific scratch energy; and b: chipping ratio.

Fig. 33 shows the results of the specific cutting energy and chipping ratio for the conventional and AM-produced titanium. As expected, the required specific energy for material removal was reduced by increasing the chip thickness for all materials. The minimum specific cutting energy of ~ 11.5 J/mm^3 was achieved for the titanium alloy regardless of the material-manufacturing method. The consumed energy for plastic deformation in the form of side plowing is larger than the energy required for the chip formation [12]. As illustrated in Fig. 33b, the values of the chipping ratio vary with chip thickness. The chipping ratio increases with the chip thickness, leading to a more efficient chip formation and lower specific energy (as shown in Fig. 33a). The obtained chipping ratio for conventional parts is lower than those for the AM parts at chip thicknesses less than 5 µm. This is because of the different microstructures. Almost the same result for the chipping ratio was observed for both AM parts. As a result, the cutting of AM material is more efficient at lower chip thicknesses because of lower plastic and elastic deformation during the process. When scratching conventional material, the lower chipping ratio at low chip thicknesses resulted in a higher specific energy, where the share of plastic and elastic deformation is considerably larger compared to the share of cutting. For both additively-manufactured materials (AM BD 20 and AM BD 30), nearly the same specific energies were observed due to similar chipping ratio and hardness. In many cases, the AM-parts need to be fine-finished. Examples of fine finishing of AM materials include super-finishing and fine grinding, which are performed at low chip thicknesses [35]. However, when larger chip thicknesses (larger than 5 µm) are used, the chipping ratio for the conventional part is slightly higher than for AM parts. This may be caused by the different material microstructures. Interestingly, chip thicknesses higher than 5 µm resulted in higher chipping ratios for the conventional parts compared to the AM parts, where almost the same specific energies for all kinds of materials were achieved. A higher chipping ratio generally means a more efficient process and lower specific energies. But at this point (chip thickness of 5 µm), the specific energy for all materials achieves its minimum value, which needs further investigation.

Micro-grinding test

Fig. 34 shows specific-energy measurements for three different Ti6Al4V materials (conventional, AM BD 20, and AM BD 30) and two different micro-grinding tool

concentrations (150C in (Fig. 34a) and 200 (Fig. 34b)). Increasing the grinding aggressiveness resulted in lower specific energies, which were also observed in the single-grain scratch tests by increasing the chip thickness. Higher aggressiveness values cause less rubbing and less plastic deformation in chip formation – and consequently a more efficient grinding process. With an increase in the aggressiveness number, a minimum specific grinding energy of 79 J/mm^3 was achieved, which is much higher than the minimum specific energy in the single-grain scratch tests (11.5 J/mm^3). This is because of the size effect in the micro-grinding process. Achieving the minimum specific grinding energy is only possible with aggressive process conditions that minimize plowing and rubbing. In the micro-grinding process, which features a small tool diameter and high tool deflection, obtaining high aggressiveness values is not feasible due to limitations in the achievable depth of cuts and feed rates.

In contrast to the single-grain scratch tests, where the AM materials generated lower specific energies compared to conventional titanium, the specific grinding energy in AM parts was either equal (for titanium build parallel to the workpiece width of 20 mm) or higher (for titanium build parallel to the workpiece length of 30 mm, and only for small aggressiveness numbers) in micro-grinding. At higher aggressiveness values, almost the same values of specific micro-grinding energy were obtained for all samples. The same can be observed for the 200-concentration tool (Fig. 34b). To check the validity of the results for non-aggressive grinding conditions (i.e. low aggressiveness), additional tests were done. The results are presented in Fig. 34c. The results confirm that at low aggressiveness values, the highest specific energy in the micro-grinding process was generated in the case of AM BD 30.

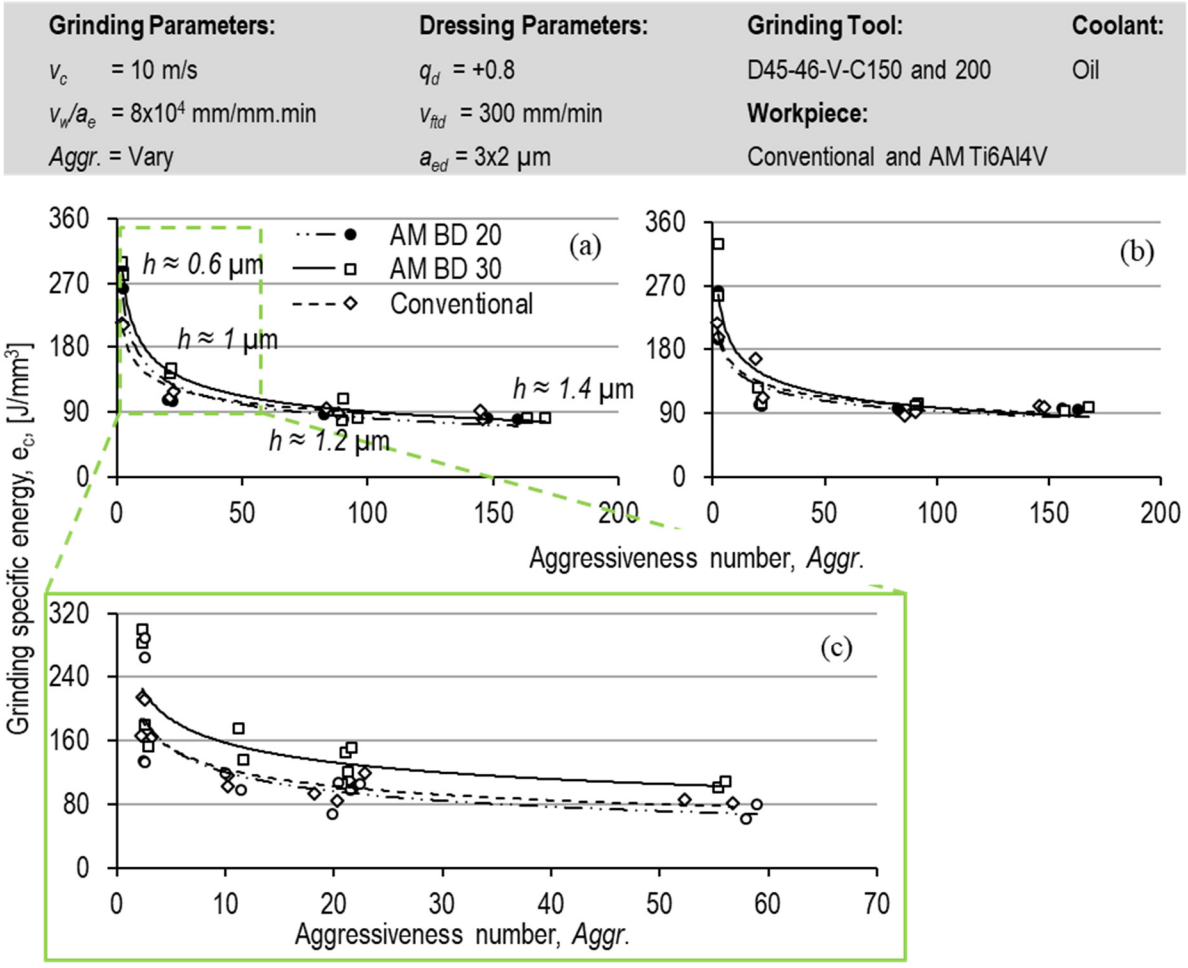

Fig. 34. The effect of the manufacturing process on the specific energy for a: tool with a concentration of 150; b: tool with a concentration of 200; and c: tool with a concentration of 150 in detail.

The differences between the specific energies in the single grain scratch test and in micro-grinding can be explained by the chipping ratio in the single-grain scratch test. Contrary to micro-milling, the chip thickness in the micro-grinding process is normally very low (typically lower than 2 µm). Therefore, to examine the material-removal mechanism, small chip thicknesses in the single grain scratch test must be considered. According to the results in Fig. 33, at chip thicknesses lower than 5 µm the AM parts produced lower pile-up material compared to the conventional part – independent of the build direction. In this range, the specific energies of AM parts are also lower because of the lower share of plastic deformation in the single-grain scratch tests. In the single-grain scratch tests, only a single abrasive grain participates in the material removal process in a single cutting path. In the micro-grinding process, however, the micro-grinding tool consists of several abrasive grains (for example 20 static abrasive grains in 10 µm depth of the tool) which are stochastically distributed over the surface of the micro-grinding tool. Hence, several abrasive grains are contributing to the material removal process simultaneously.

As with the single-grain scratch test, a slot remains after each grain-workpiece engagement. The 3D space includes a groove and material pile-up left along the cutting path. The subsequent abrasive grain then engages with the work material. The new grain, depending on its protrusion height and position with respect to the first grain, either cuts another slot along its moving path or moves between the slots cut by the former grains. If the grain comes into contact with the workpiece, it will not only cut the workpiece surface but also remove the pile-up material remaining from the previous pass. The higher the volume of piled-up material, the higher the volume of material removed by successive grains. This results in a larger instantaneous chip thickness for each abrasive grain under the same process conditions.

Varying the chip thickness changes the share of the rubbing, plowing, and cutting in chip formation. Since the chipping ratios for the conventional part are smaller than the chipping ratios for the AM parts (at chip thicknesses values lower than 5 µm, in Fig. 33b), each single abrasive grain removes relatively more material (i.e., there is more pile-up material at the same chip thicknesses), which means a higher share of cutting and a lower share of plastic and elastic deformation. The micro-grinding of conventional parts benefits in this respect. However, it could result in a higher share of plastic deformation in the micro-grinding of AM parts. Therefore, the specific micro-grinding energies are almost of the same order as the conventional parts. Another reason may be associated with strain hardening. Dmitriev et al. [117] studied the effect of material crystallographic orientation on strain hardening of pure titanium in scratch tests. They showed that, depending on the crystallographic orientation, the strain hardening after scratching can happen either on the base material or the pile-up. It was also reported that when the indenter (here in micro-grinding the abrasive grains) moves along the easy-slide directions (the easy-to-cut crystallographic orientations), the strain hardening happens in the base material rather than in the pile-up. Moreover, when the indenter movement differs from easy glide directions, then the strain hardening happens in the pile-up materials.

The comparison of results in Fig. 34a and Fig. 34b demonstrates that changing the tool concentration resulted in almost the same specific energy. According to the discussion above, the specific energy is highly dependent on the chip thickness and topography of the micro-grinding tool. Moreover, the variation of the specific energy is not considerable when changing the grinding parameters. Therefore, to find an explanation for the same specific energies observed, the maximum chip thickness has to be analyzed. The chip thickness changes with varying the grinding parameters (i.e. the feed rate, v_w, cutting speed, v_c, depth of cut, a_e, equivalent diameter of the grinding tool, d_s) and tool topography (i.e. cutting-point density, C, and the chip-shape factor, r). Since the geometry and kinematics of the process are the same

(i.e. same aggressiveness number), the chip thickness is changing with the micro-topography of the grinding tool.

The higher the concentration, the higher the number of dynamic grains participating in the chip formation, resulting in higher *C* and lower chip thickness. Since the tool was dressed with the same dressing parameters, we assume a similar shape of the grains, hence the *r* factor should be approximately identical for both micro-grinding tools. Decreasing the chip thickness causes a larger share of elastic and plastic deformation in the grinding process. Hence, increasing the tool concentration at the same aggressiveness number should theoretically increase the values of specific energy. Both micro-grinding tools were analyzed using a confocal microscope after micro-grinding within *Aggr*. of nearly 60. For the 200-concentration tool, a number of the abrasive grains were pulled-out after just one grinding pass. The pulled-out grains caused a reduction in the static and, consequently, dynamic grain density. Hence, the values of specific energy are of the same order.

The efficiency of the micro-grinding process can be improved by proper selection of process parameters. Using higher chip thicknesses resulted in a lower specific energy where higher micro-grinding forces were generated. Lower specific energies lead to a lower share of plastic and elastic deformation and friction in the process and a higher share of cutting. A minimum specific energy of ~11.5 J/mm^3 was achieved for the titanium alloy single-scratch test, regardless of its manufacturing method, in the single grain test. This value is 79 J/mm^3 in the micro-grinding process, which is much higher than the minimum specific energy in the single grain scratch test and macro-grinding process reported by other researchers (between 12-15 J/mm^3 [38,39]).

Shaw and Malkin [12,97] pointed out that the minimum specific energy for the chip formation is associated with the melting specific energy of the material. The minimum specific cutting energy (11.5 J/mm^3) corresponds to the condition in which the friction and plastic deformation are minimal. The specific enthalpy of Ti6Al4V at different temperatures was already investigated by Boivineau et al. [118]. The specific melting energy of the workpiece material at a certain temperature can be determined by the difference of its specific enthalpy at room temperature. For the liquid-state, the specific melting energy of Ti6Al4V can be defined as:

$$U_{liquidus} = H_{liquid} - H_{room} = 5.74 \text{ J/mm}^3 \quad \text{Eq. 7-8}$$

The melting specific energy resembles the liquid state of Ti6Al4V, for which the melting process is completed because the density of liquid titanium is much lower than in the solid-state. For the solid-state, the specific melting energy of the work material can be defined as:

$$U_{soli} = H_{soli} - H_{room} = 4.51 \text{ J/mm}^3 \quad \text{Eq. 7-9}$$

where H_{room} is the enthalpy of Ti6Al4V at room temperature and H_{liquid} and H_{soli} are the enthalpies of Ti6Al4V at liquidus and solidus temperatures, respectively. $U_{liquidus}$ and U_{soli} denote the specific liquidus and solidus energies, respectively. Daneshi [119] modelled the time required for chip formation via each abrasive grain in grinding of nickel alloys. He pointed out that the time required for chip formation is much smaller than the time required for transformation from solidus to liquidus state. He mentioned that the minimum specific grinding energy can be limited to the specific solidus energy of each specific material. However, this minimum energy is approximately 35% higher than the specific solidus energy because of the friction between the abrasive grain and generated chip. The minimum specific cutting energy (11.5 J/mm^3) is much higher than the specific energy required for melting in both solidus and homologous states. Thus, this difference may be a result of high friction between the diamond grain, the chips and the workpiece, as well as higher plowing or plastic deformation in the

cutting process. Moreover, the tool has a defined geometry, i.e. a conical form, with a relatively high negative angle (120 degree) and an ideal sphere tip radius of 100 µm without a sharp cutting. This would cause higher friction. However, in the actual grinding process, the individual grinding tools are much sharper.

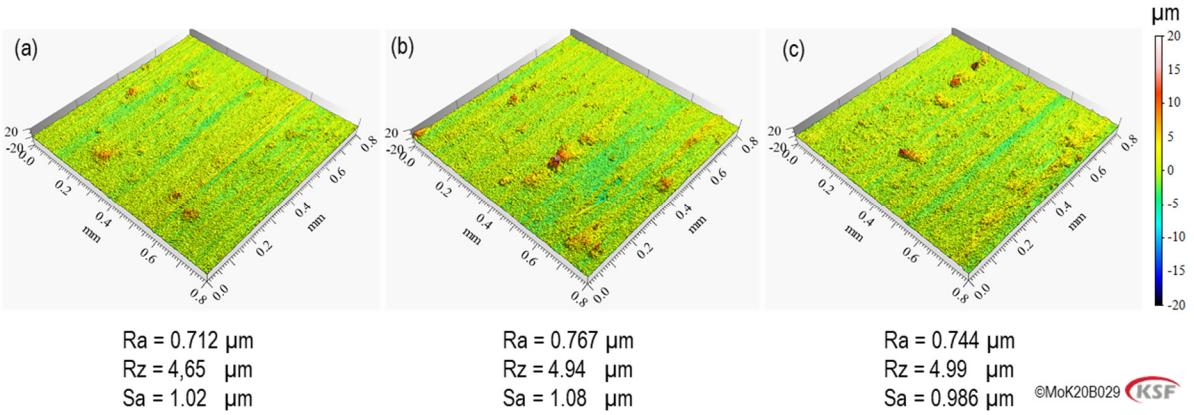

Fig. 35. Surface topography of the workpiece after micro-grinding process for a: conventional part; b: AM BD 20: and c: AM BD 30 (v_c = 10 m/s, a_e= 10 µm, v_w = 800 mm/min, and *Aggr.* ≈ 100).

The topography of the ground surface for the three materials was analyzed and the results are displayed in Fig. 35. Almost the same surface topography was achieved using the same grinding parameters, regardless of the material-manufacturing method. The surface parameter, Sa, and roughness parameters, Ra and Rz, are all nearly of the same order. In all cases, some material debris can also be seen on the ground surface.

7.2.5. Surface roughness

Fig. 36a shows the simulated and experimental values of the surface roughness versus different depth of cuts, based on the method explained in section 6.2. In both simulation and experiment, increasing the depth of cut resulted in a rougher surface finish. As can be seen in Fig. 36a, both predicted and experimental surface roughness values increased with increasing the depth of cut. Increasing the depth of cut increases the grinding forces, which consequently increases the stress on the micro-grinding tool – increasing the risk of vibration and increased surface roughness. The influence of the feed rate on surface roughness at the cutting speed of 14m/s is shown in Fig. 36b. The grinding feed rate has a negligible effect on surface roughness. Although the predicted surface roughness values are somewhat lower than those obtained from experiments. The differences between the simulated and measured surface roughness, seen in Fig. 36b, can be attributed to the unavoidable vibration in the grinding process (at cutting speed of 14m/s). The tool vibration is one of the influential factors which may significantly influence the surface quality. The very small diameter of the tool along with its high rotational speed causes the tool vibration which has been neglected in the simulation.

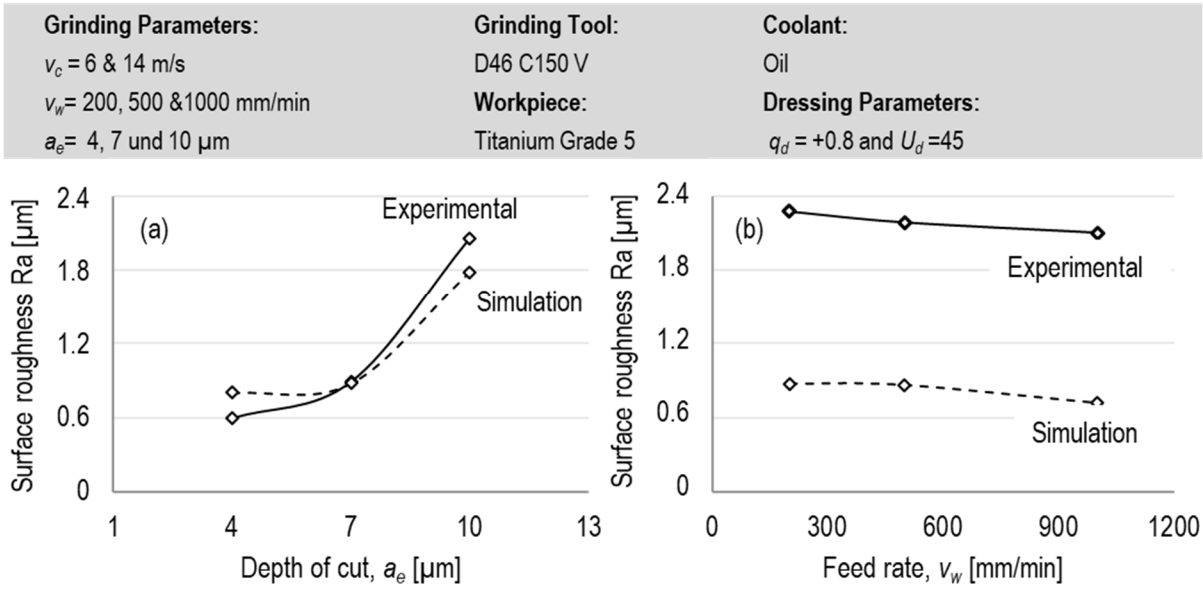

Fig. 36. The simulated and experimental values of the surface roughness versus different a: depth of cuts (v_c = 6 m/s and v_w = 1000); and b: feed rate (v_c = 14 m/s and a_e = 7 µm).

The simulation results agree with the experimental results to a greater degree at a low cutting speed of 6 m/s (Fig. 36a); and less so at higher cutting speed (14 m/s) (Fig. 36b). For an instant, the predicted surface roughness at the cutting speed of 6 m/s, feed rate 100 mm/min, and depth of cut of 7 µm was similar to the real surface roughness (Fig. 36a). However, changing the cutting speed from 6 to 14 m/s increased the measured surface roughness from Ra=0.89 to Ra=2.2. The simulation model predicted a finer surface roughness with increasing the cutting speed from 6 to 14 m/s (Ra=0.89 to Ra=0.65).

8. Conclusions

The main objective of the thesis is to achieve a highly efficient and accurate micro-grinding process in terms of specific grinding energy and surface integrity. In connection with the postulated research questions (RQ), the following conclusions (summarized in Fig. 37) can be drawn:

Surface integrity and effects of different process parameters. (RQ1 and RQ4)

To evaluate the surface integrity in micro grinding, the induced residual stresses, surface roughness, confocal microscopy pictures as well as SEM pictures were analyzed.

Titanium

- Micro-grinding experiments induced only compressive residual stresses – limited to the ground surface. Lower cutting speed and higher v_w/a_e ratio resulted in larger compressive residual stresses. The induced compressive residual stresses by varying the v_w/a_e ratio were mostly caused by thermal loads. Changing the cutting speed generated both thermal and mechanical loads. High cutting speeds led to a severe amount of smeared material, cavities, and material debris. To achieve a finished surface with a good surface integrity, it is necessary to lower cutting speed and increase feed rate; instead of employing a large depth of cut. The tool-workpiece contact length plays an important role in induced residual stresses. For the same specific energy, changing the contact length results in different residual stresses. An almost damage-free surface was achieved when employing the cutting speed of 6 m/s.
- The quality of the finished parts was not affected by the material-manufacturing method (AM vs. wrought). Therefore, the micro-grinding surface integrity was comparable in both material cases.
- The results showed that the surface quality of the finished parts is highly affected by the dressing parameters. Optimization can be done by proper selection of U_d and q_d parameters. Increasing the dressing overlap ratios reduced the values of surface roughness and improved the overall quality of the surface finish.

Si_3N_4

- The results indicate that using ultra-short pulse Laser Assisted Micro-Grinding (LAMG) could improve the accuracy of the part to a large extent. When applying LAMG, no tool deflection was measured during the process. This is in stark contrast to approximately 30% of tool deflection in the Conventional Micro-Grinding (CMG) process.
- Among tested micro-grinding tools with different bonds, the best surface roughness was achieved when using an electroplated grinding tool because of the higher number of active grains and reduced uncut chip thickness.

Process efficiency and underlying the effect different process parameters. (RQ2 and RQ4)

The specific grinding energy is a key indicator to evaluate the efficiency of the micro-grinding process. This indicator can indicate the amount of plastic and elastic deformation as well as ploughing in the process.

Titanium

- Feed-rate-to-depth-of-cut ratio did not significantly affect the specific energy of micro-grinding of titanium, while keeping the maximum chip thickness constant. However, using lower cutting speeds resulted in higher specific grinding energy. Grinding with a sharp tool (achieved by rougher dressing parameters) gave lower specific energy. Concentration of the abrasives did not affect the obtained specific energies.
- The same minimum specific grinding energy of 11. 5 J/mm^3 was obtained in the single-grain scratch tests for both workpiece materials (conventional and AM-produced). Cutting of AM material was more efficient compared to conventional material at chip thicknesses lower than 5 µm due to higher chipping ratios and lower specific energies. In the micro-grinding process, at high aggressiveness, almost the same specific energy was obtained for all materials, independent of their manufacturing process (75 J/mm^3). This energy was much higher than the minimum specific energy required for titanium cutting. This proves a high level of elastic deformation and ploughing in the micro-grinding of titanium. At lower aggressiveness, the AM parts either generated the same or higher specific grinding energies than the conventional part. The built-up direction of the additively manufactured parts had a significant influence on the specific energy (AM BD 30 higher than AM BD 20).

Si_3N_4

- Using a Laser-Assisted Micro-Grinding (LAMG) process could drastically increase the efficiency of the process. However, finding a suitable laser input energy density proved challenging. Comparing the result of specific energy with structured and unstructured tools showed that with approximately 10% tool structuring, the specific energy required for micro-grinding Si_3N_4 could be reduced by up to 60%. This could be achieved by reducing the number of active cutting edges (higher chip thickness) through structuring.
- The hybrid bonded grinding tool showed stable behavior during the long-term grinding test. However, the grinding forces induced by this tool were relatively high. The vitrified grinding tool contained a high porosity and generated lower grinding forces (almost 40 percent lower compared to the metal-bonded tool).

Process modeling and fundamental investigation of titanium micro-grinding (RQ3)

- The developed model enabled that the effects of process parameters and micro-grinding tool topography could be acceptably correlated to the process outputs; of course, with a certain degree of accuracy and simplification. Modelling of the micro-grinding process was applicable by describing the micro-grinding tool topography as a function of the grain size, concentration, height, and distribution.
- From the modelling and experimental results, it can be concluded that the flow stress of the titanium did not change with increasing the strain rate in the range of tested cutting speeds (6-14 m/s). Thus, for a constant chip thickness, the specific grinding forces are almost similar for the utilized cutting speeds. Moreover, the feed rate and depth of cut have the same impact on the specific grinding forces where the grinding forces did not change with changing the feed-rate-to-depth-of-cut ratio.
- One of the most influential factors in modelling the micro-grinding forces is tool deflection. The tool deflection resulting from the normal grinding forces was statically modelled with acceptable accuracy. Another important factor is the dressing process and tool condition. The effect of dressing parameters on force modelling showed that

even at the same chip thickness, finer dressing parameters resulted in higher grinding forces and the prediction model could precisely correlate the dressing parameters to the grinding forces.

- The prediction model could rather precisely estimate tangential and normal micro-grinding forces (mean error of 10%). In the case of prediction of the ground surface roughness, however, the simulation results matched with the experimental results in greater degree at low cutting speed of 6 m/s, rather than at the higher cutting speed (14m/s). This could be because of the tool vibration which occurs at the higher cutting speeds – effect not considered in the model.

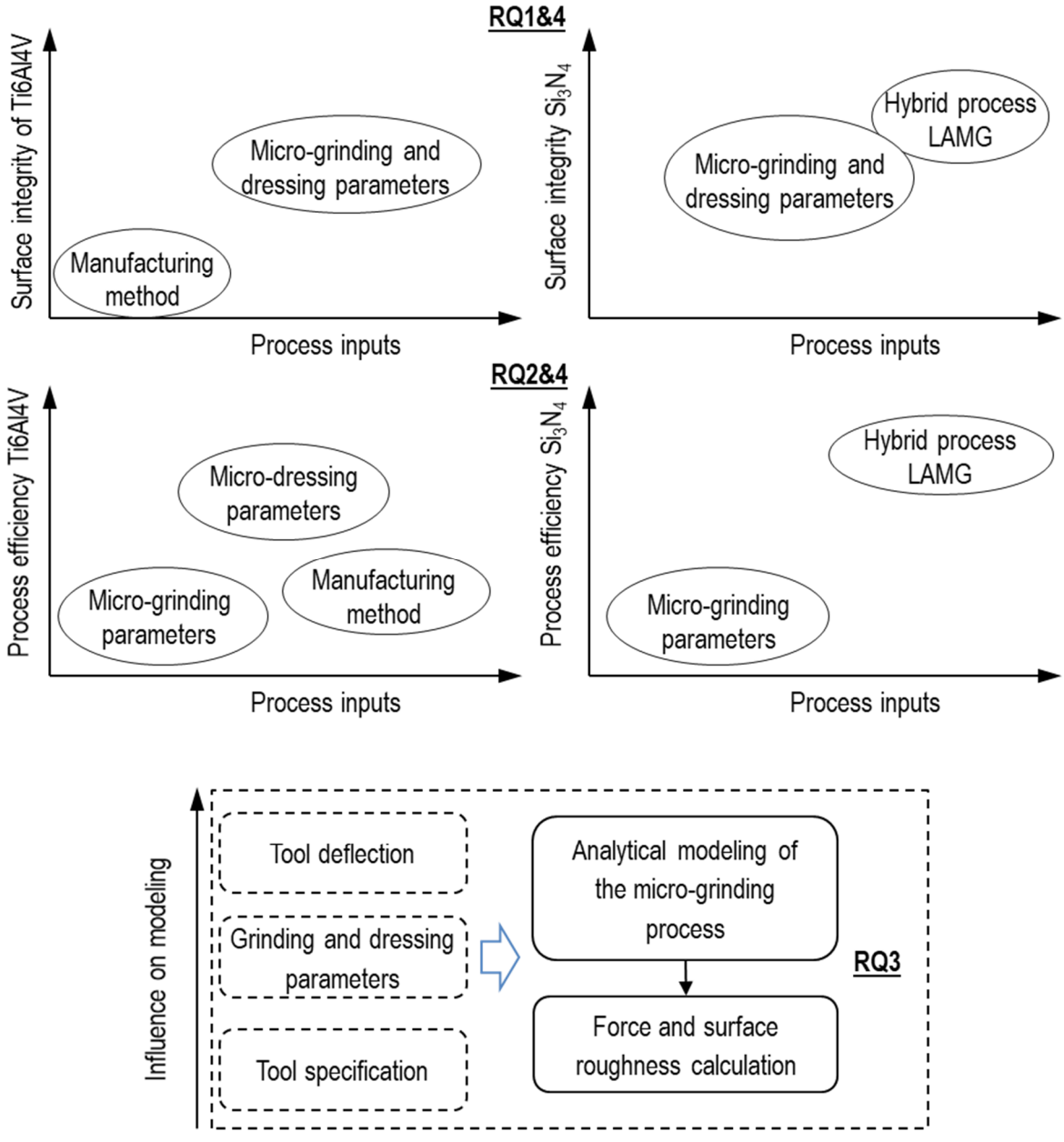

Fig. 37. Flowchart of the main outcomes concerning the defined research questions (RQs).

9. Future work

Based on the results presented in this thesis, the following suggestions are made regarding an extension of the work with respect to micro-chipping mechanism, process efficiency and surface integrity of the machined parts.

- One of the most critical factors, which can largely affect the integrity of the finished surface, is temperature. Thus, a fundamental study of the micro-grinding temperatures is essential. In the micro-grinding process, the workpiece-tool contact length changes rapidly with small variations in the process parameters. Therefore, a thermo-mechanical analysis of the micro-grinding process can give a wealth of knowledge to researchers.
- Because of the size effect, the tool run-out and vibration play an important role in achievable process outputs and the underlying material removal mechanism. In this study, these parameters were neglected. Tool vibration can negatively affect the surface quality and cause tool breakage and grain pull-out.
- Based on the literature review the attritious wear is one of the major wear mechanisms in the micro-grinding process. Hence, a deeper knowledge regarding the wear mechanism and its influence on the surface roughness and process efficiency is necessary.
- The effect of different cutting fluids in the micro-grinding process with small micro-grinding tools is still vague. Moreover, because of the small size of the tool, using high pressure lubrication is not possible. But utilizing high pressure coolants in some cases is necessary, which can cause tool vibration and deflection. This can largely affect the accuracy of the finished parts. Therefore, finding the connection between these parameters are essential. Additionally, because of high rotational speed and small size of the micro-grinding tool, cutting fluids with high viscosity may not reach the tool-workpiece contact zone, therefore the optimization of the cutting fluid density is essential.
- Modelling of the micro-grinding process is still in its early stage. Most of the modelling studies only considered the effect of process parameters and tool specification on the micro-grinding forces and surface roughness. Many important parameters such as tool vibration, run out, and tool deflection are neglected. These parameters have an influence on the process parameters as it was illustrated in this thesis for the case of tool deflection. A deeper modelling study regarding the influence of these parameters is crucial for a better process understanding. Moreover, the thermal aspects must be carefully investigated and the effect of different lubrication, considering various heat sources and size effects, is still open for integration into modelling. Additionally, the influence of the tool wear on the resultant forces may also be considered for modelling.

10. Acknowledgments

First and foremost, I would like to gratefully thank my boss, Professor Bahman Azarhoushang for his help, guidance, encouragement, and financial support during my time at the Institute of Precision Machining (KSF). I similarly thank my main supervisor and examiner, Professor Peter Krajnik, at Chalmers University of Technology for his support, guidance, encouragement, and kindness during my Ph.D. period. I also thank my co-supervisor Professor Uta Klement for her support and guidance. Your door was always open for me, even during your busy and tight schedule. You were always welcoming with my problems and provided me with all the necessary support and valuable input. Without your help, doing this work would not have been possible. Thanks to you all – I learned a lot from you about the history of machining and manufacturing methods, about material characterization, planning, and teaching. I would like to express my deepest appreciation to Dr. Fukuo Hashimoto for his positive role as a discussion leader and his constructive comments during my Licentiate.

Furthermore, I would like to acknowledge several people and companies that I had the pleasure to work with and receive guidance from:

- At the first position, I would like to thank my friend and my group leader Dr. Amir Daneshi. Thank you for the enjoyable collaboration, very useful discussions, helping with the modelling, and teaching me a lot about grinding and cutting processes.
- Sergey Shamray, I express my gratitude for your help and your collaboration. It was a great time to work with you and use your help.
- Faramarz Hojati, thank you for your support in modelling and interesting collaboration in micro-cutting.
- I would like to thank my friend Mr. Nik Hirsch for proofreading of this thesis.
- Alexander Filbert and Felix Blendinger from Furtwangen University, I appreciate your help in the metallography of the materials.
- In particular, I would like to gratefully acknowledge the support of the companies Günther Effgen GmbH, Meister Abrasives AG (specially Mr. Elias Navaro), and Haefeli AG for providing the micro-grinding tools.
- Company Arcam AB/GE Additive, thank you for providing me with the additive manufactured titanium specimens.
- Thank you StressTech GmbH for measuring the residual stress of the ground parts.
- I would like to thank all current and former KSF members, Jahangir Khosravi, Dr. Ali Zahedi, Esmaeil Ghadiri, Dr. Heike Kitzig-Frank, Maria Kohmann, Björn Becker, Robert Bösinger, Dr. Qingfeng Ai, Jürgen Struß, and Babak Soltani. In all problems, you stayed by my side and supported me freely. We spent a lot of time together, we worked together; we enjoyed the time, and we learned a lot together. Thank you all.

Last but not least I want to express my love to my beloved mother and thank her for enduring the distance during my stay and work in Germany from Iran. I thank my sister and my brothers for their support during my stay abroad and my friends in Germany for all their support and encouragement in this period.

References

[1] Masuzawa T. State of the Art of Micromachining. CIRP Annals 2000;49(2):473–88.

[2] Pratap A, Patra K, Dyakonov AA. A comprehensive review of micro-grinding: Emphasis on toolings, performance analysis, modeling techniques, and future research directions. Int J Adv Manuf Technol 2019;104(1-4):63–102.

[3] Jackson MJ. Micro and Nanomanufacturing. Boston, MA: Springer Science+Business Media, LLC; 2007.

[4] Kadivar M, Shamray S, Soltani B, Daneshi A, Azarhoushang B. Laser-assisted micro-grinding of Si3N4. Precision Engineering 2019;60:394–404.

[5] Kadivar M, Azarhoushang B, Shamray S, Krajnik P. The effect of dressing parameters on micro-grinding of titanium alloy. Precision Engineering 2018;51:176–85.

[6] Kadivar M, Azarhoushang B, Daneshi A, Krajnik P. Surface integrity in micro-grinding of Ti6Al4V considering the specific micro-grinding energy. Procedia CIRP 2020;87:181–5.

[7] Weck M, Wenzel C. Ultraprecision machining of microcomponents. Machine Tools 2000;1:113–22.

[8] Azarhoushang B. Anwendungsorientierte Prozessauslegung zum Rundschleifen ohne Formfehler und thermische Schädigung 2014.

[9] Azarhoushang B. Intermittent grinding of ceramic matrix composites: unterbrochenes Schleifen von keramischen Faserverbundwerkstoffen. Shaker; 2011.

[10] Brinksmeier E, Mutlugünes Y, Klocke F, Aurich JC, Shore P, Ohmori H. Ultra-precision grinding. CIRP Annals 2010;59(2):652–71.

[11] Chae J, Park SS, Freiheit T. Investigation of micro-cutting operations. International Journal of Machine Tools and Manufacture 2006;46(3-4):313–32.

[12] Malkin S. Grinding technology: Theory and applications of machining with abrasives. Dearborn, Mich.: Society of Manufacturing Engineers; op. 1989.

[13] Taniguchi N. Current Status in, and Future Trends of, Ultraprecision Machining and Ultrafine Materials Processing. CIRP Annals 1983;32(2):573–82.

[14] Cheng K, Huo D. Micro-cutting: Fundamentals and applications. Chichester, West Sussex, United Kingdom: Wiley; 2013.

[15] Kadivar M. Micro-grinding of titanium: Chalmers Tekniska Hogskola (Sweden); 2018.

[16] Miyashita M. 1st annual precision engineering conference. North Carolina State University, Raleigh, NC, USA 1985;7.

[17] Kadivar M, Azarhoushang B, Daneshi A. Study of specific energy in grinding of tungsten carbide. In: 14th International Conference on High Speed Machining, 17-18th April 2018. Kursaal, San Sebastian - Spain.

[18] Cheng J, Gong YD. Experimental study of surface generation and force modeling in micro-grinding of single crystal silicon considering crystallographic effects. International Journal of Machine Tools and Manufacture 2014;77:1–15.

[19] Cheng J, Wu J, Gong YD, Wen XL, Wen Q. Grinding forces in micro slot-grinding (MSG) of single crystal sapphire. International Journal of Machine Tools and Manufacture 2017;112:7–20.

[20] Ya-Dong G, Yin L, Yao S, Xue-Long W, Qiang L, Shuo-Shuo Q et al. Experimental and emulational investigations into grinding characteristics of Zr-based bulk metallic glass (BMG) using microgrinding. Int J Adv Manuf Technol 2018;97(9-12):3431–51.
[21] Park HW. Development of micro-grinding mechanics and machine tools: Georgia Institute of Technology; 2008.
[22] Setti D, Kirsch B, Aurich JC. An Analytical Method for Prediction of Material Deformation Behavior in Grinding Using Single Grit Analogy. Procedia CIRP 2017;58:263–8.
[23] Perveen A, San WY, Rahman M. Fabrication of different geometry cutting tools and their effect on the vertical micro-grinding of BK7 glass. Int J Adv Manuf Technol 2012;61(1-4):101–15.
[24] Butler-Smith PW, Axinte DA, Daine M. Solid diamond micro-grinding tools: From innovative design and fabrication to preliminary performance evaluation in Ti–6Al–4V. International Journal of Machine Tools and Manufacture 2012;59:55–64.
[25] Aurich JC, Engmann J, Schueler GM, Haberland R. Micro grinding tool for manufacture of complex structures in brittle materials. CIRP Annals 2009;58(1):311–4.
[26] Gong YD, Wen XL, Cheng J, Yin GQ, Wang C. Experimental study on fabrication and evaluation of a micro-scale shaft grinding tool. J Mech Sci Technol 2014;28(3):1027–37. https://doi.org/10.1007/s12206-013-1176-6.
[27] Morgan C, Vallance RR, Marsh ER. Micro Grinding Blind Holes in Hard Tungsten Carbide with Polycrystalline Diamond Micro Tools. In: 20th Annual Meeting of the American Society for Precision Engineering, ASPE 2005; 2005.
[28] Shamray S, Kadivar M, Daneshi A, Azarhoushang B. Performance of micro-grinding pins with different bonding while micro-grinding Si3N4. International Journal of Abrasive Technology 2020;10(1):16–31.
[29] Aurich JC, Carrella M, Walk M. Micro grinding with ultra small micro pencil grinding tools using an integrated machine tool. CIRP Annals 2015;64(1):325–8.
[30] Dyakonov A, Gorodkova A. Experimental research of cutting forces during microgrinding. In: MATEC Web of Conferences; 2018, p. 1049.
[31] Perveen A, Jahan MP, Rahman M, Wong YS. A study on microgrinding of brittle and difficult-to-cut glasses using on-machine fabricated poly crystalline diamond (PCD) tool. Journal of Materials Processing Technology 2012;212(3):580–93.
[32] Lee P-H, Nam JS, Li C, Lee SW. An experimental study on micro-grinding process with nanofluid minimum quantity lubrication (MQL). Int. J. Precis. Eng. Manuf. 2012;13(3):331–8.
[33] Lee P-H, Lee SW. Experimental characterization of micro-grinding process using compressed chilly air. International Journal of Machine Tools and Manufacture 2011;51(3):201–9.
[34] Yin G, Wang D, Cheng J. Experimental investigation on micro-grinding of SiCp/Al metal matrix composites. Int J Adv Manuf Technol 2019;102(9-12):3503–17.
[35] Hashimoto F, Yamaguchi H, Krajnik P, Wegener K, Chaudhari R, Hoffmeister H-W et al. Abrasive fine-finishing technology. CIRP Annals 2016;65(2):597–620.

[36] Morgan CJ, Vallance RR, Marsh ER. Specific grinding energy while microgrinding tungsten carbide with polycrystalline diamond micro tools. In: ICOMM-2007 2nd International Conference on Micro-Manufacturing; 2007, p. 180–187.
[37] Badger J. Grinding of sub-micron-grade carbide: Contact and wear mechanisms, loading, conditioning, scrubbing and resin-bond degradation. CIRP Annals 2015;64(1):341–4.
[38] Guo GQ, Liu ZQ, Zheng XH, Chen M. Investigation on Surface Grinding of Ti-6Al-4V Using Minimum Quantity Lubrication. AMR 2012;500:308–13.
[39] Kacalak W, Lipiński D, Bałasz B, Rypina Ł, Tandecka K, Szafraniec F. Performance evaluation of the grinding wheel with aggregates of grains in grinding of Ti-6Al-4V titanium alloy. Int J Adv Manuf Technol 2018;94(1-4):301–14. https://doi.org/10.1007/s00170-017-0905-x.
[40] Zhou Y, Ma L, Gong Y, Zhang L, Yin G, Sun Y. Study on the mechanism of chip forming and the microhardness of micro-grinding nickel-based single-crystal superalloy. Int J Adv Manuf Technol 2019;103(1-4):281–95.
[41] Gong Y, Zhou Y, Wen X, Cheng J, Sun Y, Ma L. Experimental study on micro-grinding force and subsurface microstructure of nickel-based single crystal superalloy in micro grinding. J Mech Sci Technol 2017;31(7):3397–410. https://doi.org/10.1007/s12206-017-0629-8.
[42] Zhou Y, Gong Y, Cai M, Zhu Z, Gao Q, Wen X. Study on surface quality and subsurface recrystallization of nickel-based single-crystal superalloy in micro-grinding. Int J Adv Manuf Technol 2017;90(5-8):1749–68.
[43] Fook P, Berger D, Riemer O, Karpuschewski B. Structuring of Bioceramics by Micro-Grinding for Dental Implant Applications. Micromachines 2019;10(5):312.
[44] Zhang Q, To S, Zhao Q, Guo B. Amorphization and C segregation based surface generation of Reaction-Bonded SiC/Si composites under micro-grinding. International Journal of Machine Tools and Manufacture 2015;95:78–81.
[45] Zhang Q, To S, Zhao Q, Guo B. Recrystallization of amorphized Si during micro-grinding of RB-SiC/Si composites. Materials Letters 2016;172:48–51.
[46] Lee P-H, Kim JW, Lee SW. Experimental characterization on eco-friendly micro-grinding process of titanium alloy using air flow assisted electrospray lubrication with nanofluid. Journal of Cleaner Production 2018;201:452–62.
[47] Sun G, Ding Z. Effects of Heating Rate and Strain Rate on Phase Transformation in Micro-Grinding. EPJ Web Conf. 2019;224:5003.
[48] Fook P, Riemer O. Characterization of Zirconia-Based Ceramics After Microgrinding. Journal of Micro and Nano-Manufacturing 2019;7(2).
[49] Malkin S, Cook NH. The Wear of Grinding Wheels: Part 1—Attritious Wear. Journal of Engineering for Industry 1971;93(4):1120–8.
[50] Malkin S, Cook NH. The Wear of Grinding Wheels: Part 2—Fracture Wear. Journal of Engineering for Industry 1971;93(4):1129–33.
[51] Feng J, Kim BS, Shih A, Ni J. Tool wear monitoring for micro-end grinding of ceramic materials. Journal of Materials Processing Technology 2009;209(11):5110–6.
[52] Li W, Ren Y, Li C, Li Z, Li M. Investigation of machining and wear performance of various diamond micro-grinding tools. Int J Adv Manuf Technol 2020;106(3-4):921–35.

[53] Perveen A, Molardi C. Machining of Glass Materials: An Overview. In: Gupta K, editor. Advanced Manufacturing Technologies. Cham: Springer International Publishing; 2017, p. 23–47.
[54] Malkin S, Hwang TW. Grinding Mechanisms for Ceramics. CIRP Annals 1996;45(2):569–80.
[55] Lawn BR, Evans AG. A model for crack initiation in elastic/plastic indentation fields. J Mater Sci 1977;12(11):2195–9.
[56] Bifano TG, Dow TA, Scattergood RO. Ductile-Regime Grinding: A New Technology for Machining Brittle Materials. Journal of Engineering for Industry 1991;113(2):184–9.
[57] Cheng J, Wu J, Gong YD, Wen XL, Wen Q. Experimental study on the single grit interaction behaviour and brittle–ductile transition of grinding with a diamond micro-grinding tool. Int J Adv Manuf Technol 2017;91(1-4):1209–26.
[58] Cheng J, Gong YD. Experimental study on ductile-regime micro-grinding character of soda-lime glass with diamond tool. Int J Adv Manuf Technol 2013;69(1-4):147–60.
[59] Li Z, Zhang F, Luo X, Guo X, Cai Y, Chang W et al. A New Grinding Force Model for Micro Grinding RB-SiC Ceramic with Grinding Wheel Topography as an Input. Micromachines 2018;9(8):368.
[60] Mirifar S, Kadivar M, Azarhoushang B. First Steps through Intelligent Grinding Using Machine Learning via Integrated Acoustic Emission Sensors. JMMP 2020;4(2):35.
[61] Yang M, Li C, Zhang Y, Jia D, Li R, Hou Y et al. Effect of friction coefficient on chip thickness models in ductile-regime grinding of zirconia ceramics. Int J Adv Manuf Technol 2019;102(5-8):2617–32.
[62] Yang M, Li C, Zhang Y, Jia D, Li R, Hou Y et al. Predictive model for minimum chip thickness and size effect in single diamond grain grinding of zirconia ceramics under different lubricating conditions. Ceramics International 2019;45(12):14908–20.
[63] Agarwal S, Venkateswara Rao P. Predictive modeling of undeformed chip thickness in ceramic grinding. International Journal of Machine Tools and Manufacture 2012;56:59–68.
[64] Zhang Y, Fang C, Huang G, Xu X. Modeling and simulation of the distribution of undeformed chip thicknesses in surface grinding. International Journal of Machine Tools and Manufacture 2018;127:14–27.
[65] Cheng J, Wang C, Wen X, Gong Y. Modeling and experimental study on micro-fracture behavior and restraining technology in micro-grinding of glass. International Journal of Machine Tools and Manufacture 2014;85:36–48.
[66] Li HN, Yu TB, Wang ZX, Zhu LD, Wang WS. Detailed modeling of cutting forces in grinding process considering variable stages of grain-workpiece micro interactions. International Journal of Mechanical Sciences 2017;126:319–39.
[67] Gorodkova AE, Dyakonov AA, Herreinstein AV. Thermophysical modeling of microgrinding. Russ. Engin. Res. 2017;37(7):647–50.
[68] Niinomi M. Recent research and development in titanium alloys for biomedical applications and healthcare goods. Science and Technology of Advanced Materials 2016;4(5):445–54.
[69] Rack HJ, Qazi JI. Titanium alloys for biomedical applications. Materials Science and Engineering: C 2006;26(8):1269–77.

[70] Zhang YT, Bottausci F, Rao MP, Parker ER, Mezic I, Macdonald NC. Titanium-based dielectrophoresis devices for microfluidic applications. Biomed Microdevices 2008;10(4):509–17.
[71] Parker ER, Rao MP, Turner KL, Macdonald NC. Bulk titanium microneedles with embedded microfluidic networks for transdermal drug delivery. In: 19th IEEE International Conference on Micro Electro Mechanical Systems; 2006, p. 498–501.
[72] Parker ER, Rao MP, Turner KL, Meinhart CD, Macdonald NC. Bulk Micromachined Titanium Microneedles. J. Microelectromech. Syst. 2007;16(2):289–95.
[73] Voice W. The future use of gamma titanium aluminides by Rolls-Royce. Aircraft Eng & Aerospace Tech 1999;71(4):337–40.
[74] Marenzi G, Spagnuolo G, Sammartino JC, Gasparro R, Rebaudi A, Salerno M. Micro-Scale Surface Patterning of Titanium Dental Implants by Anodization in the Presence of Modifying Salts. Materials (Basel, Switzerland) 2019;12(11).
[75] Parker ER, Thibeault BJ, Aimi MF, Rao MP, Macdonald NC. Inductively Coupled Plasma Etching of Bulk Titanium for MEMS Applications. J. Electrochem. Soc. 2005;152(10):C675.
[76] Jaffery SI, Mativenga PT. Assessment of the machinability of Ti-6Al-4V alloy using the wear map approach. Int J Adv Manuf Technol 2009;40(7-8):687–96.
[77] Thepsonthi T, Özel T. Multi-objective process optimization for micro-end milling of Ti-6Al-4V titanium alloy. Int J Adv Manuf Technol 2012;63(9-12):903–14.
[78] Hojati F, Daneshi A, Soltani B, Azarhoushang B, Biermann D. Study on machinability of additively manufactured and conventional titanium alloys in micro-milling process. Precision Engineering 2020;62:1–9.
[79] Özel T, Thepsonthi T, Ulutan D, Kaftanoğlu B. Experiments and finite element simulations on micro-milling of Ti-6Al-4V alloy with uncoated and cBN coated micro-tools. CIRP Annals 2011;60(1):85–8.
[80] Robinson AE, Funke HH-W, Hendrick P, Recker E, Peirs J. Development of a hydrogen fuelled 1 kW ultra micro gas turbine with special respect to designing, testing and mapping of the μ-scale combustor. In: 2008 IEEE International Conference on Sustainable Energy Technologies (ICSET), p. 656–660.
[81] Piotter V, Bauer W, Knitter R, Mueller M, Mueller T, Plewa K. Powder injection moulding of metallic and ceramic micro parts. Microsyst Technol 2011;17(2):251–63.
[82] Müller T, Piotter V, Plewa K, Guttmann M, Ritzhaupt-Kleissl H-J, Hausselt J. Ceramic micro parts produced by micro injection molding: Latest developments. Microsyst Technol 2010;16(8-9):1419–23.
[83] Azarhoushang B, Soltani B, Zahedi A. Laser-assisted grinding of silicon nitride by picosecond laser. The International Journal of Advanced Manufacturing Technology 2017;93(5-8):2517–29.
[84] Jahanmir S, Ramulu M, Koshy P. Machining of ceramics and composites. Marcel Dekker; 1999.
[85] Pfeiffer W, Hollstein T, Zeller R. Bearbeitungsbedingte Randschichtintegrität und Verschleißverhalten von Keramik. Materialwissenschaft und Werkstofftechnik 2000;31(8):787–9.

[86] Weinert K, Schneider M, Willsch C. Influence of Grinding on the Quality of the Cutting Edge. Prod. Eng. Res. Devel. 1996;3(2):49–52.
[87] Azarhoushang B, Zahedi A. Laser conditioning and structuring of grinding tools-a review. Advances in Manufacturing 2017;5(1):35–49.
[88] Azarhoushang B, Kadivar M, Bösinger R, Shamray S, Zahedi A, Daneshi A. High-speed high-efficient grinding of CMCs with structured grinding wheels. International Journal of Abrasive Technology 2019;9(1):1–15.
[89] Zahedi A, Azarhoushang B, Akbari J. Conditioning of vitrified and resin bond CBN grinding wheels using a picosecond laser. Scientia Iranica. Transaction B, Mechanical Engineering 2017;24(5):2369–78.
[90] Transchel R, Stirnimann J, Blattner M, Bill B, Thiel R, Kuster F et al. Effective Dynamometer for Measuring High Dynamic Process Force Signals in Micro Machining Operations. Procedia CIRP 2012;1:558–62.
[91] Azarhoushang B, Soltani B, Daneshi A. Study of the effects of laser micro structuring on grinding of silicon nitride ceramics. CIRP Annals 2018;67(1):329–32.
[92] Lide DR. CRC handbook of chemistry and physics. CRC press; 2004.
[93] Weikert M. Oberflächenstrukturieren mit ultrakurzen Laserpulsen [Dissertation]; 2005.
[94] Porter DA, Easterling KE. Phase transformations in metals and alloys (revised reprint). CRC press; 2009.
[95] Bäuerle D. Laser processing and chemistry. Springer Science & Business Media; 2013.
[96] Zahedi A, Azarhoushang B. FEM based modeling of cylindrical grinding process incorporating wheel topography measurement. Procedia CIRP 2016;46(1):201–4.
[97] Shaw MC. Principles of abrasive processing. Oxford University Press on Demand; 1996.
[98] Younis MA, Alawi H. Probabilistic analysis of the surface grinding process. Transactions of the Canadian Society for Mechanical Engineering 1984;8(4):208–13.
[99] Hecker RL, Ramoneda IM, Liang SY. Analysis of Wheel Topography and Grit Force for Grinding Process Modeling. Journal of Manufacturing Processes 2003;5(1):13–23.
[100] Rowe WB, Morgan MN, Qi HS, Zheng HW. The Effect of Deformation on the Contact Area in Grinding. CIRP Annals 1993;42(1):409–12.
[101] Klocke F, Knig W. Fertigungsverfahren 2. Springer; 2005.
[102] Tawakoli T, Azarhoushang B. Intermittent grinding of ceramic matrix composites (CMCs) utilizing a developed segmented wheel. International Journal of Machine Tools and Manufacture 2011;51(2):112–9.
[103] Wegener K, Hoffmeister H-W, Karpuschewski B, Kuster F, Hahmann W-C, Rabiey M. Conditioning and monitoring of grinding wheels. CIRP Annals 2011;60(2):757–77.
[104] Klocke F, Linke B. Mechanisms in the generation of grinding wheel topography by dressing. Prod. Eng. Res. Devel. 2008;2(2):157–63.
[105] Malkin S, Murray T. Mechanics of rotary dressing of grinding wheels 1978.
[106] Linke B. Dressing process model for vitrified bonded grinding wheels. CIRP Annals 2008;57(1):345–8.
[107] Daneshi A, Jandaghi N, Tawakoli T. Effect of dressing on internal cylindrical grinding. Procedia CIRP 2014;14:37–41.
[108] Kadivar M, Zahedi A, Azarhoushang B, Krajnik P. Modelling of the micro-grinding process considering the grinding tool topography. IJAT 2017;8(2):157.

[109] Dražumerič R, Badger J, Roininen R, Krajnik P. On geometry and kinematics of abrasive processes: The theory of aggressiveness. International Journal of Machine Tools and Manufacture 2020;154:103567.
[110] Moriwaki T, Sugimura N, Luan S. Combined Stress, Material Flow and Heat Analysis of Orthogonal Micromachining of Copper. CIRP Annals 1993;42(1):75–8.
[111] Eleiche AM, Campbell JD. Strain-rate effects during reverse torsional shear. Experimental Mechanics 1976;16(8):281–90.
[112] Kadivar M, Azrhoushang B, Zahedi A, Müller C. Laser-assisted micro-milling of austenitic stainless steel X5CrNi18-10. Journal of Manufacturing Processes 2019;48:174–84.
[113] Hamdi H, Zahouani H, Bergheau J-M. Residual stresses computation in a grinding process. Journal of Materials Processing Technology 2004;147(3):277–85. https://doi.org/10.1016/S0924-0136(03)00578-8.
[114] Brinksmeier E, Brockhoff T. Randschicht-wärmebehandlung durch schleifen. HTM. Härterei-technische Mitteilungen 1994;49(5):327–30.
[115] Capello E, Semeraro Q. Process parameters and residual stresses in cylindrical grinding. J. Manuf. Sci. Eng. 2002;124(3):615–23.
[116] Nachmani Z. Randzonenbeeinflussung beim Schnellhubschleifen. Apprimus-Verlag; 2008.
[117] Dmitriev AI, Nikonov AY, Shugurov AR, Panin AV. Numerical study of atomic scale deformation mechanisms of Ti grains with different crystallographic orientation subjected to scratch testing. Applied Surface Science 2019;471:318–27.
[118] Boivineau M, Cagran C, Doytier D, Eyraud V, Nadal M-H, Wilthan B et al. Thermophysical Properties of Solid and Liquid Ti-6Al-4V (TA6V) Alloy. Int J Thermophys 2006;27(2):507–29.
[119] Daneshi A. Micro chip formation mechanism in grinding of Nickel-base superalloy-Inconel 718. Albert-Ludwigs-Universität Freiburg; 2019.